Electronic Supplementary Material (ESI) for Energy & Environmental Science.

Supplementary Materials for

3D-ordered catalytic nanoarrays interlocked on anion exchange membranes for water electrolysis

Lei Wan, Jing Liu, Dongcheng Lin, Ziang Xu, Yihan zhen, Maobing Pang, Qin Xu, and Baoguo Wang*
*Corresponding author. Email: bgwang@tsinghua.edu.cn

Experimental Section

1. Chemicals and materials

Ni foil was obtained from Metal Materials Research Institute, Hefei, China. Ni foam was bought from Shenzhen Lifeixin Environmental Protection Co., Ltd. Nickel chloride hexahydrate ($NiCl_2·6H_2O$, 99%), cobalt chloride hexahydrate ($CoCl_2·6H_2O$, 99%), ammonium chloride (NH_4Cl, 99%), urea (99%), polyethylene glycol (M_w = 10000 g mol^{-1}), ferrous sulfate hexahydrate ($FeSO_4·6H_2O$, 99%), nickel nitrate hexahydrate ($Ni(NO_3)_2·6H_2O$, 99%), cupric nitrate hemi(pentahydrate) ($Cu(NO_3)_2·2.5H_2O$, 99%), iron nitrate nonahydrate ($Fe(NO_3)_3·9H_2O$, 99%), ammonium fluoride (NH_4F, 99%), sodium hypophosphite monohydrate ($NaH_2PO_2·H_2O$, 99%), ammonium persulfate (APS, 99%), P-terphenyl (99%), N-methyl-4-piperidone (98%), and CH_2Cl_2 (⩾ 99.9%) were purchased from Aladdin Reagent Co., Ltd. Trifluoromethanesulfonic acid and Trifluoroacetic acid were supplied by Energy Chemical. Pt/C (20 wt%, Johnson Matthey), IrO_2, PiperION™ membrane were purchased from fuel cell store. Nafion 117 membrane was purchased from DuPont. FAA-3-50 and PBI membranes were purchased from Fumatech. Sustainion X37-50 membranes (50 μm) were purchased from Dioxide Materials. All chemicals were used without further purification. Deionized (DI) water (18.2 MΩ) was obtained using a Millipore system and used to prepare all aqueous solutions.

2. Materials preparation

2.1. Preparation of CoNi LDH nanowire arrays

The CoNi LDH nanowire arrays were prepared via a simple hydrothermal method. Before synthesis, the Ni foil (NF) surface was initially cleaned by acid wash (1 M HCl) in an ultrasound bath for 10 min. Then the Ni foil was washed with deionized water for several times before use. The treated Ni foil was transferred into a stainless-steel autoclave (100 mL) containing a homogenous solution of

$NiCl_2 \cdot 6H_2O$ (0.005 M), $CoCl_2 \cdot 6H_2O$ (0.01 M) and urea (0.015 M) in 75 mL H_2O. Afterward, the autoclave was sealed and maintained at 120 ℃ for 5 h. The obtained CoNi LDH/NF was then taken out and washed with DI water.

2.2. Preparation of FeNi LDH nanosheet arrays

The FeNi LDH nanosheet arrays were prepared via a simple electroposition method. Before synthesis, the Ni foil surface was initially cleaned by acid wash (1 M HCl) in an ultrasound bath for 10 min. Briefly, $FeSO_4 \cdot 6H_2O$ (0.15 M) and $Ni(NO_3)_2 \cdot 6H_2O$ (0.15 M) were dissolved in DI (200 mL). The carbon rod and Ni foil were utilized as the anode and cathode, respectively. FeNi LDH was electrodeposition onto Ni foil at a constant current density (5 mA cm^{-2}) for 2 min. After electrodeposition, the obtained FeNi LDH/NF was washed three times with water and dried in air for 12 h.

2.3. Preparation of hierarchical $NiCo_2O_4$@FeNi LDH nanowire arrays

To prepare the hierarchical $NiCo_2O_4$@FeNi LDH nanowire arrays, the as-prepared NiCo LDH/NF was calcined at 400 ℃ for 3 h. Further, the FeNi LDH were electrodeposited on $NiCo_2O_4$/NF in a two-electrode configuration. Briefly, $FeSO_4 \cdot 6H_2O$ (0.15 M) and $Ni(NO_3)_2 \cdot 6H_2O$ (0.15 M) were dissolved in DI (200 mL). The carbon rod and $NiCo_2O_4$/NF were utilized as the anode and cathode, respectively. FeNi LDH was electrodeposited onto $NiCo_2O_4$ at a constant current density (5 mA cm^{-2}) for 2 min. After electrodeposition, the obtained $NiCo_2O_4$@FeNi LDH/NF was washed three times with water and dried in air for 12 h.

2.4. Preparation of Ni porous foams

The Ni porous foams were prepared via one-step electrodeposition. Before synthesis, the Ni foil was trated by the same method. The porous Ni foams were prepared by electrodeposition at a high current density (2000 mA cm^{-2}) for 90 s in a two-electrode electrode system. The carbon rod and NF were utilized as the anode and cathode, respectively. The electrodeposition solution was composed of $NiCl_2 \cdot 6H_2O$ (0.1 M) and NH_4Cl (1 M). The as-prepared Ni/NF was washed with ethanol and DI water prior to drying in a vacuum oven at 50 ℃ for 1 h.

2.5. Preparation of hierarchical NiCo@FeNi LDH porous foams

The hierarchical NiCo@FeNi LDH porous foams were prepared via two-step electrodeposition. Before synthesis, the Ni foil was trated by the same method. The porous NiCo alloy foams were prepared by electrodeposition at a high current density (2000 mA cm^{-2}) for 90 s in a two-electrode electrode system. The carbon rod and NF were utilized as the anode and cathode, respectively. The electrodeposition solution was composed of $CoCl_2 \cdot 6H_2O$ (0.1 M), $NiCl_2 \cdot 6H_2O$ (0.1 M) and NH_4Cl (1 M). The as-prepared NiCo/NF was washed with ethanol and DI water prior to drying in a vacuum oven at 50 ℃ for 1 h. The hierarchical NiCo@FeNi LDH porous foams were then prepared by the previously described electrodeposition process.

2.6. Preparation of alkaline QAPPT ionomer

The quaternary ammonia poly (N-methyl-piperidine-co-p-terphenyl) (QAPPT) polymers were synthesized following recently reported literature[1]. 7.44 g (32 mmol) P-terphenyl was dissolved in 12 mL CH_2Cl_2 under ice bath and 4.2 mL (36 mmol) N-Methyl-4-piperidone was added, then 2.4 mL trifluoroacetic acid was poured in the solution. Finally 30 mL trifluoromethanesulfonic acid was slowly added to the system with constantly mechanical agitation. After 3 h, the products were precipitation in an aqueous solution of K_2CO_3, washed with distilled water and dried in vacuum oven

at 60 ℃ for 24 h. The PPT ploymer was obtained. 6.5 g PPT was dissolved in 150 mL mixed solvent (125 mL NMP + 25 mL DMSO) and 20 mL CH_3I was added. The reaction was proceeded at 70 ℃ for ~8 h then the solution was poured into ether to get dark brown solid. Next the soild was soaked in an aqueous solution of 1 M KOH at 60 ℃ for 24 h, filtered and washed with distilled water until the filtrate was neutral. The QAPPT polymer was finally got and dried in vacuum oven at 60 ℃ for 24h.

2.7. Preparation of novel 3D-ordered MEAs

To achieve 3D-ordered anode CLs on an AEM, a layer of polymer electrolyte dispersion is directly deposited on top of the as-prepared electrodes *via* ultrasonic spray technique. Subsequently, the cathode catalyst slurry was sprayed on the as-prepared AEM surface. To prepare the cathode catalyst slurry, Pt/C (20 wt.% Pt) catalysts were homogeneously mixed with an alkaline QAPPT ionomer in an isopropanol/water (8/2 in volume) mixed solvent by ultrasound for 2 h. The Pt loadings for cathode CL were controlled to be 1 mg cm^{-2}. To remove the dense Ni foil, the as-prepared samples were immersed into deionized water for 1 min. Then, the samples were taken out and heated at 50 ℃ for 8 min. Owing the high interfacial bonding strength between the membrane and anode CL, the Ni foil was effectively removed through swelling-assisted transfer method. Finally, the 3D-ordered MEAs were stored in 1 M KOH to replace Br^- with OH^-. In different MEA tests, the deviation range of membrane thickness is 30-35 μm. The membrane thickness of MEAs is determined by the volume of polymer electrolyte dispersion for direct membrane deposition.

2.8. Preparation of conventional ordered MEAs

Before the MEA preparation, the conventionally used QAPPT membrane was prepared by casting polymer electrolyte dispersion on a glass Petri dish. After drying at 60 ℃ for one day, the resulting membrane was gently peeled from the dish. Then, the conventional 3D-ordered MEAs were prepared

from decal transfer method. The hierarchical nanoarrays or porous foams were decaled onto as-prepared QAPPT membranes under the pressure of 4.0 MPa at 140 ℃ for 1 min to form CCM electrodes. After decal, the stainless steel plates were physically removed deliberately. The obtained conventional 3D-ordered MEAs were stored in 1 M KOH to replace Br^- with OH^-.

2.9. Preparation of conventional MEA-CCS

The hierarchical NiCo@FeNi LDH porous foams were prepared on Ni foam using the same synthesis process as described above. For the cathode, the Pt/C ink with the same composition was sprayed on the carbon paper. To form a MEA-CCS, the NiCo@FeNi LDH/Ni foam and Pt/C/carbon paper were assembled with the self-supported QAPPT membrane by hot pressing under the pressure of 1.0 MPa at 120 ℃ for 1 min.

2.10. Preparation of conventional MEA-CCM

To prepare the anode catalyst slurry, IrO_2 or NiCo@FeNi LDH catalysts were homogeneously mixed with an alkaline QAPPT ionomer in an isopropanol/water (8/2 in volume) mixed solvent by ultrasound for 2 h. The powdery NiCo@FeNi LDH catalysts were obtained by scraping the powder from self-supported NiCo@FeNi LDH/Ni foil. The as-prepared anode catalyst slurry was sprayed on one side of the self-supported QAPPT membrane. The IrO_2 loadings for anode CL were controlled to be 2 mg cm^{-2}. For the cathode CL, the Pt/C ink with the same composition was sprayed on the other side of the self-supported QAPPT membrane. To form five-layered MEA-CCM, the as-prepared three-typed MEA-CCM was assembled with the Ni foam and carbon paper by hot pressing under the pressure of 1.0 MPa at 120 ℃ for 1 min.

2.11. Preparation of novel 3D-ordered MEAs with different catalytic nanoarrays

To prepare 3D-ordered MEA with chemically etched CuCo-oxide (CE-CCO) as the ACL, the CE-CCO was first prepared on the Ni foil according to the previous report[2]. Specifically, the CE-CCO electrode was preapred by electrodeposition in a solution (100 mL) containing $Co(NO_3)_2 \cdot 6H_2O$ (50 mM) and $Cu(NO_3)_2 \cdot 2.5H_2O$ (15 mM), with Ni foil used as the working electrode substrate. Prior to electrodeposition, Ni foil was etched with 1 M HCl for 10 min to remove surface oxide layers. A Pt mesh (3 cm × 4 cm) and a saturated calomel electrode (SCE) separated by a distance of 1 cm were used as counter and reference electrodes, respectively. $(Cu,Co)(OH)_2$ was electrodeposited on Ni foil at a constant potential of −1 V_{SCE} for 5 min at room temperature without stirring, and the obtained electrode was thoroughly rinsed with DI water, immersed into 0.2 M APS for 10 s, and then rinsed several times with DI water. The sample was then air-dried and heated to 250 °C for 3 h at 1 °C min^{-1}. The loading amount of CE-CCO in Ni foil was about 3.6 mg cm^{-2}. The CE-CCO was then transferred from the Ni foil to the AEM using the swelling-assisted transfer method.

To prepare 3D-ordered MEA with ternary FeCoNi LDH as the ACL, the FeCoNi LDH was first prepared on the Ni foil according to the modified previous report[3]. Specifically, the surface oxide layer of Ni foil was removed through sonication in 1 M HCl for 10 min. $Fe(NO_3)_3 \cdot 9H_2O$ (25 mM), $Ni(NO_3)_2 \cdot 6H_2O$ (25 mM), $Co(NO_3)_2 \cdot 6H_2O$ (25 mM), polyethylene glycol (1 g), and urea (0.1 M) were dissolved in DI water (40 mL) and stirred for 30 min to get a transparent precursor solution. Then, the precursor solution was transferred into a Teflon-lined stainless autoclave (100 mL), and the Ni foil was vertically immersed into the liquid. After that, the autoclave was sealed and transferred into an electric oven. The reaction was continued for 5 h at 120 ℃, and then cooled down naturally, and the obtained FeCoNi LDH/Ni foil sample was rinsed with a massive amount deionized water and ethanol, and dried in the fume hood. The loading amount of FeCoNi LDH in Ni foil was about 3.1

mg cm^{-2}. The FeCoNi LDH was then transferred from the Ni foil to the AEM using the swelling-assisted transfer method. In the 3D-ordered MEAs with CE-CCO and FeCoNi LDH as the ACLs, the CCLs were prepared by spraying the Pt/C ink on the AEM.

To prepare 3D-ordered MEA with CoP as the CCL, the CoP was first prepared on the Ni foil according to the previous report[4]. Specifically, the surface oxide layer of Ni foil was removed through sonication in 1 M HCl for 10 min. $Co(NO_3)_2 \cdot 6H_2O$ (0.291 g), NH_4F (0.093 g) and urea (0.30 g) were dissolved in 20 mL water under vigorous stirring for 30 min. Then the solution was transferred into a Teflon-lined stainless autoclave (25 mL), and the Ni foil was vertically immersed into the liquid. The autoclave was sealed and maintained at 120 ℃ for 6 h in an electric oven. After the autoclave cooled down slowly at room temperature, the Co(OH)F/Ni foil was taken out and washed with water thoroughly before vaccum dried. To prepare CoP/Ni foil, Co(OH)F/Ni foil and NaH_2PO_2 were put at two separate positions in a porcelain boat with NaH_2PO_2 at the upstream side of the furnace. The molar ratio of Co to P is 1:5. Subsequently, the samples were heated at 300 ℃ for 60 min in a static Ar atmosphere, and then naturally cooled to ambient temperature under Ar. The loading amount of CoP in Ni foil was about 1.0 mg cm^{-2}. The CoP was then transferred from the Ni foil to the AEM using the swelling-assisted transfer method. The ACL was prepared by spraying the IrO_2 ink on the AEM.

3. Characterization

3.1. Morphology structure analysis

The microstructure of MEAs was observed by using a scanning electron microscope (SEM, Hitachi SU-8010) and transmission electron microscopy (TEM, JEM2010). For the surface analysis of MEAs through SEM, samples were completely dried in an oven before observing. For the cross-section analysis of MEAs through SEM, samples were firstly freezed in liquid nitrogen and then a

slight force has been put in order to obtain brittle fracture in order to obtain the cross section of MEAs. The energy element dispersity at the cross section was collected by using a dispersive X-ray (EDX) spectrometry accessory (X-max 80).

To observe the ionomer distribution in 3D-ordered ACLs by SEM, the nanostructed electrocatalysts were removed by immersing MEA sample into 6 M HCl solution at 60 ℃ for 30 min.

The *in situ* microstructure of the interfacial part between the ACL and AEM was observed by focused ion beam scanning electron microscopy (FIB-SEM, Helios 600i). The current for FIB ranged from 100 pA to 1 nA.

The internal three-dimensional structural information was obtained by computed micro-X-ray tomography (micro-CT, Zeiss Xradia Versa 620). Projection images of two dimensions were collected and reconstructed into a 3D image with a resolution of 0.33 μm per voxel.

3.2. X-ray diffraction (XRD) analysis

XRD (D/max-2550, Cu Kα radiation) measurements were conducted by powder diffractometer in the 2θ range of 5-90°.

3.3. X-ray photoelectron spectroscopy (XPS) analysis

XPS (PHI Quantera II, Japan) was conducted to determine the oxidation state of the different species by using an Al Kα radiation with the C 1s peak at 284.8 eV.

3.4. ACL/AEM interfacial strength analysis

The interfacial bonding strength of the MEAs was measured using an electronic universal material testing machine (WDW-100) by a peel-off test.

3.5. ACL/NF interfacial strength analysis

The catalyst/Ni foil interfacial strength was measured using an nano scratch tester (Bruker Hysitron TI980).

3.6. Optical contact angle

The optical contact angle was measured through the Kruss DSA30 equipment.

3.7. The measurements of gas bubble diameter

As shown in **Fig. S69**, the measurements of gas bubble diameter were conducted in a standard

three-electrode system. The photos of oxygen bubbles release were obtained by a high-speed charge-coupled device camera (X-Motion, AOS Technologies) mounted on a microscope (SZ-CTC, OLYMPUS).

3.8. Gas bubble adhesive force analysis

The interaction force between the gas bubbles and ACL interfaces was assessed by a surface tension meter (Date Physics DCAT25). The volume of the gas bubble was about 2 μL for each testing. A typ-ical gas bubble adhesive force measurements consisted of three processes. Process 1 referred to the CL surface approaching the air bubble, in process 2 the electrode surface interacted with the air bub-ble, and in process 3 the electrode surface separated from the air bubble.

3.9. Catalyst tarnsfer ratio analysis

The catalyst transfer ratio (T) was calculated by using the following equation: $T = (w_a\text{-}w_b)/(w_a\text{-}w_c) \times 100\%$. Where w_a, w_b and w_c represent substrate weight with catalyst layer, substrate weight with residual catalyst layer after transfer and substrate weight, respectively.

Half-cell test

All half-cell tests were conducted in a STE system in an O_2-saturated 1 M KOH electrolyte solution using an electrochemical workstation (Princeton Applied Research) with graphite rod counter electrode and a Hg/HgO reference electrode. For comparison, the IrO_2/Ni foil was prepared by spraying IrO_2 catalyst slurry on the Ni foil surface. To prepare the anode catalyst slurry, IrO_2 powder (10 mg) was mixed with DI water (200 μL), isopropyl alcohol (800 μL) and QAPPT ionomer (10 mg; 10 wt%). The ionomer ratio was 10 wt%. The IrO_2 loadings on Ni foil were controlled to be 2 mg cm^{-2}. The scanning speed of the linear sweep voltammetry (LSV) curve with 80% iR drop compensation was 5 mV s^{-1}, and the potential range was 1.2-1.8 V vs. RHE for OER. All measured potentials were referred to the reversible hydrogen electrode (RHE), according to the equation: $E_{RHE} = E_{Hg/HgO} +$

0.098 + 0.0592 pH. The pH value of 1 M KOH electrolyte is 14. ElS of the electrodes were obtained at 1.55 V vs. RHE in the frequency range of 100 kHz to 0.1 Hz with an AC potential amplitude of 10 mV. The electrochemical double-layer capacitance was evaluated based on the CV test under the potential window of 1.027-1.127 V (vs. RHE), and the scan rate was 20, 40, 60, 80, and 100 mV s^{-1}. The C_{dl} value was calculated according to the equation: $C_{dl} = \frac{(j_a - j_c)v}{2} = \frac{(j_a - |j_c|)v}{2} = \frac{\Delta j v}{2}$, in which j_a and j_c is the anodic and cathodic voltammetric current density, respectively, taken middle of the selected potential range, and v is the scan rate. Chronopotentiometry was applied to measure the long-term stability for OER activity.

Single-cell test

The AEM water electrolysis system comprised the as-prepared MEAs and liquid/gas diffusion layer (carbon paper for cathode; Ni foam for anode). The active area of the MEA was 5.0 cm^2. The single cell was fed with 1 M KOH or pure water as an electrolyte and was operated at 60 ℃. The AEM water electrolysis tests were performed using a Wuhan LAND electrochemical station. Polarisation curves without iR compensation were obtained by recording the current density in the voltage range of 1.1–2.4 V at 60 °C. EIS was performed at 1.6 V with an amplitude of 50 mV over the frequency range from 10 kHz to 0.1 Hz. The long-term durability testing of AEM water electrolysis systems was conducted at a constant current density of 1000 mA cm^{-2}. The overvoltgae of the kinetics, Ohm and mass transport can be calculated as follows.

$\eta_{ohm} = R_b \times j$

$\eta_{kin} = \alpha \times \log(j) + V_0$

$\eta_{mass} = V - 1.229 - \eta_{ohm} - \eta_{kin}$

Where R_b is the bulk resistance of the cell, j is a current density, α is the Tafel slope, V_0 is the cell voltgae at exchange current density, V is the cell voltage and 1.229 is the thermodynamic voltage required for water splitting.

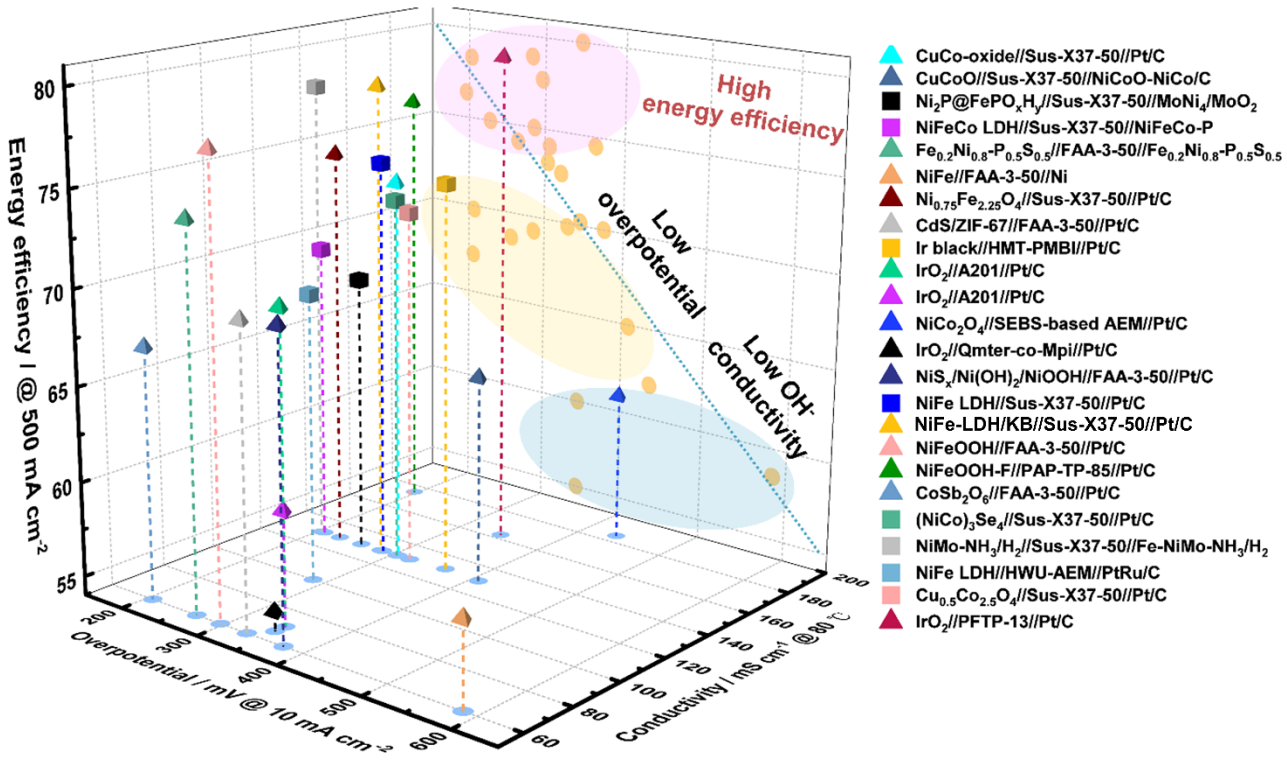

Fig. S1 | The relationship of electrode activity, membrane conductivity, and electrolysis performance of AEM water electrolysis. Overpotential (HER and OER) of electrocatalysts, hydroxide conductivity of AEMs and energy efficiency (at 500 mA cm^{-2}) of AEM water electrolysis (in 1 M KOH) comparison reported recently. The details on electrocatalysts and AEMs can be found in **Supplementary Table 1**.

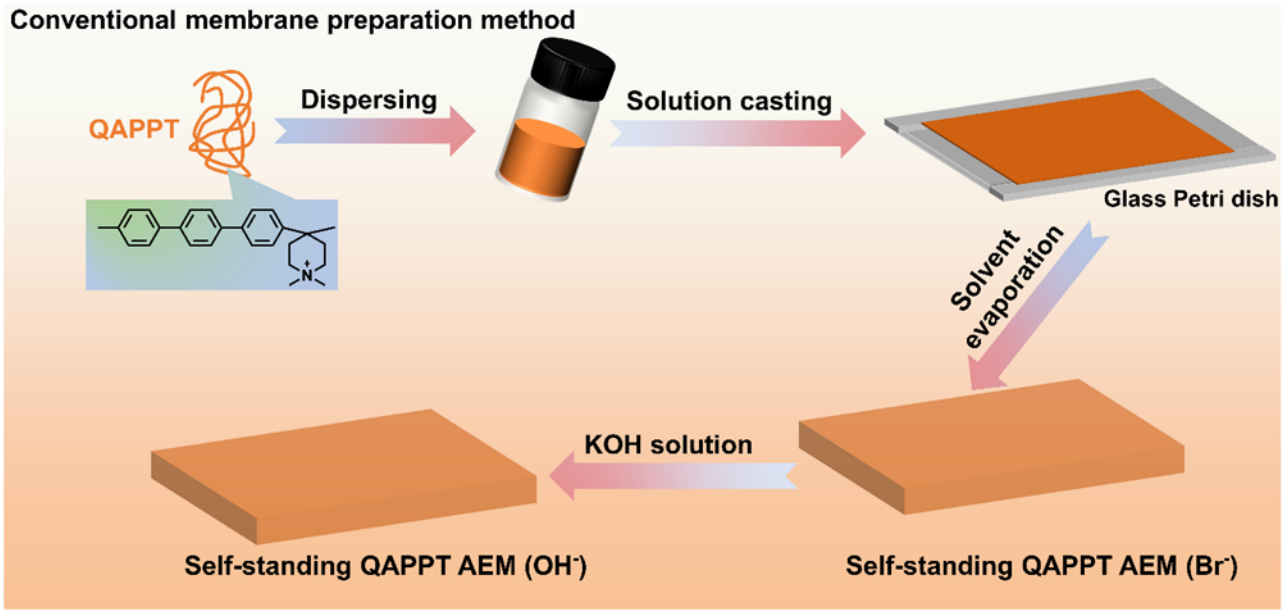

Fig. S2 | Schematic diagram of the conventional self-standing AEM preparation method. First, the AEM casting solutions were prepared by dissolving polymer in the solvent (such as DMOS, and DMAc) by vigorous stirring at 80 °C. The polymer solutions were cooled and then cast on a glass plate, which was dried in the oven at 60 °C for 36 h. After the solvent evaporated, the obtained AEMs were peeled off from the glass plate. Finally, the AEMs in Br^- form were immersed in KOH solution for 48 h at room temperature in nitrogen atmosphere to obtain the ones in OH^- form.

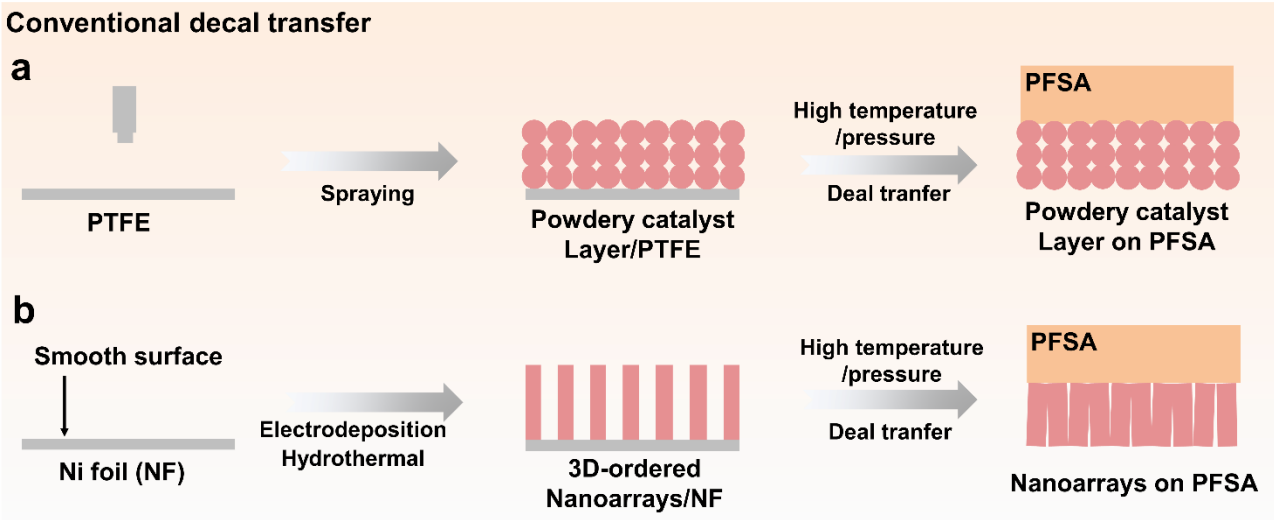

Fig. S3 | Schematic diagram of the conventional decal transfer preparation method. (a) First, the powdery electrocatalysts were prepared on PTFE substrate by spraying. Then, the powdery catalyst layer was transferred on a self-supported PFSA by hot pressing at a condition of 2 MPa and 120 ℃ for 5 min. (b) First, the 3D-ordered nanoarrays were prepared on Ni foil by different methods (such as electrodeposition and hydrothermal). Then, the 3D-ordered nanoarrays were transferred on a self-supported PFSA by hot pressing at a condition of 2 MPa and 120 ℃ for 5 min.

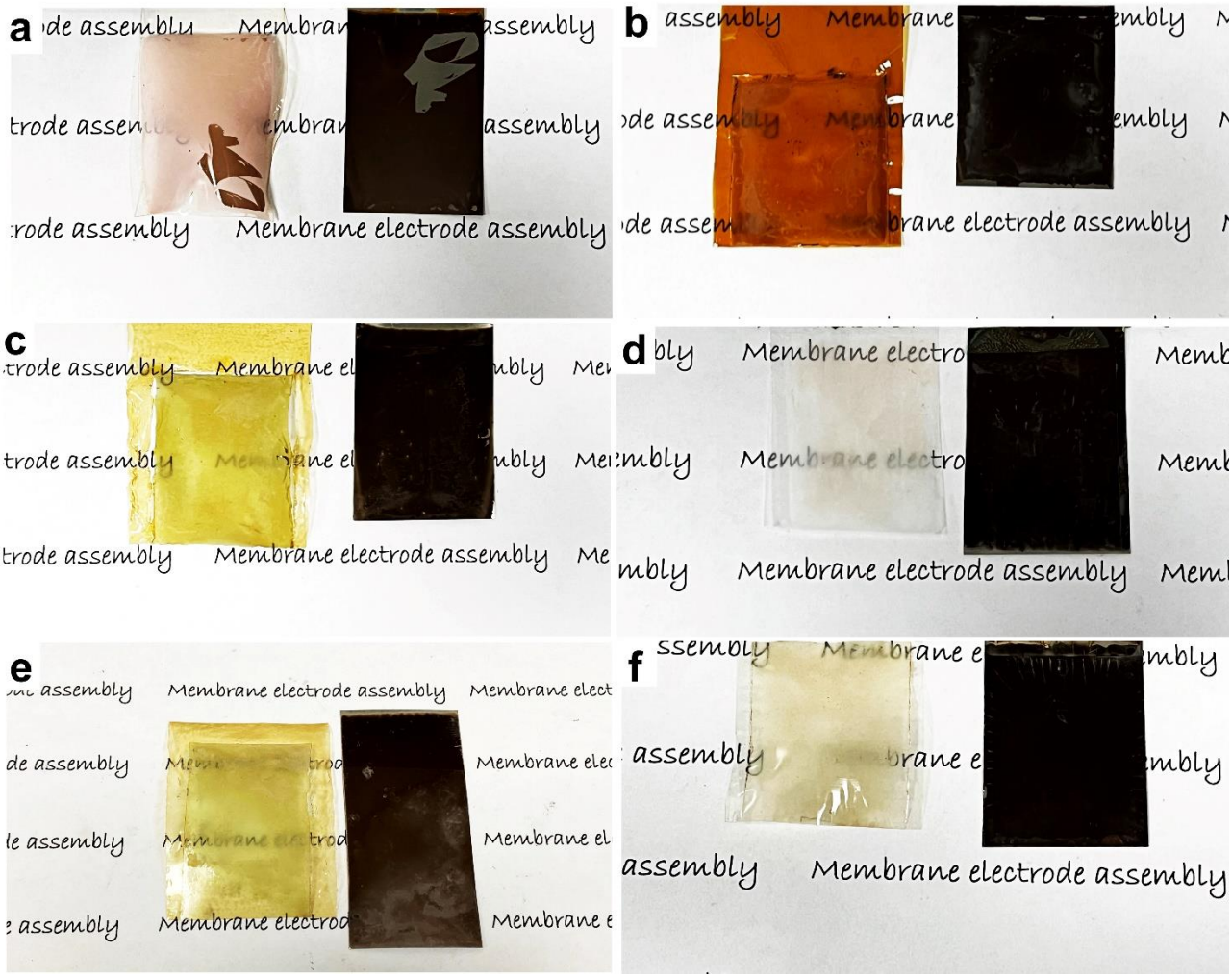

Fig. S4 | photographs of membranes and substrates after conventional decal transfer process at 120 °C and 2 MPa. (a) Nafion membrane and Ni foil substrate. The catalyst transfer ratio is 30 wt%. (b) PBI membrane and Ni foil substrate. The catalyst transfer ratio is 5 wt%. (c) FAA-3-50 membrane and Ni foil. The catalyst transfer ratio is 2 wt%. (d) Sustainion X37-50 membrane and Ni foil. The catalyst transfer ratio is 3 wt%. (e) QAPPT membrane and Ni foil. (f) PiperION membrane and Ni foil. The catalyst transfer ratio is 8 wt%.

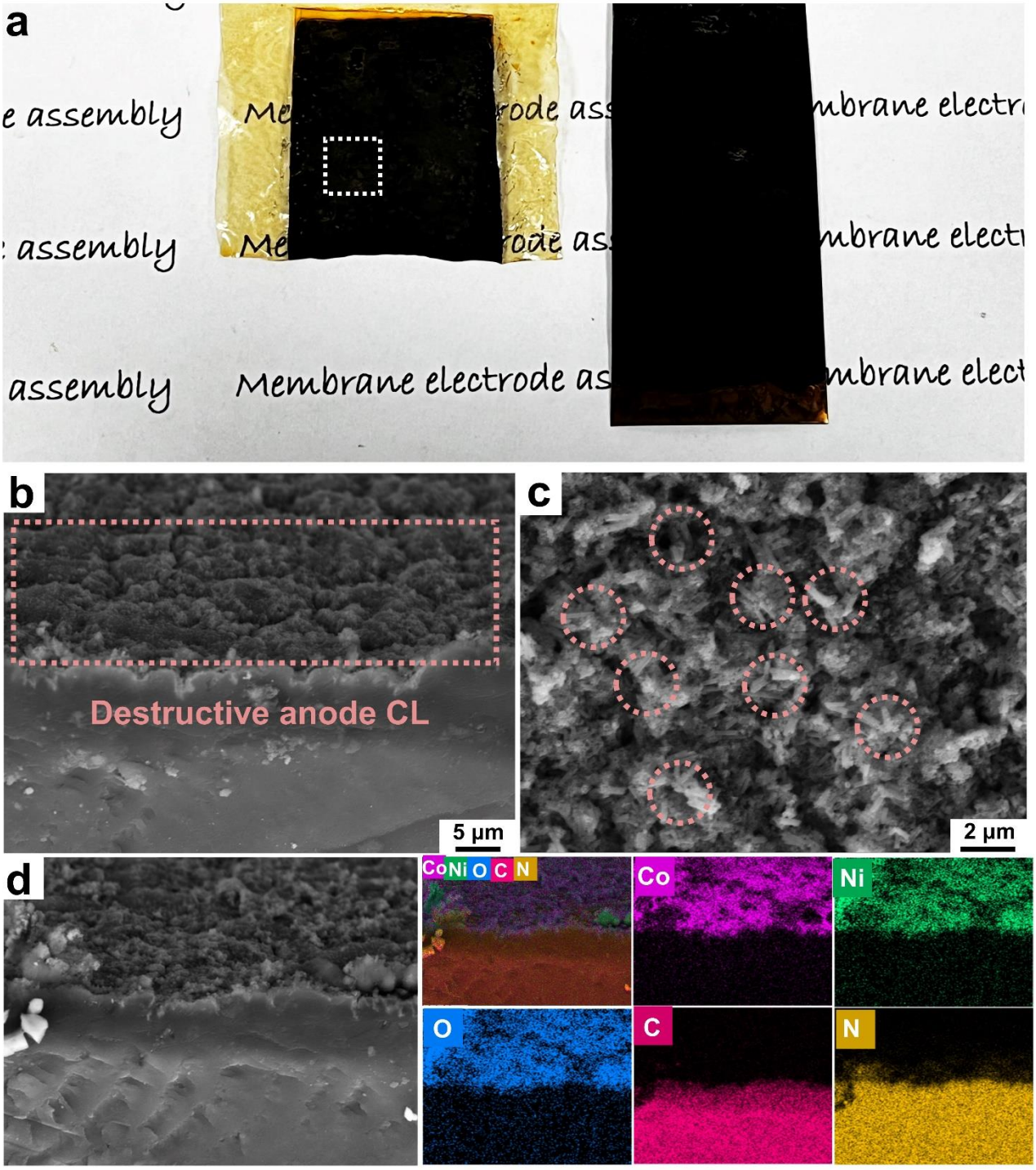

Fig. S5 | Characterization of conventional 3D-ordered MEA based on $NiCo_2O_4$ and PiperION AEM prepared via decal transfer method. (a) The photograph of conventional 3D-ordered MEA based on $NiCo_2O_4$. The catalyst transfer ratio is 60 wt%. (b) Cross-sectional FE-SEM and (c) surface images of conventional 3D-ordered MEA based on $NiCo_2O_4$. (d) EDS elemental mapping images of conventional 3D-ordered MEA based on $NiCo_2O_4$.

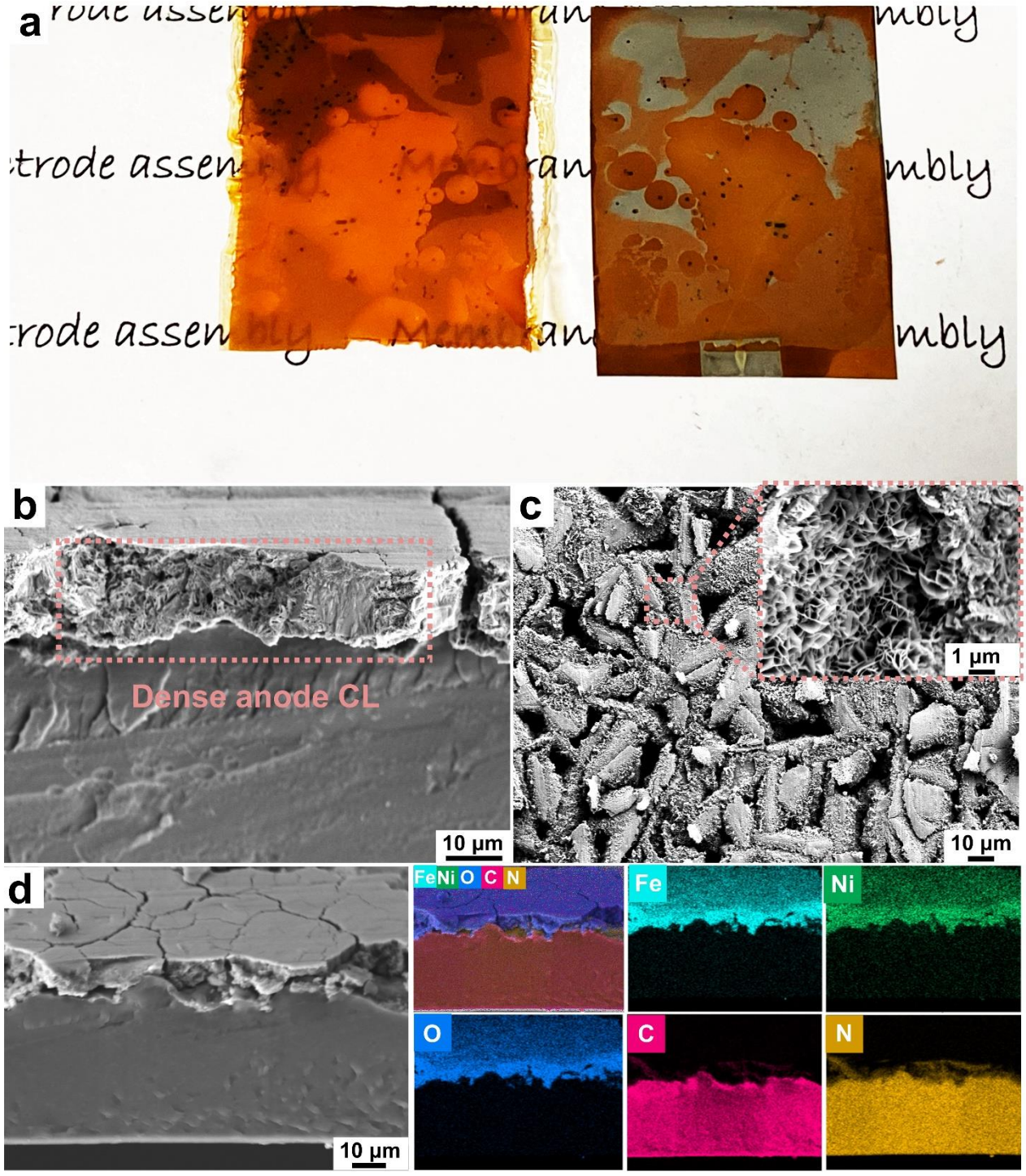

Fig. S6 | Characterization of conventional 3D-ordered MEA based on FeNi LDH and PiperION AEM prepared via decal transfer method. (a) The photograph of conventional 3D-ordered MEA based on FeNi LDH. The catalyst transfer ratio is 65 wt%. (b) Cross-sectional FE-SEM and (c) surface images of conventional 3D-ordered MEA based on FeNi LDH. (d) EDS elemental mapping images of conventional 3D-ordered MEA

based on FeNi LDH.

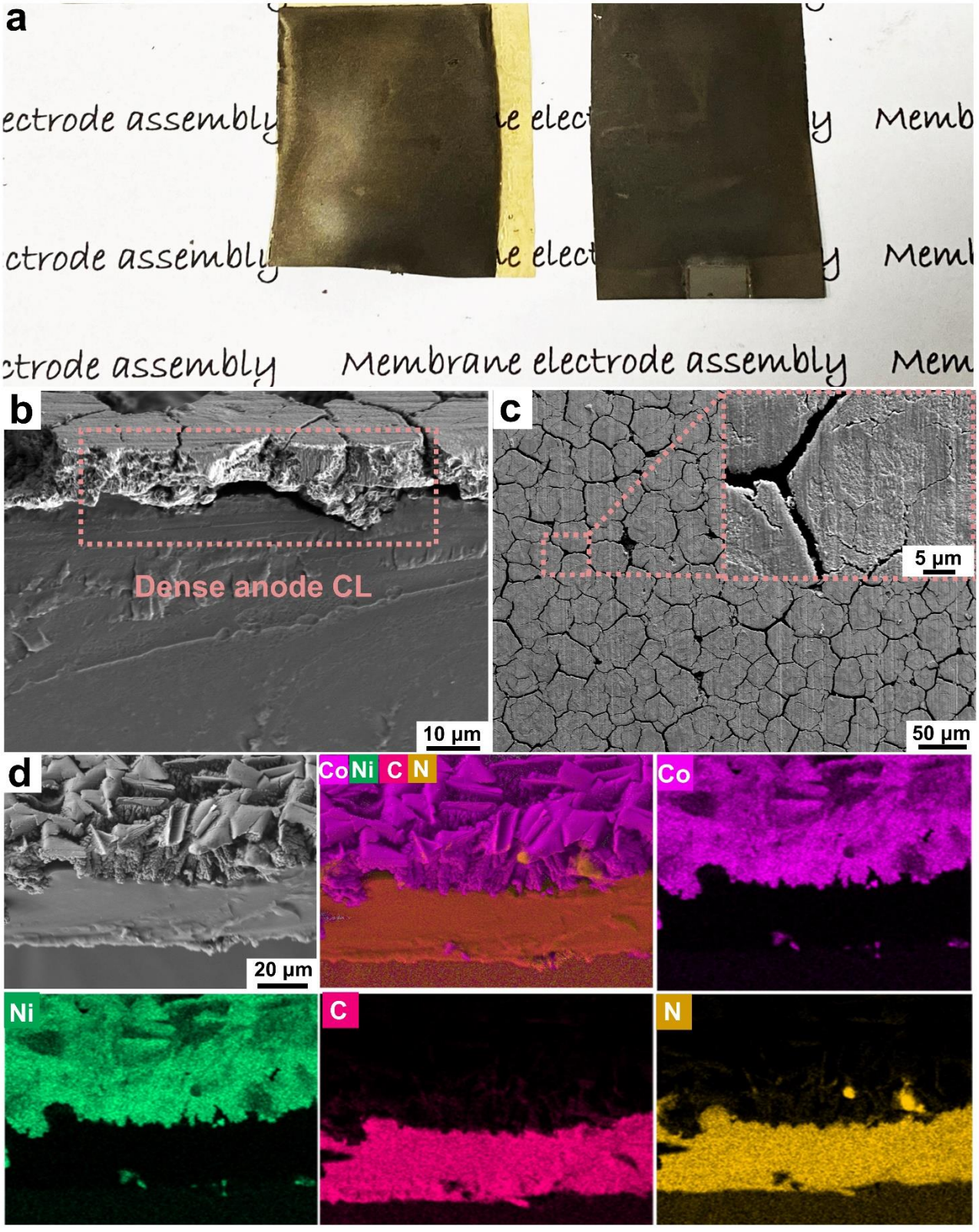

Fig. S7 | Characterization of conventional 3D-ordered MEA based on NiCo foam and PiperION AEM prepared via decal transfer method. (a) The photograph of conventional 3D-ordered MEA based on NiCo foam. The catalyst transfer ratio is 85 wt%. (b) Cross-sectional FE-SEM and (c) surface images of conventional

3D-ordered MEA based on NiCo foam. (d) EDS elemental mapping images of conventional 3D-ordered MEA based on NiCo foam.

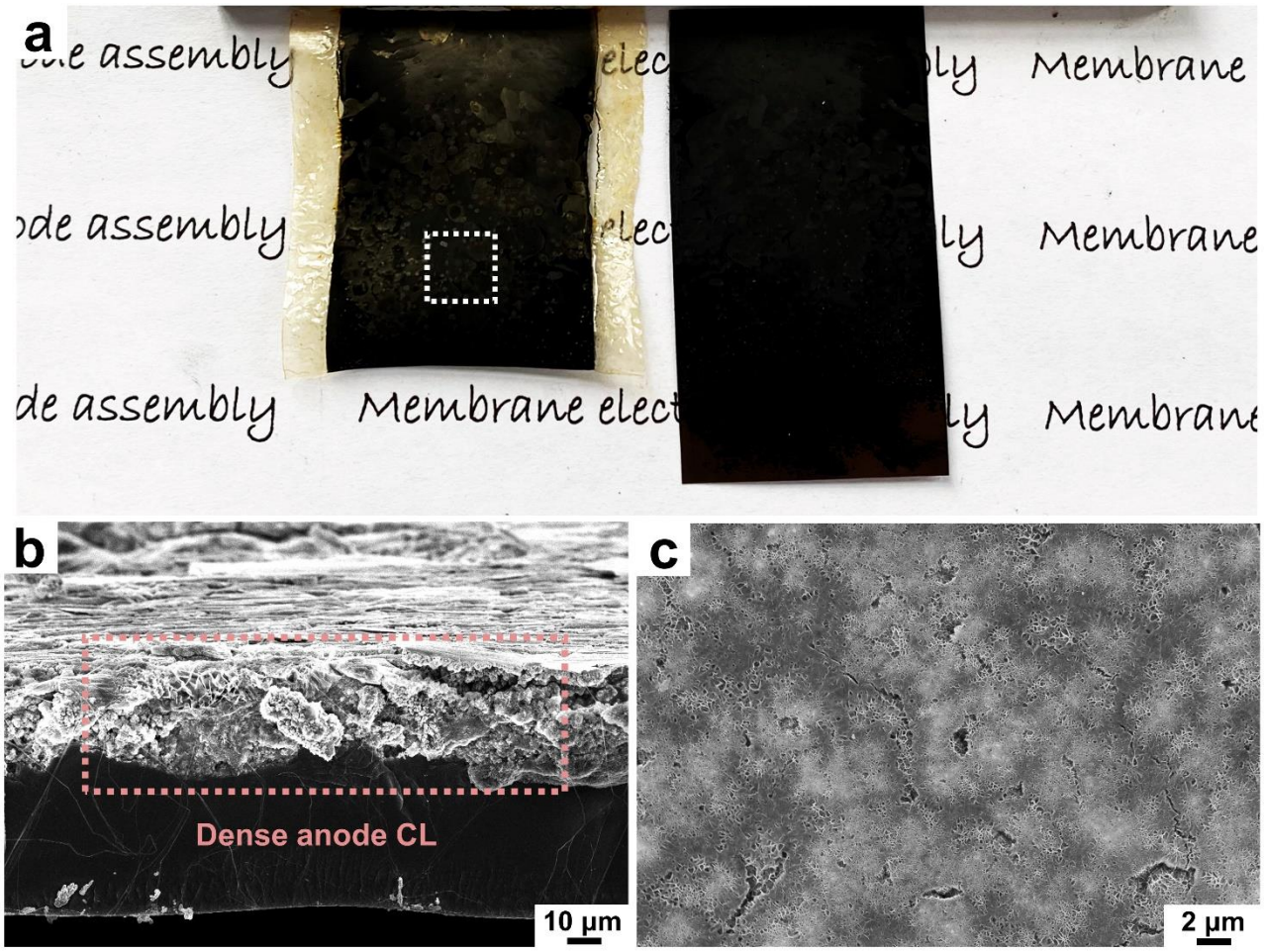

Fig. S8 | Characterization of conventional 3D-ordered MEA based on $NiCo_2O_4$@FeNi LDH and PiperION AEM prepared via decal transfer method. (a) The photograph of conventional 3D-ordered MEA based on $NiCo_2O_4$@FeNi LDH. The catalyst transfer ratio is 60 wt%. (b) Cross-sectional FE-SEM and (c) surface images of conventional 3D-ordered MEA based on $NiCo_2O_4$@FeNi LDH.

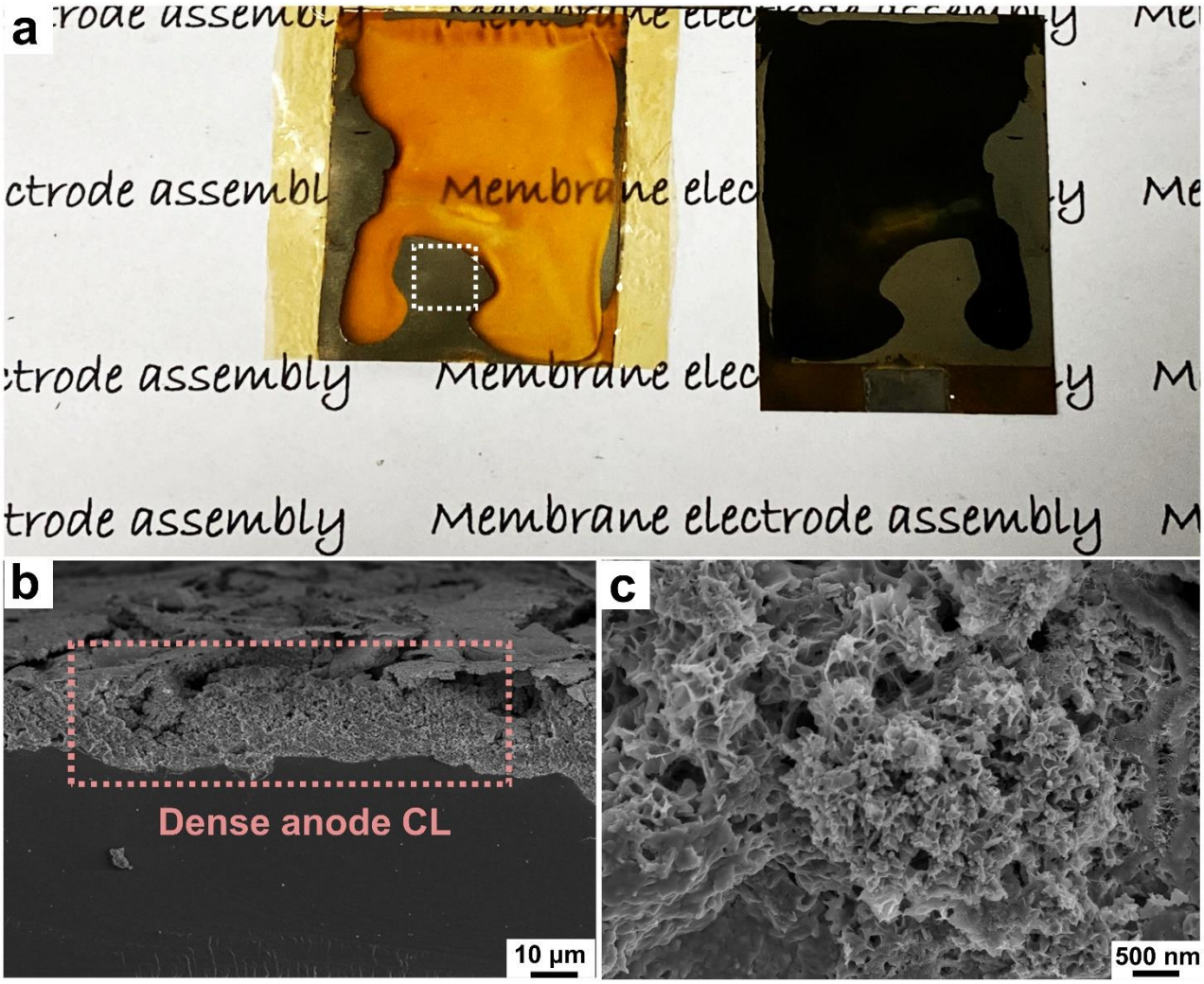

Fig. S9 | Characterization of conventional 3D-ordered MEA based on NiCo@FeNi LDH and PiperION AEM prepared via decal transfer method. (a) The photograph of conventional 3D-ordered MEA based on NiCo@FeNi LDH. The catalyst transfer ratio is 40 wt%. (b) Cross-sectional FE-SEM and (c) surface images of conventional 3D-ordered MEA based on NiCo@FeNi LDH.

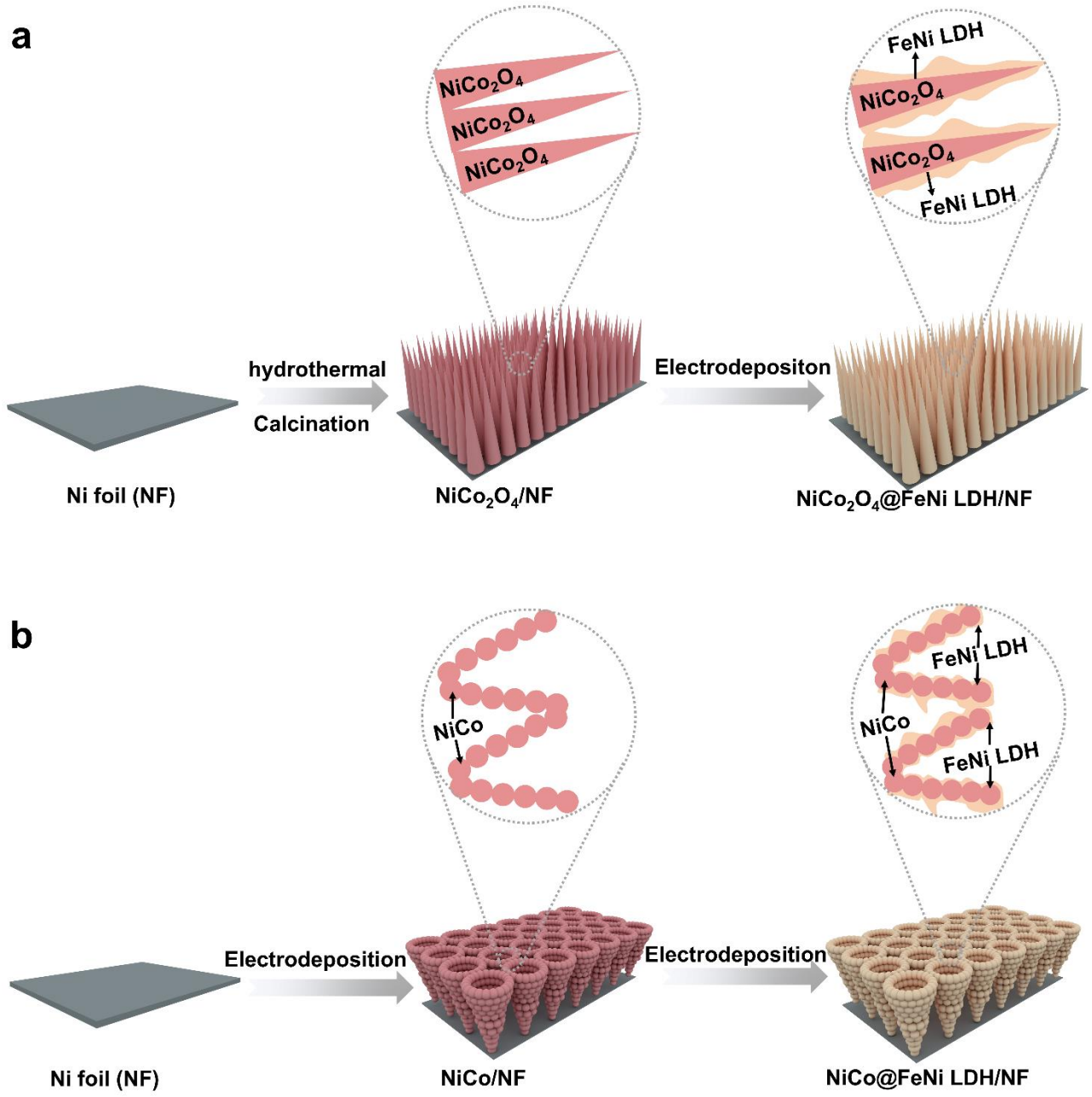

Fig. S10 | Schematic representation of the synthesis procedure for hierarchical nanoarrays on Ni foil: (a) $NiCo_2O_4$@FeNi LDH and (b) NiCo@FeNi LDH.

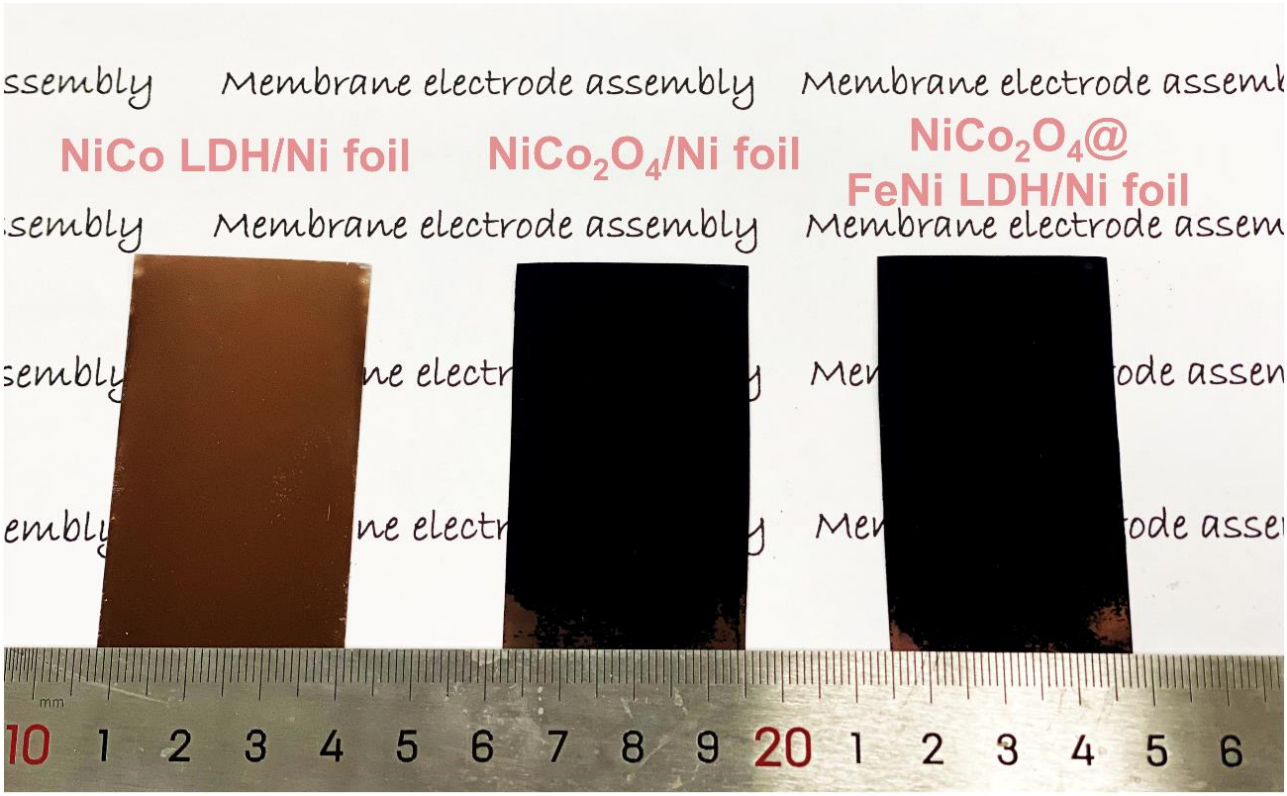

Fig. S11 | Digital images of NiCo LDH/Ni foil, $NiCo_2O_4$/Ni foil, $NiCo_2O_4$@FeNi LDH/Ni foil, NiCo/Ni foil, FeNi LDH/Ni foil and NiCo@FeNi LDH/Ni foil.

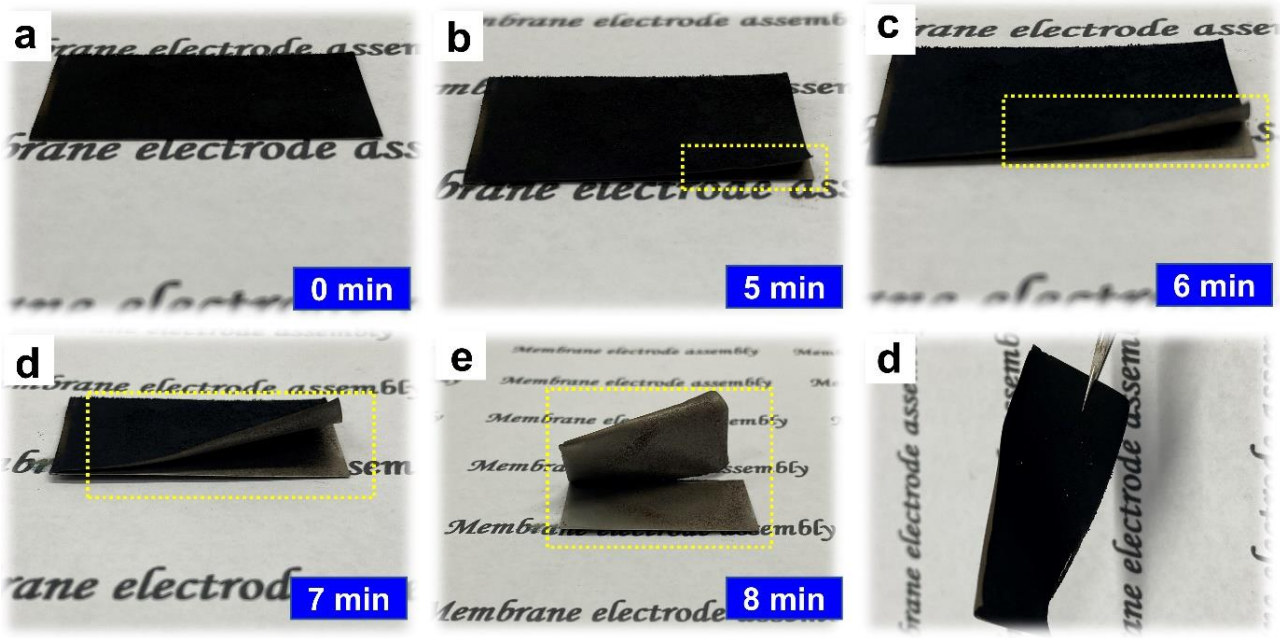

Fig. S12 | Novel swell-assisted transfer process for $NiCo_2O_4$@FeNi LDH/Ni foil. Digital images of the novel swell-assisted transfer process for the $NiCo_2O_4$@FeNi LDH anode CL: The AEM-coated $NiCo_2O_4$@FeNi LDH/Ni foil was heated at 50 °C for (a) 0 min, (b) 5 min, (c) 6 min, (d) 7 min, and (e) 8 min. (f) The digital image of obtained AEM-coated 3D-ordered anode CL based on $NiCo_2O_4$@FeNi LDH.

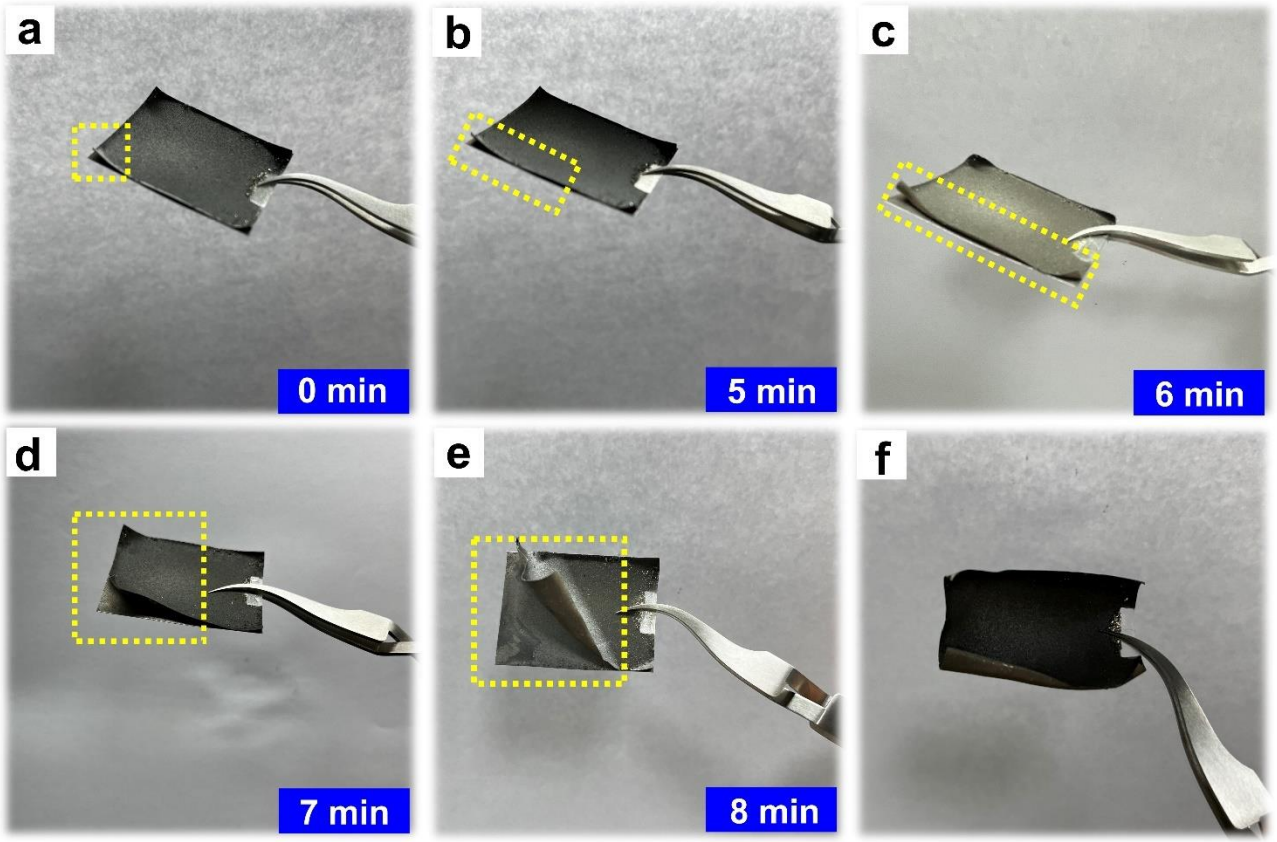

Fig. S13 | Novel swell-assisted transfer process for NiCo@FeNi LDH/Ni foil. Digital images of the novel swell-assisted transfer process for the NiCo@FeNi LDH anode CL: The AEM-coated NiCo@FeNi LDH/Ni foil was heated at 50 ℃ for (a) 0 min, (b) 5 min, (c) 6 min, (d) 7 min, and (e) 8 min. (f) The digital image of obtained AEM-coated 3D-ordered anode CL based on NiCo@FeNi LDH.

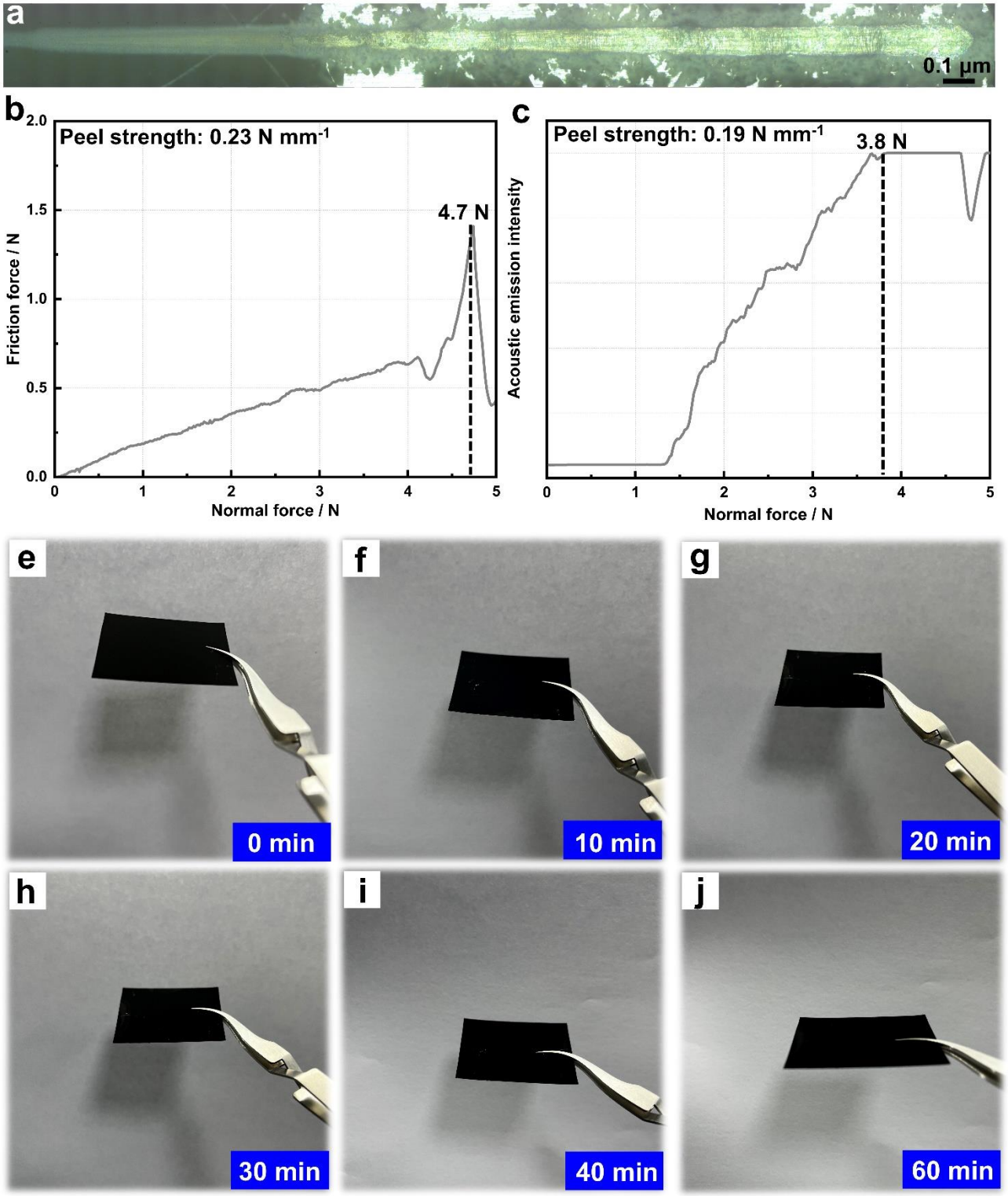

Fig. S14 | Interfacial strength characterization. (a) The photos of micro-scratches of IrO_2 coated on Ni foil. The (b) friction force-normal force curves and (c) acoustic signals of the IrO_2 coated on Ni foil. Digital images of the novel swell-assisted transfer process for the IrO_2 coated on Ni foil: The AEM-coated IrO_2 on Ni foil was heated at 50 ℃ for (e) 0 min, (f) 10 min, (g) 20 min, (h) 30 min, (i) 40 min, and (j) 60 min.

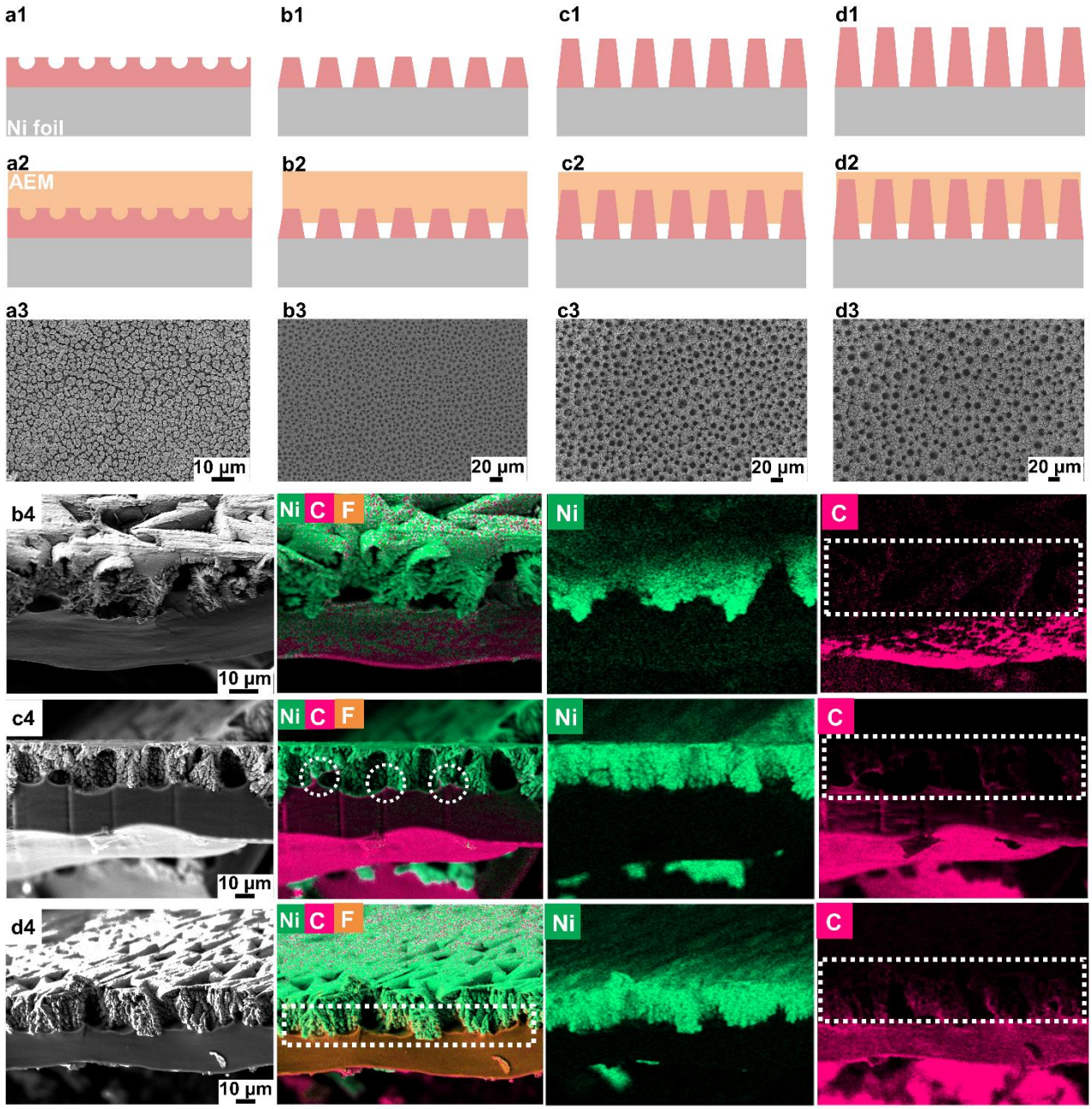

Fig. S15 | The impact of average pore diameter of porous Ni foam on swell-assisted transfer process. Schematic illustration of the cross-section morphologies of porous Ni foams prepared by hydrogen bubble template method at different current densities of (a1) 0.1 A cm^{-2}, (b1) 0.5 A cm^{-2}, (c1) 1.0 A cm^{-2}, and (d1) 2.0 A cm^{-2}. Schematic illustration of the cross-section morphologies of AEM-coated porous Ni foams by direct membrane deposition: (a2) AEM-coated porous Ni-0.1 foam, (b2) AEM-coated porous Ni-0.5 foam, (c2) AEM-coated porous Ni-1.0 foam, and (d2) AEM-coated porous Ni-2.0 foam. The surface SEM images of (a3) porous Ni-0.1 foam, (b3) porous Ni-0.5 foam, (c3) porous Ni-1.0 foam, and (d3) porous Ni-2.0 foam. The

cross-sectional SEM images and corresponding EDS mapping of (b4) AEM-coated porous Ni-0.5 foam, (c4) AEM-coated porous Ni-1.0 foam, and (d4) AEM-coated porous Ni-2.0 foam.

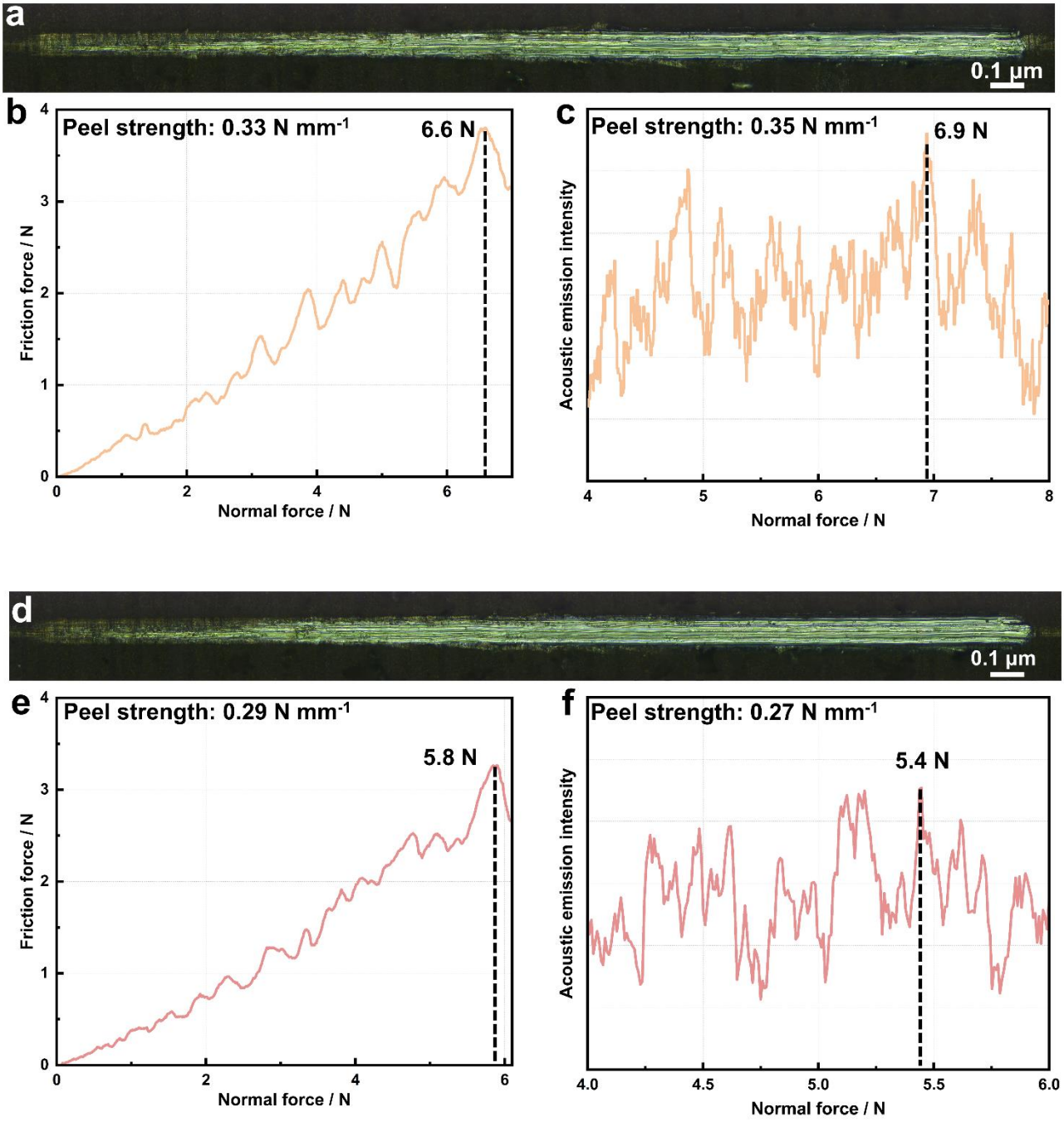

Fig. S16 | Interfacial strength characterization. (a) The photos of micro-scratches of $NiCo_2O_4$@FeNi LDH nanowire arrays adhesive on Ni foil. The (b) friction force-normal force curves and (c) acoustic signals of the $NiCo_2O_4$@FeNi LDH on Ni foil. (d) The photos of micro-scratches of NiCo@FeNi LDH nanowire arrays adhesive on Ni foil. The (e) friction force-normal force curves and (f) acoustic signals of the NiCo@FeNi LDH on Ni foil.

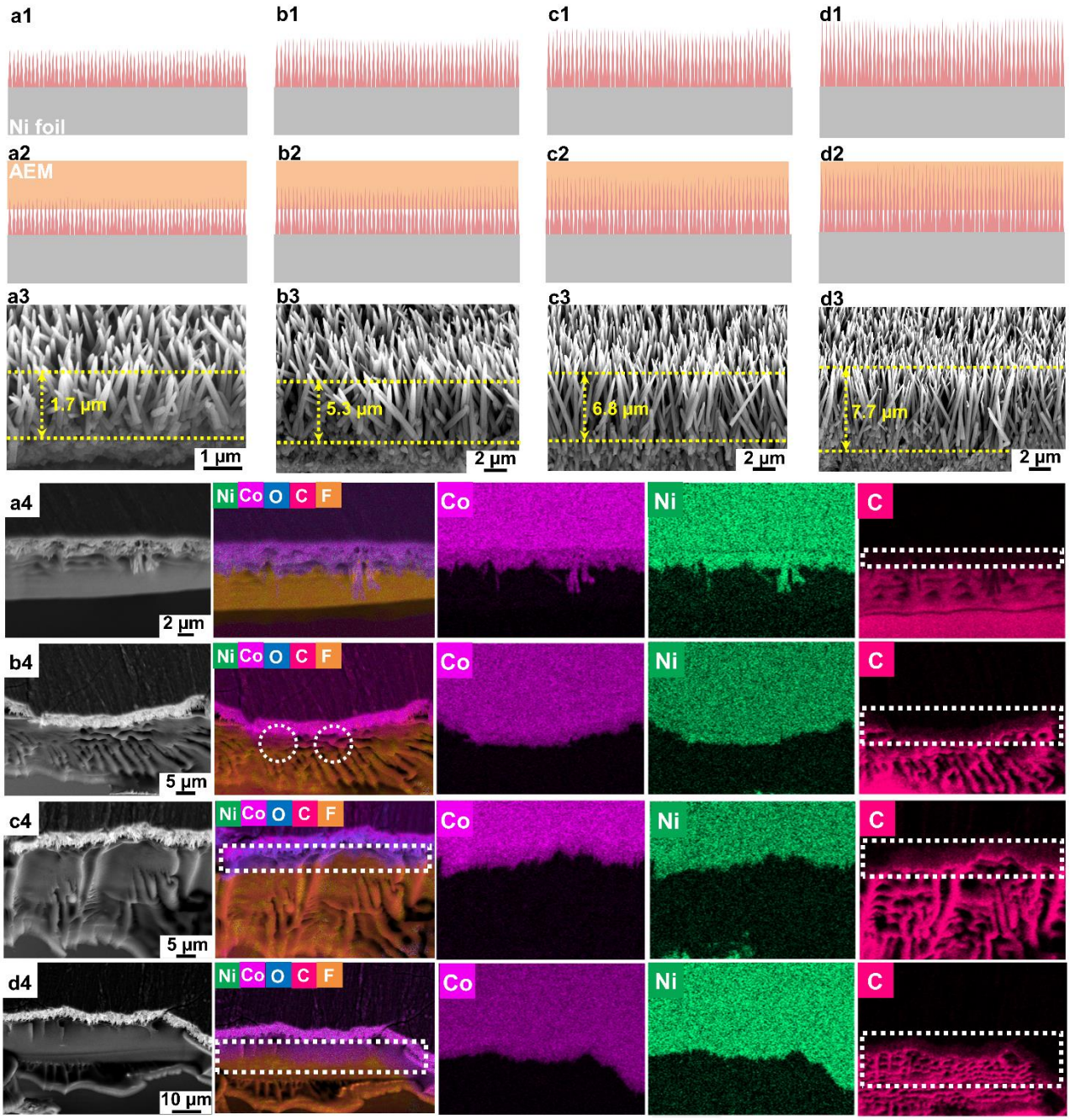

Fig. S17 | The impact of average pore depth of porous CoNi LDH nanowire arrays on swell-assisted transfer process. Schematic illustration of the cross-section morphologies of ordered CoNi LDH nanowire arrays (CoNi LDH NAs) prepared by hydrothermal method at different hydrothermal time of (a1) 1 h, (b1) 2 h, (c1) 4 h, and (d1) 6 h. Schematic illustration of the cross-section morphologies of AEM-coated ordered CoNi LDH nanowire arrays by direct membrane deposition: (a2) AEM-coated CoNi LDH NAs-1 h, (b2) AEM-coated CoNi LDH NAs-2 h, (c2) AEM-coated CoNi LDH NAs-4 h, and (d2) AEM-coated CoNi LDH NAs-6

h. The cross-section SEM images of (a3) CoNi LDH NAs-1 h, (b3) CoNi LDH NAs-2 h, (c3) CoNi LDH NAs-4 h, and (d3) CoNi LDH NAs-6 h. The cross-sectional SEM images and corresponding EDS mapping of (a4) AEM-coated CoNi LDH NAs-1 h, (b4) AEM-coated CoNi LDH NAs-2 h, (c4) AEM-coated CoNi LDH NAs-4 h, and (d4) AEM-coated CoNi LDH NAs-6 h.

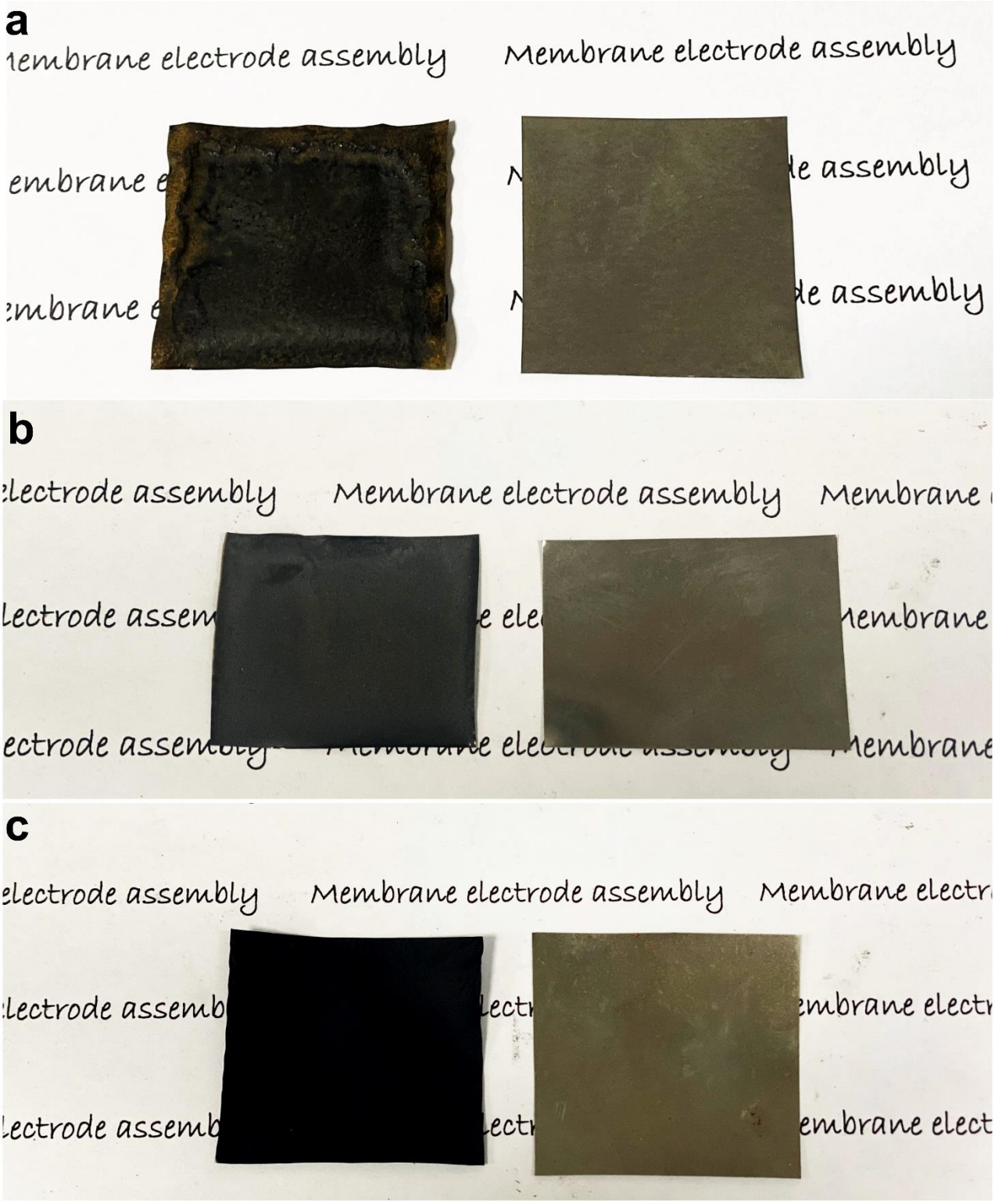

Fig. S18 | Digital images of 3D-ordered MEAs through the swell-assisted transfer method: (a) FeNi LDH anode CL (catalyst transfer ratio: 99.8%), (b) $NiCo_2O_4$@FeNi LDH anode CL (catalyst transfer ratio: 99.5%) and (c) NiCo@FeNi LDH anode CL (catalyst transfer ratio: 99.8%).

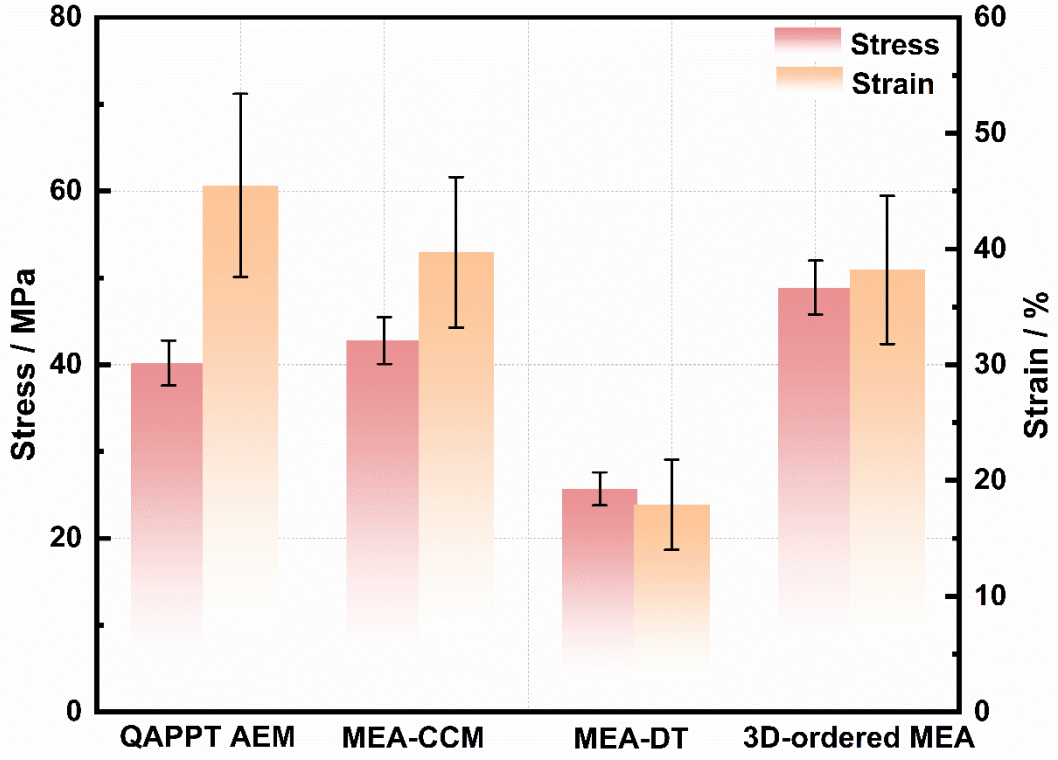

Fig. S19 | Mechanical properties including tensile strength and elongation at break of the QAPPT AEM, MEA-CCM, MEA-DT (MEA prepared by decal transfer method) and 3D-ordered MEA.

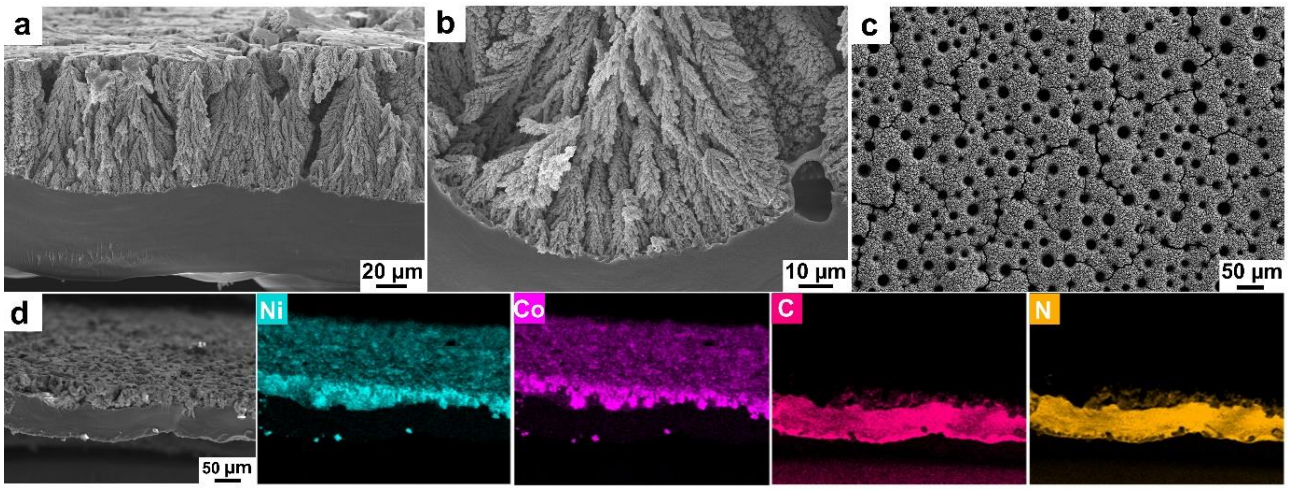

Fig. S20 | Characterization of novel 3D-ordered MEA (two-layered structure) based on NiCo foams and QAPPT AEM prepared via swell-assisted transfer method. Cross-sectional FE-SEM images of (a-b) anode CL with NiCo foams on a AEM. Surface FE-SEM image of (c) anode with NiCo foams. (d) The corresponding cross-sectional elemental mapping of anode CL with NiCo foams on a AEM.

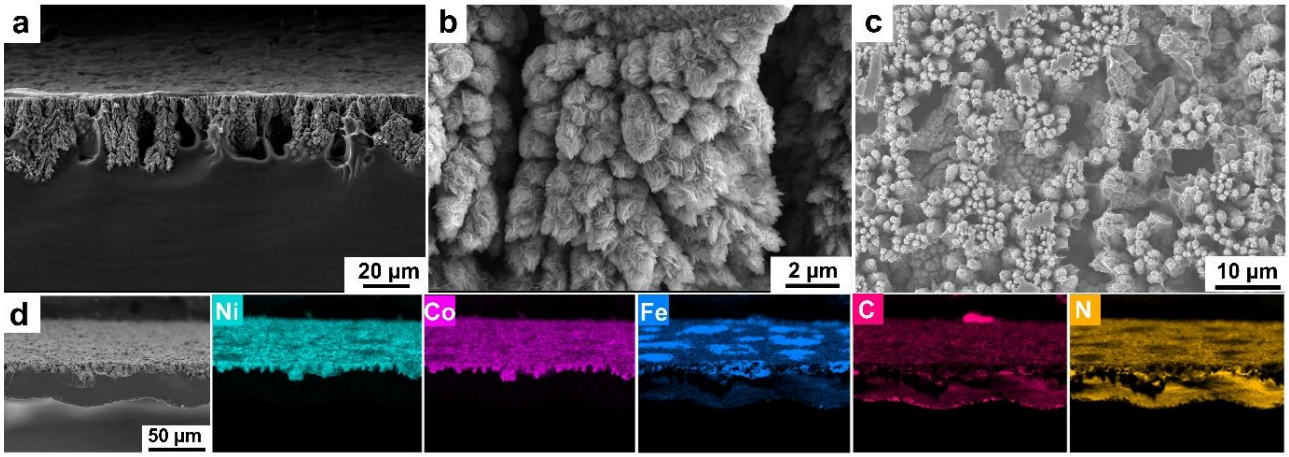

Fig. S21 | Characterization of novel 3D-ordered MEA (two-layered structure) based on NiCo@FeNi LDH foams and QAPPT AEM prepared via swell-assisted transfer method. Cross-sectional FE-SEM images of (a-b) anode CL with NiCo@FeNi LDH foams on a AEM. Surface FE-SEM image of (c) anode with NiCo@FeNi LDH foams. (d) The corresponding cross-sectional elemental mapping of anode CL with NiCo@FeNi LDH foams on a AEM.

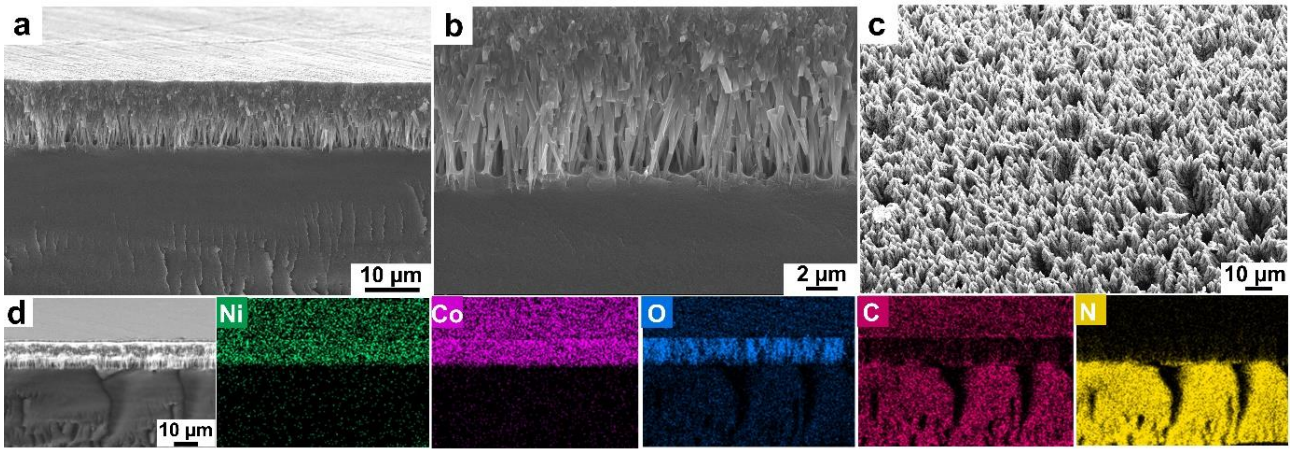

Fig. S22 | Characterization of novel 3D-ordered MEA (two-layered structure) based on $NiCo_2O_4$ naowire arrays and QAPPT AEM prepared via swell-assisted transfer method. Cross-sectional FE-SEM images of (a-b) anode CL with $NiCo_2O_4$ nanowire arrays on a AEM. Surface FE-SEM image of (c) anode with $NiCo_2O_4$ nanowire arrays. (d) The corresponding cross-sectional elemental mapping of anode CL with $NiCo_2O_4$ nanowire arrays on a AEM.

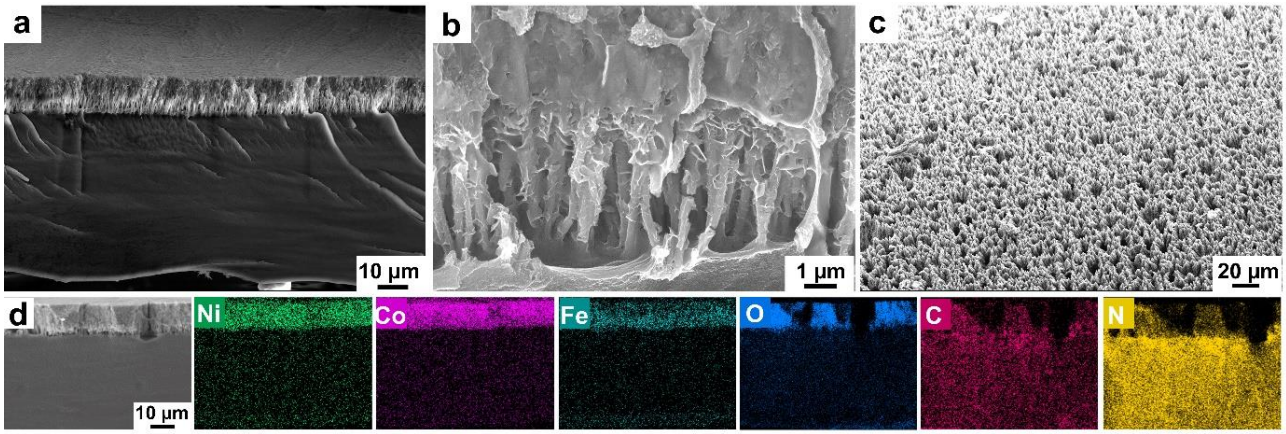

Fig. S23 | Characterization of novel 3D-ordered MEA (two-layered structure) based on $NiCo_2O_4$@FeNi LDH naowire arrays and QAPPT AEM prepared via swell-assisted transfer method. Cross-sectional FE-SEM images of (a-b) anode CL with $NiCo_2O_4$@FeNi LDH nanowire arrays on a AEM. Surface FE-SEM image of (c) anode with $NiCo_2O_4$@FeNi LDH nanowire arrays. (d) The corresponding cross-sectional elemental mapping of anode CL with $NiCo_2O_4$@FeNi LDH nanowire arrays on a AEM.

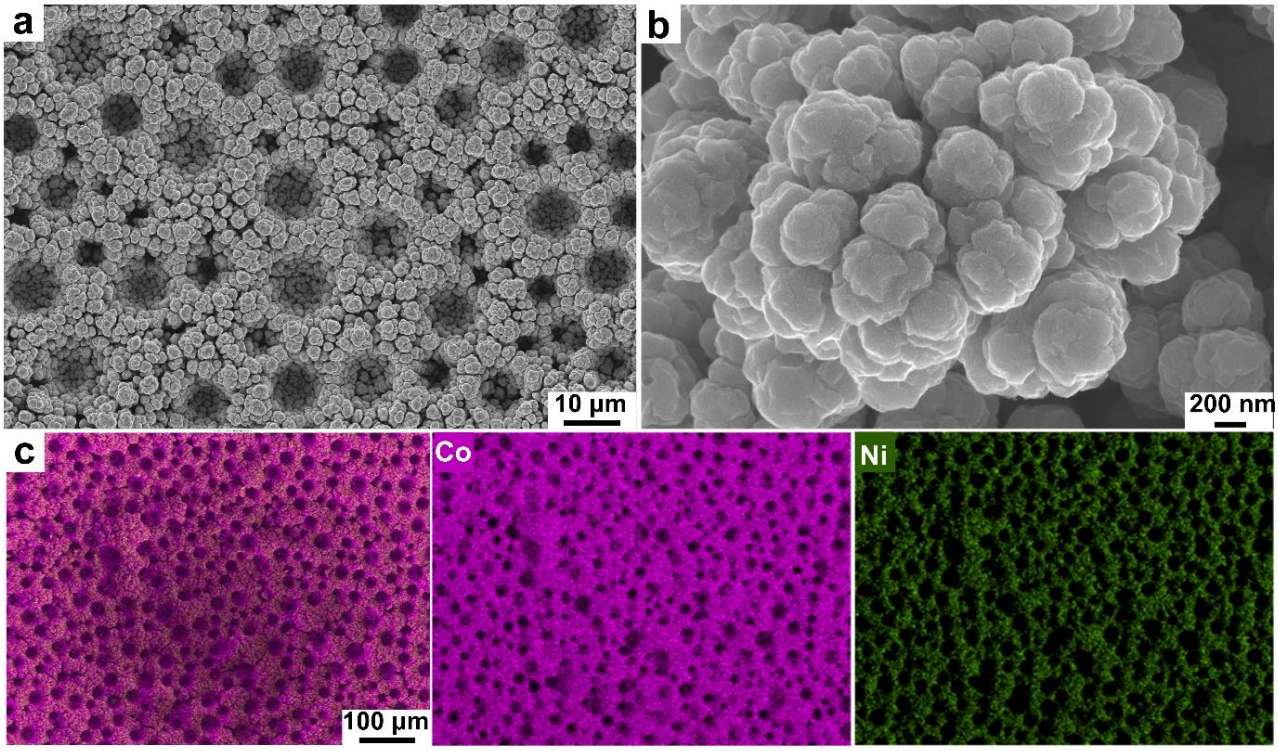

Fig. S24 | Characterization of NiCo porous foams. Structure and morphology of NiCo porous foams. (a-b) SEM images. (c) The corresponding element mapping of the NiCo porous foams.

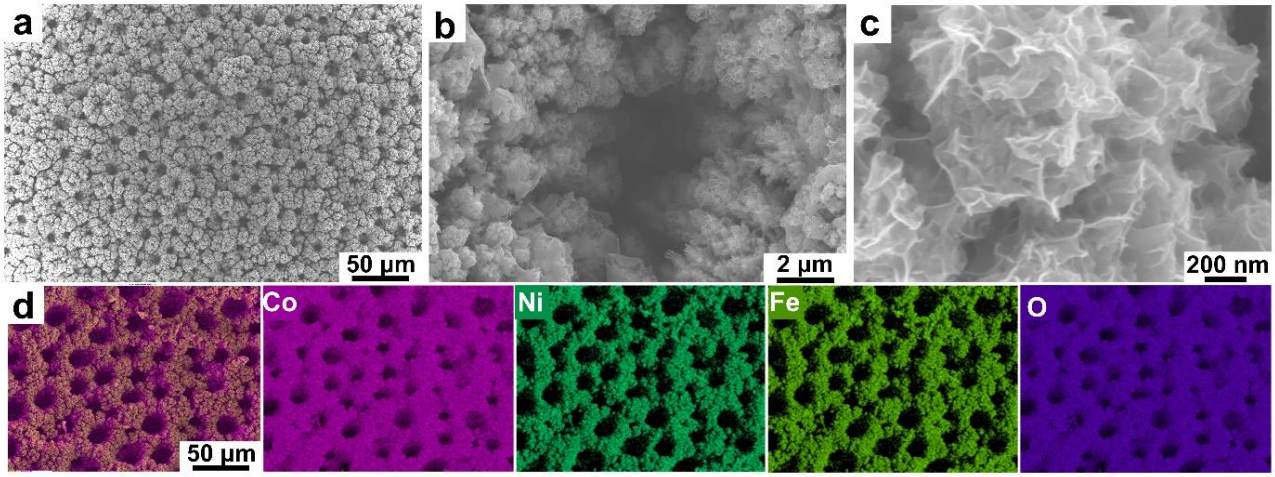

Fig. S25 | Characterization of NiCo@FeNi LDH porous foams. Structure and morphology of NiCo@FeNi LDH porous foams. (a-b) SEM images. (c) The corresponding element mapping of the NiCo@FeNi LDH porous foams.

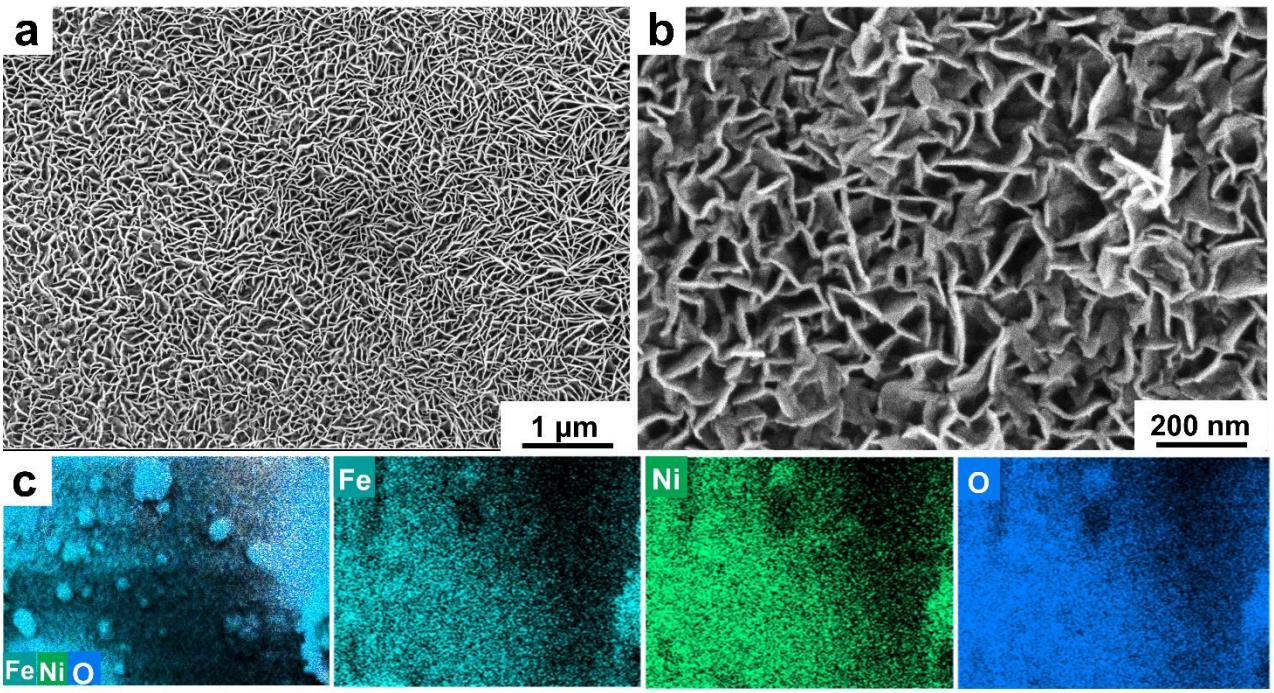

Fig. S26 | Characterization of FeNi LDH nanosheet arrays. Structure and morphology of FeNi LDH nanosheet arrays. (a-b) SEM images. (c) The corresponding element mapping of the FeNi LDH nanosheet arrays.

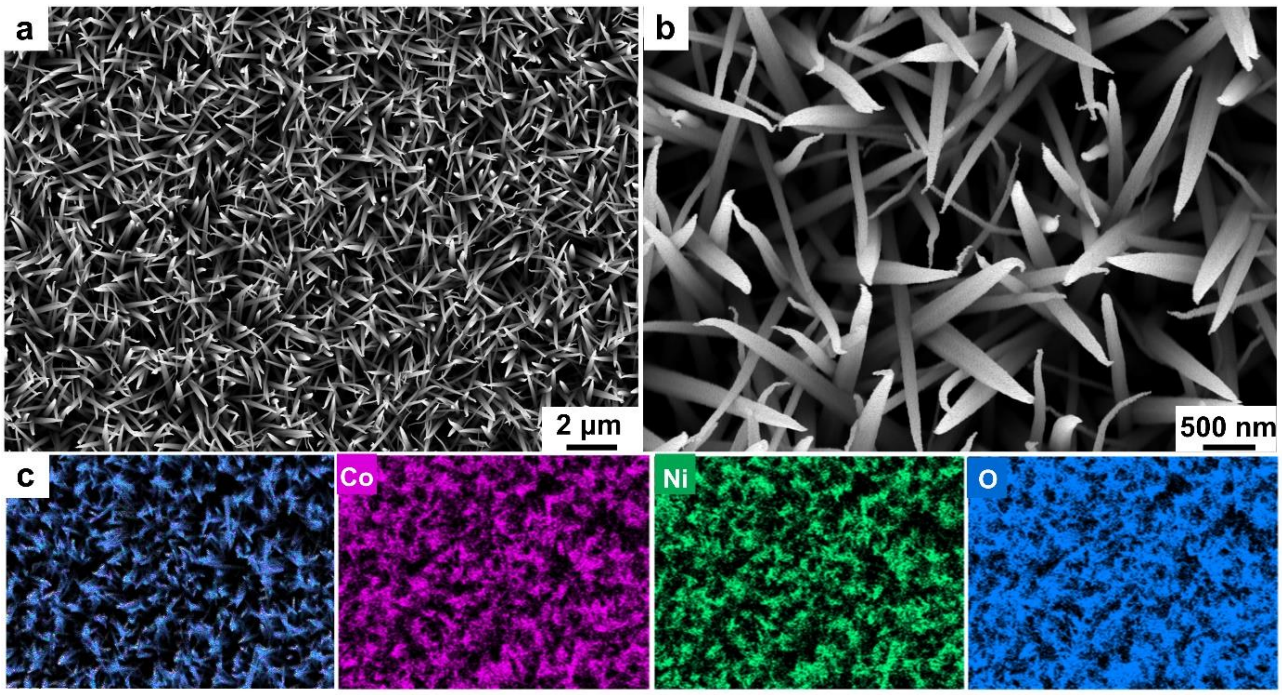

Fig. S27 | Characterization of NiCo LDH nanowire arrays. Structure and morphology of NiCo LDH nanowire arrays. (a-b) SEM images. (c) The corresponding element mapping of the NiCo LDH nanowire arrays.

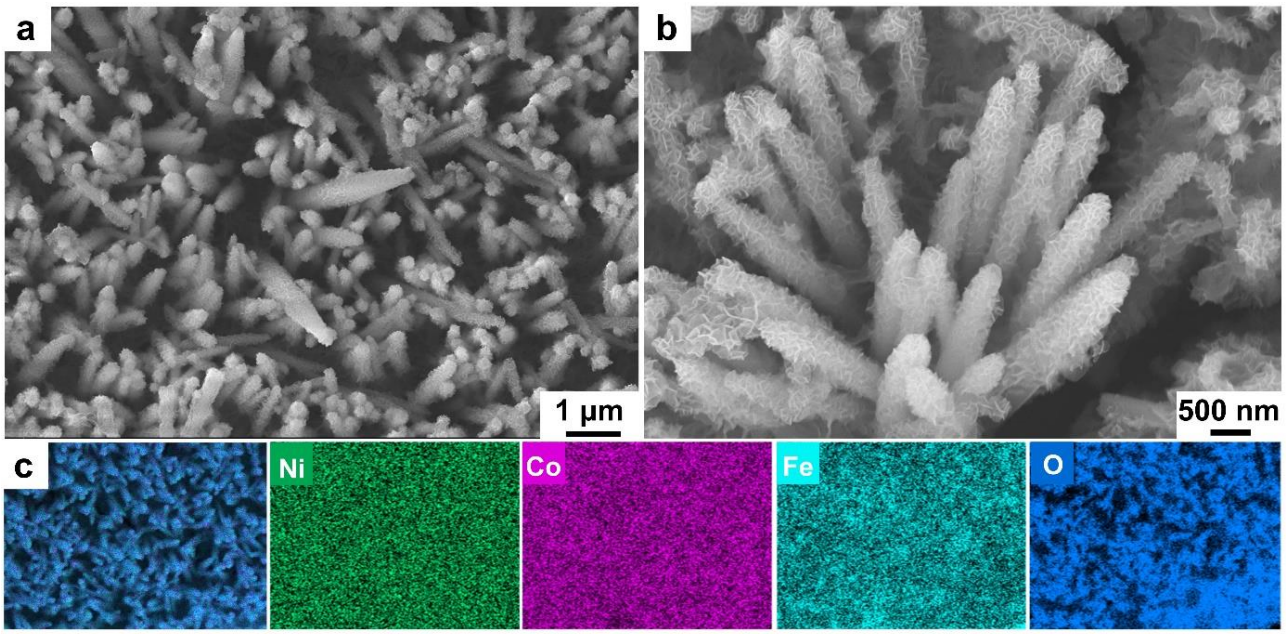

Fig. S28 | Characterization of $NiCo_2O_4$@FeNi LDH nanowire arrays. Structure and morphology of $NiCo_2O_4$@FeNi LDH nanowire arrays. (a-b) SEM images. (c) The corresponding element mapping of the $NiCo_2O_4$@FeNi LDH nanowire arrays.

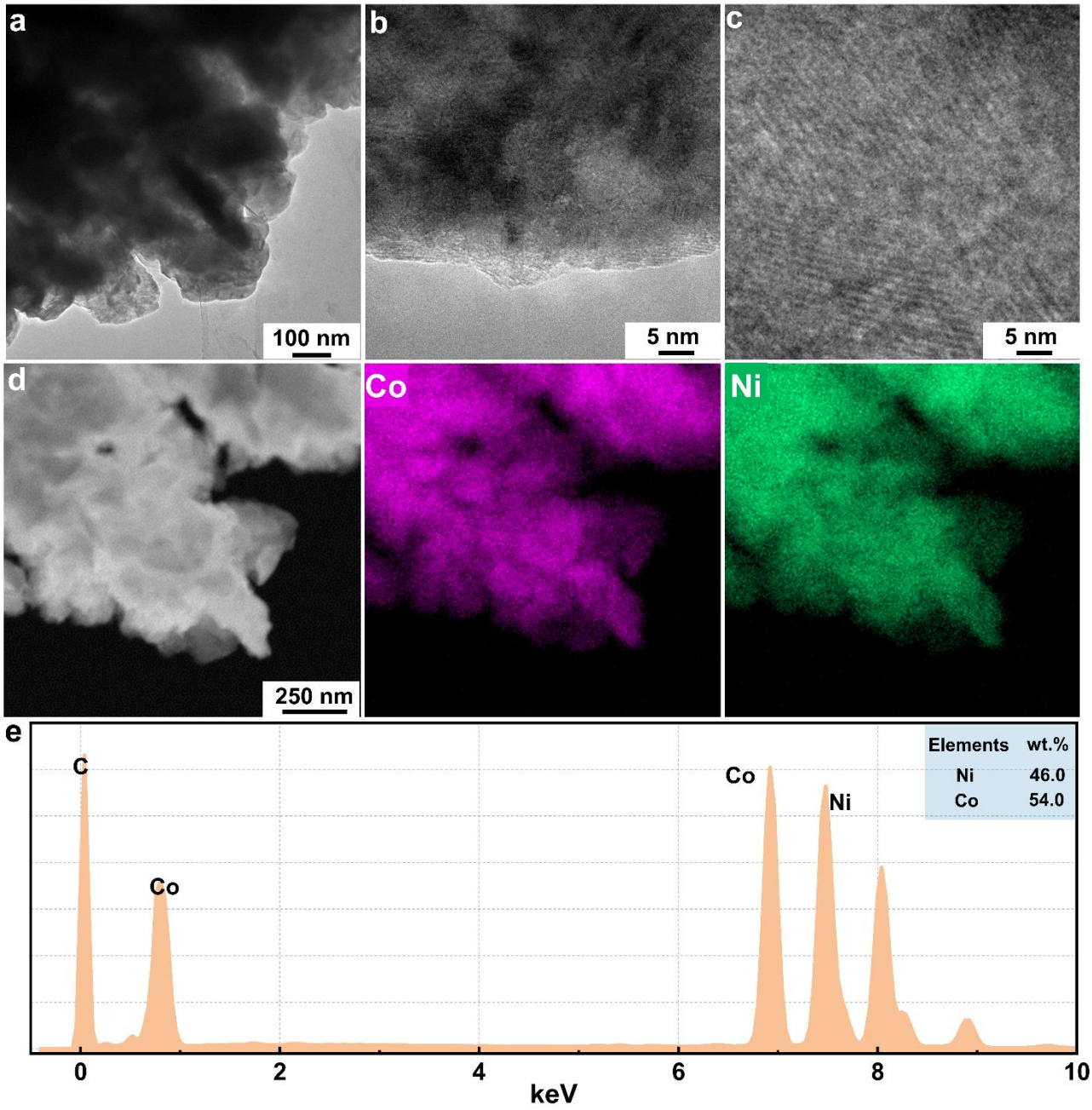

Fig, S29 | Structure and morphology of the NiCo porous foam. (a-c) TEM images. (d) The corresponding element mapping of the NiCo porous foam. (e) EDX spectra of the NiCo porous foam.

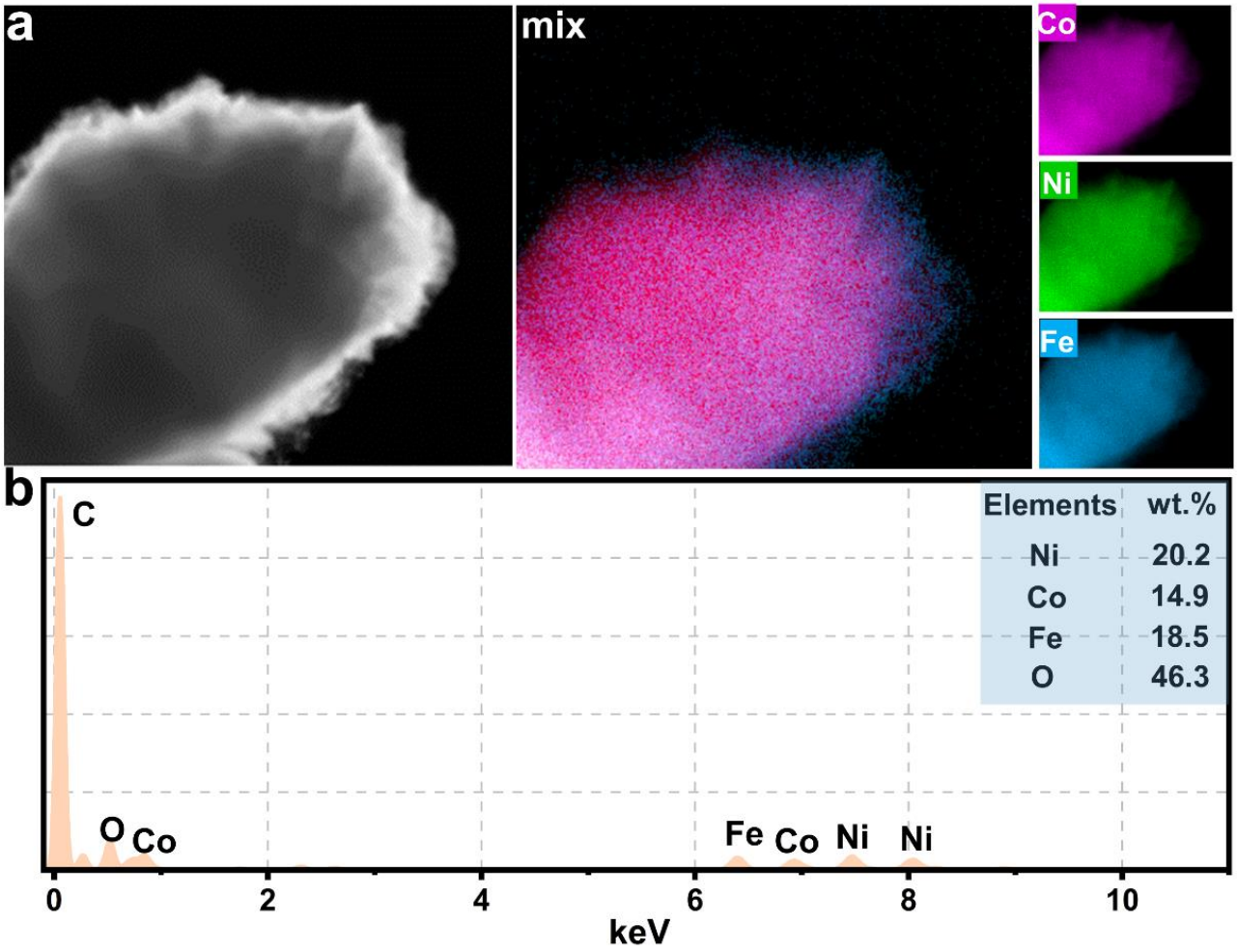

Fig. S30 | Structure and morphology of the NiCo@FeNi LDH porous foam. (a) TEM image and the corresponding element mapping of the NiCo@FeNi LDH porous foam. (b) EDX spectra of the NiCo@FeNi LDH porous foam.

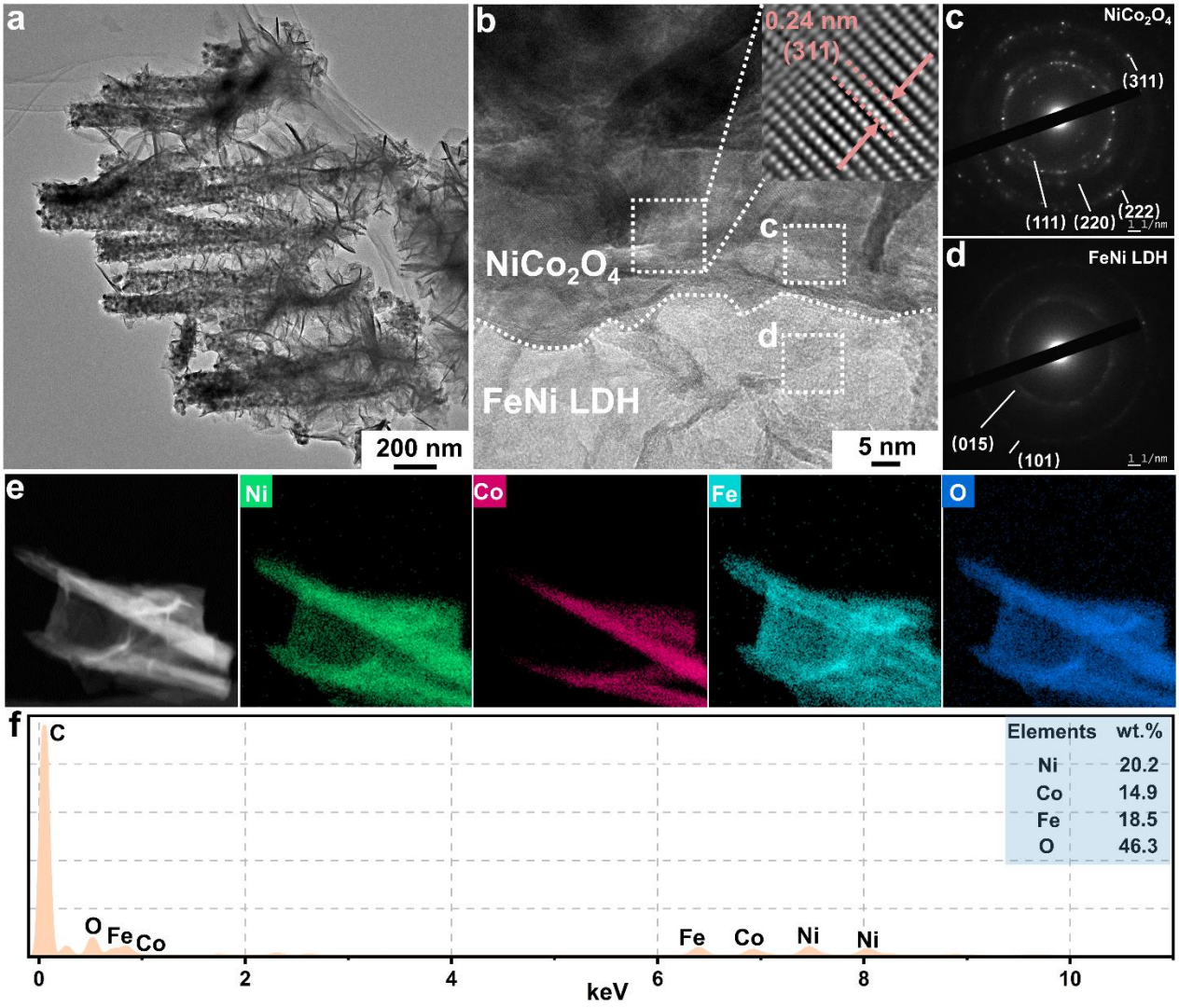

Fig. S31 | Structure and morphology of the $NiCo_2O_4$@FeNi LDH nanowire arrays. (a) TEM and (b) HRTEM images. (c-d) SAED images. (e) The corresponding element mapping of the $NiCo_2O_4$@FeNi LDH nanowire arrays. (f) EDX spectra of the $NiCo_2O_4$@FeNi LDH nanowire arrays.

Supplementary Note 1

Figure S31a exhibited the core-shell structure of $NiCo_2O_4$@FeNi LDH nanowires. The diameter of the $NiCo_2O_4$ nanowire was about 100 nm. In addition, the FeNi LDH nanosheets were coated on the surface of the $NiCo_2O_4$ nanowires homogeneously. The HRTEM of $NiCo_2O_4$@FeNi LDH in **Figure S31b** showed that the core phase has lattice spacings of 0.24 nm that attributed to the (311) plane of

$NiCo_2O_4$, and that the shell exhibited low-crystalline nanosheets due to the fast and low-temperature electrodeposition method. The SAED (**Figure S31c and S31d**) gave well-indexed diffraction rings of $NiCo_2O_4$ and FeNi LDH, which further confirmed the core-shell structure of $NiCo_2O_4$@FeNi LDH nanowires. **Figure S31e** showed the EDS element mapping. Homogeneous distributions of Fe, Ni, Co, and O are seen. The EDS spectrum further confirmed the coexistence of Fe, Ni, Co, and O elements (**Figure S31f**).

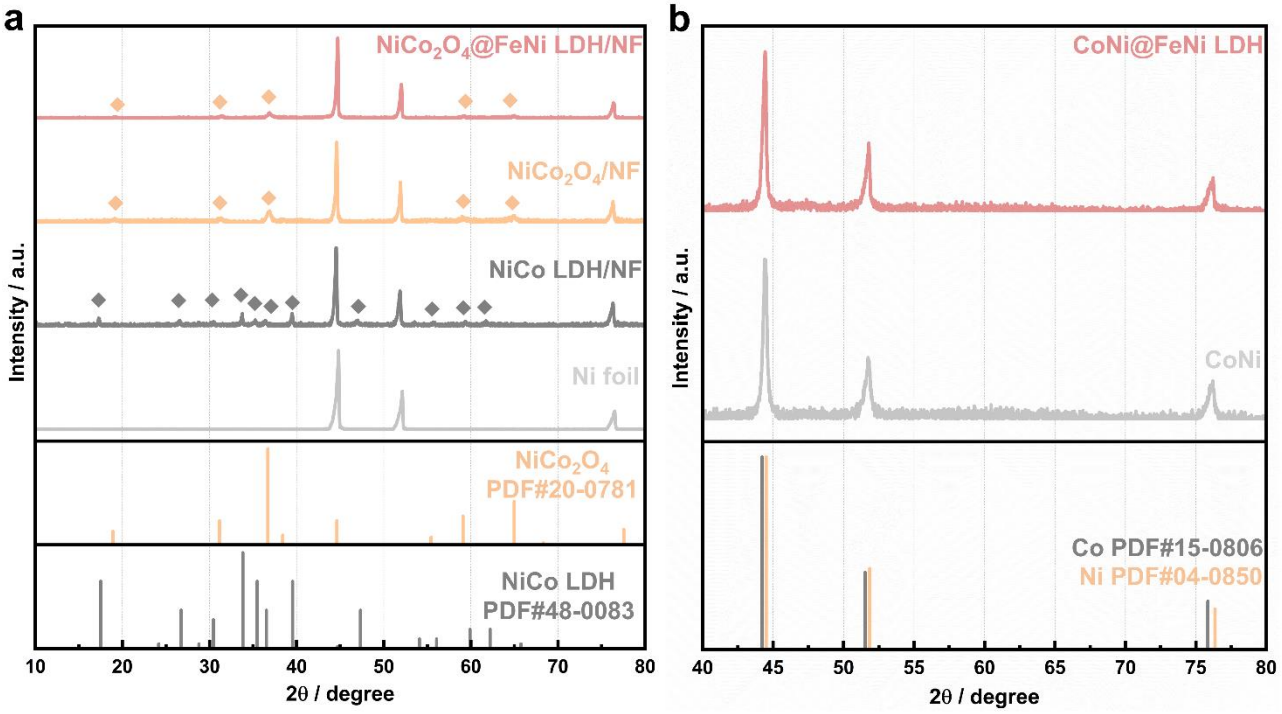

Fig. S32 | XRD patterns. (a) NiCo LDH/Ni foil, $NiCo_2O_4$/Ni foil and $NiCo_2O_4$@FeNi LDH/Ni foil. (b) CoNi and CoNi@FeNi LDH.

Supplementary Note 2

The crystal structure of different catalyst arrays was probed by XRD (**Figure S32a-b**). The XRD curves of NiCo LDH and $NiCo_2O_4$ corresponded to the standard PDF cards for NiCo hydroxide (JCPDS#48-0083) and $NiCo_2O_4$ (JCPDS#20-0781), respectively. For the XRD curve of $NiCo_2O_4$@FeNi LDH, the diffraction peaks located at 31.4°, 36.9°, 59.2°, 65.1°, respectively, corresponded to the (220), (311), (511), (440) planes of the spinel $NiCo_2O_4$. The absence of FeNi LDH reflections in the hierarchical $NiCo_2O_4$@FeNi LDH catalyst is attributed to the low crystallinity of the electrodeposited material. These results are in good agreement with the HRTEM results. XRD pattern of NiCo and NiCo@FeNi LDH in **Figure S32b** showed diffraction peaks at 44.5°, 51.8° and

76.4°, which are correlated to (111), (200) and (220) planes of Ni (JCPDS#04-0850), respectively. There are no other observable peaks besides the strong peaks of nickel substrate.

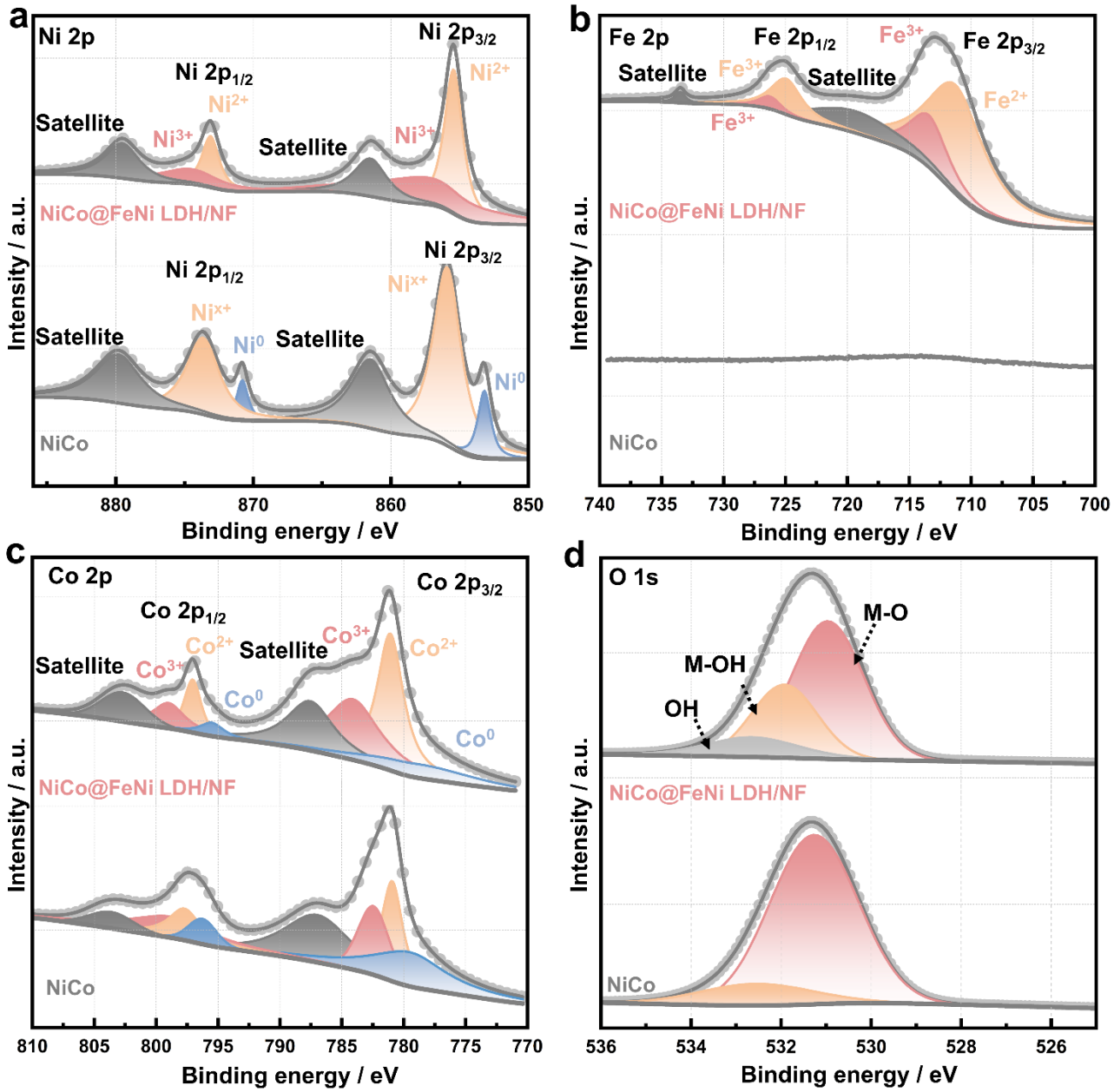

Fig. S33 | XPS survey spectra. (a) Ni 2p of NiCo/Ni foil and NiCo@FeNi LDH/Ni foil. (b) Fe 2p of NiCo/Ni foil and NiCo@FeNi LDH/Ni foil. (c) Co 2p of NiCo/Ni foil and NiCo@FeNi LDH/Ni foil. (d) O 1s of NiCo/Ni foil and NiCo@FeNi LDH/Ni foil.

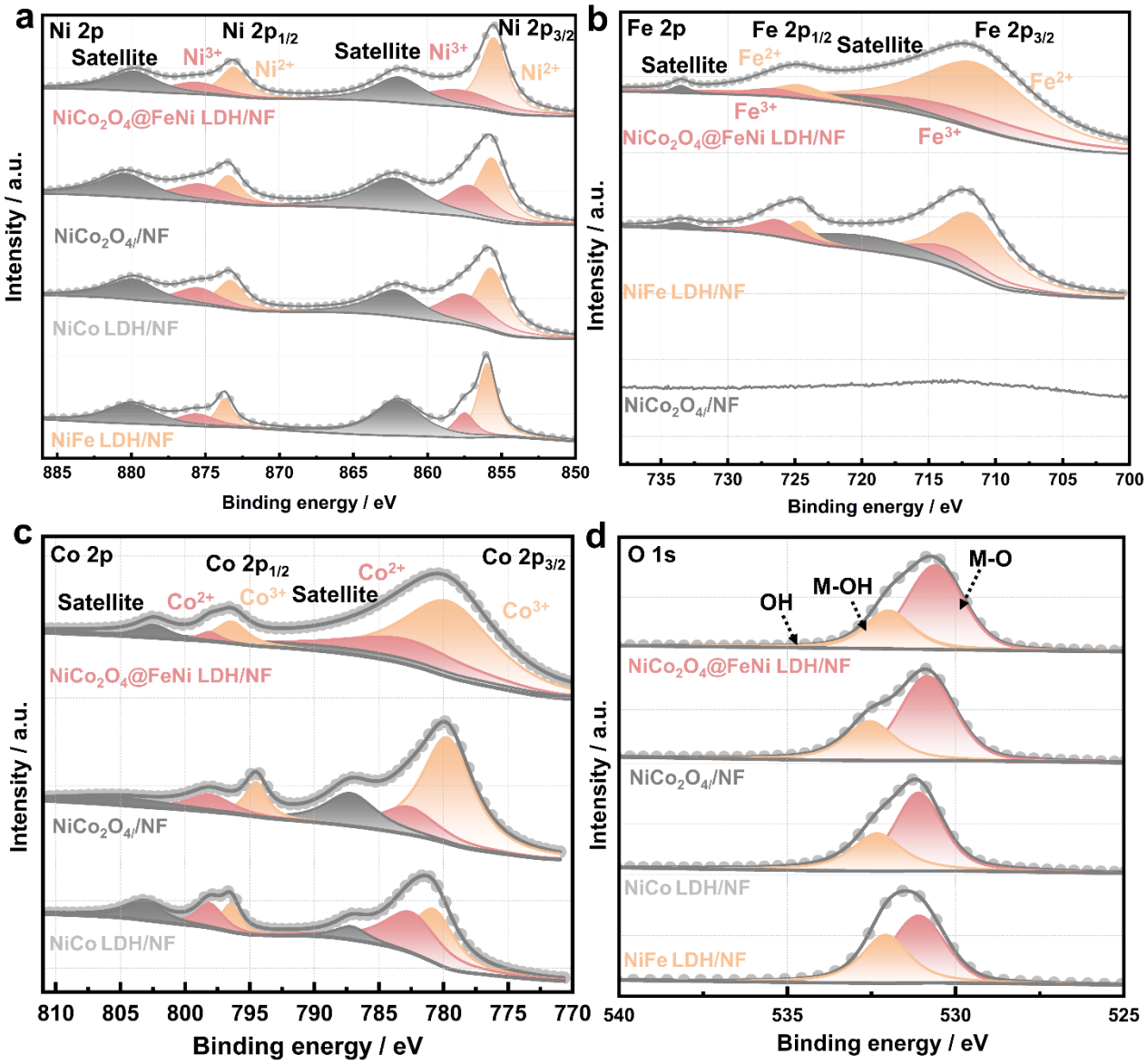

Fig. S34 | XPS survey spectra. (a) Ni 2p of NiFe LDH/Ni foil, NiCo LDH/Ni foil, $NiCo_2O_4$/Ni foil and $NiCo_2O_4$@FeNi LDH/Ni foil. (b) Fe 2p of $NiCo_2O_4$/Ni foil, NiFe LDH/Ni foil and $NiCo_2O_4$@FeNi LDH/Ni foil. (c) Co 2p of NiCo LDH/Ni foil, $NiCo_2O_4$/Ni foil and $NiCo_2O_4$@FeNi LDH/Ni foil. (d) O 1s of NiFe LDH/Ni foil, NiCo LDH/Ni foil, $NiCo_2O_4$/Ni foil and $NiCo_2O_4$@FeNi LDH/Ni foil.

Supplementary Note 3

X-Ray photoelectron spectroscopy (XPS) was performed to reveal the chemical composition and oxidation state of the hierarchical NiCo@FeNi LDH catalyst arrays. **Figure S33** shows the XPS spectrum of NiCo and NiCo@FeNi LDH. The peaks of Ni^0 $2p_{3/2}$ at 852.4 eV are corresponding to metallic nickel (Ni^0) (**Figure S33a**). And the peaks of Ni^{x+} $2p_{3/2}$ at 855.2 eV can be assigned to nickel oxides/hydroxides, because NiCo alloy may be partically oxidized when exposed to air. For the NiCo@FeNi LDH, the fitting peaks of Ni $2p_{3/2}$ and Ni $2p_{1/2}$ at 855.7 and 873.8 eV are characteristic of Ni^{2+}, and those at 862.9 and 880.8 eV were satellite peaks; the peaks at 857.5 and 875.1 eV correspond to Ni^{3+}. **Figure S33b** exhibits the deconvoluted Fe 2p spectrum of NiCo and NiCo@FeNi LDH. The Fe $2p_{3/2}$ and $2p_{1/2}$ peaks located at 711.6 eV and 725.5 eV are attributed to Fe^{3+}. As shown in **Figure S33c**, the Co 2p spectrum exhibits doublet peaks at 779.39 and 794.63 eV, which can be assigned to Co $2p_{3/2}$ and Co $2p_{1/2}$, respectively, and two satellite peaks are observed (786.33 and 803.01 eV). For the NiCo, deconvolution of Co $2p_{3/2}$ peak shows Co metallic state, Co^{2+} and Co^{3+} oxidation state located at 778.95 and 780.23 eV, respectively. It can be found that the intensity of peaks of Co^0 $2p_{3/2}$ at 778.95 eV in NiCo@FeNi LDH is weaker than that of NiCo, due to the reason that the chemical environment of Co atoms have changed after FeNi electrodeposition. The O 1s spectrum (**Figure S33d**) presented three deconvoluted peaks at 529.9, 531.9, and 533.4 eV, which can be attributed to the typical metal–oxygen bonds, oxygen in the hydroxide group, and chemisorbed water molecules, respectively.

Figure S34 shows the XPS spectrum of NiFe LDH/Ni foil, NiCo LDH/Ni foil, $NiCo_2O_4$/Ni foil and $NiCo_2O_4$@FeNi LDH/Ni foil. **Figure S34a** shows that Ni 2p high resolution spectra of $NiCo_2O_4$@FeNi LDH with fitting peaks centered at 854.3 and 872.0 eV are ascribed to Ni^{2+} binding

energy and peaks located at 856.3 and 874.0 eV are attributed to Ni^{3+}. In addition, two satellite peaks at 861.3 and 879.5 eV are observed. Similarly, Ni 2p spectrum of NiFe LDH, NiCo LDH and $NiCo_2O_4$ deconvoluted of Ni $2p_{3/2}$, Ni $2p_{1/2}$ and two satellite peaks. The Co 2p spectra of NiFe LDH, NiCo LDH, $NiCo_2O_4$, and $NiCo_2O_4$@FeNi LDH were deconvoluted with Co^{3+}, Co^{2+}, and satellite peaks in **Figure S34c**. Co $2p_{3/2}$ and Co $2p_{1/2}$ of $NiCo_2O_4$@FeNi LDH are decomposed into Co^{2+} (781.2 and 796.8 eV) as well as Co^{3+} (779.4 and 794.6 eV), respectively. As shown in **Figure 34d**, O 1s spectra were deconvoluted into peaks of metal–oxygen bonds (~532.5 eV), oxygen in the hydroxide group (~531 eV) and chemisorbed water molecules (~530 eV).

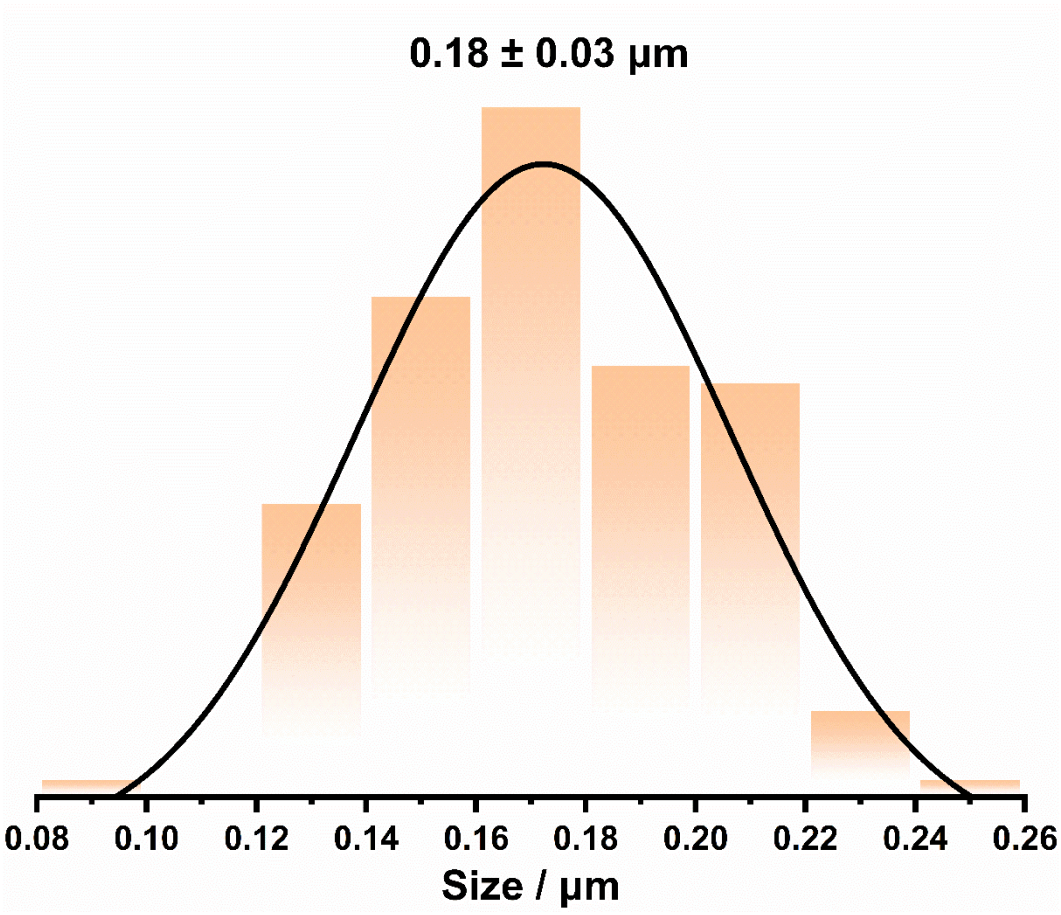

Fig. S35 | Ionomer diameter distrubution. The QAPPT ionomer diameter distribution in 3D-ordered anode CLs based on $NiCo_2O_4$@FeNi LDH nanowire arrays.

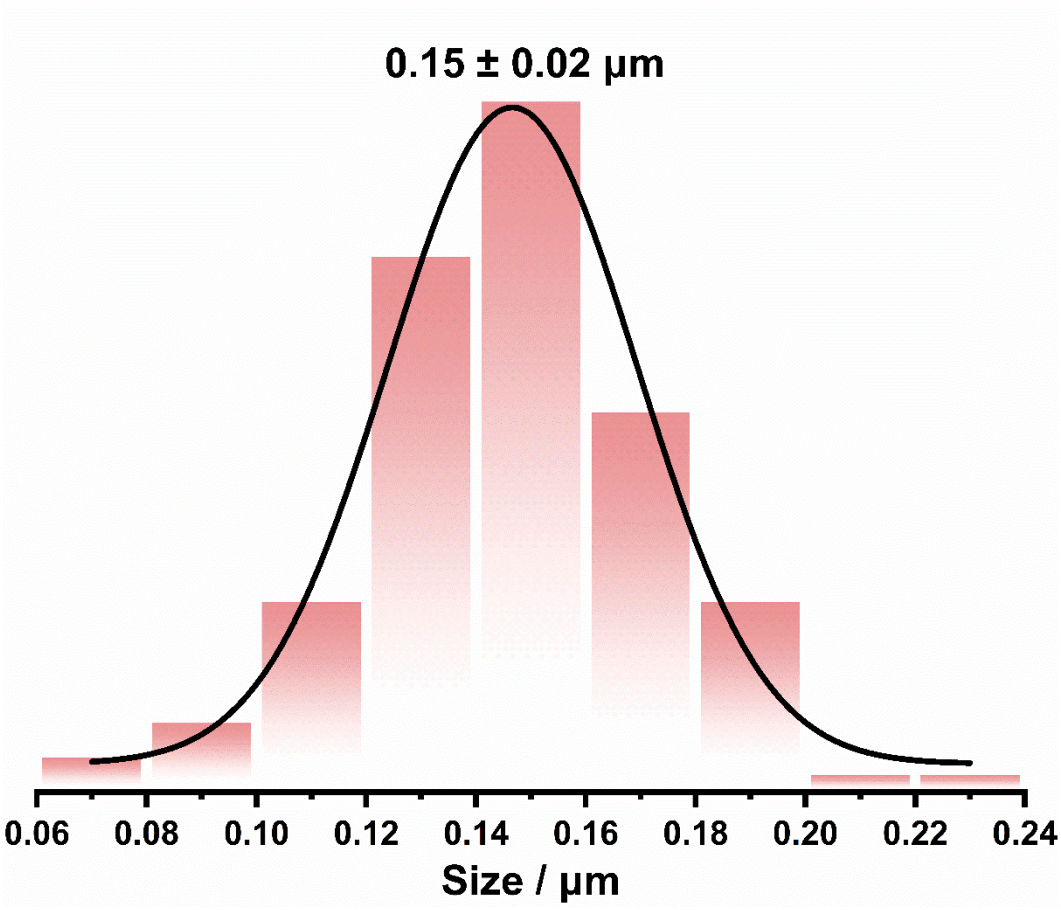

Fig. S36 | Ionomer diameter distrubution. The QAPPT ionomer diameter distribution in 3D-ordered anode CLs based on NiCo@FeNi LDH porous foams.

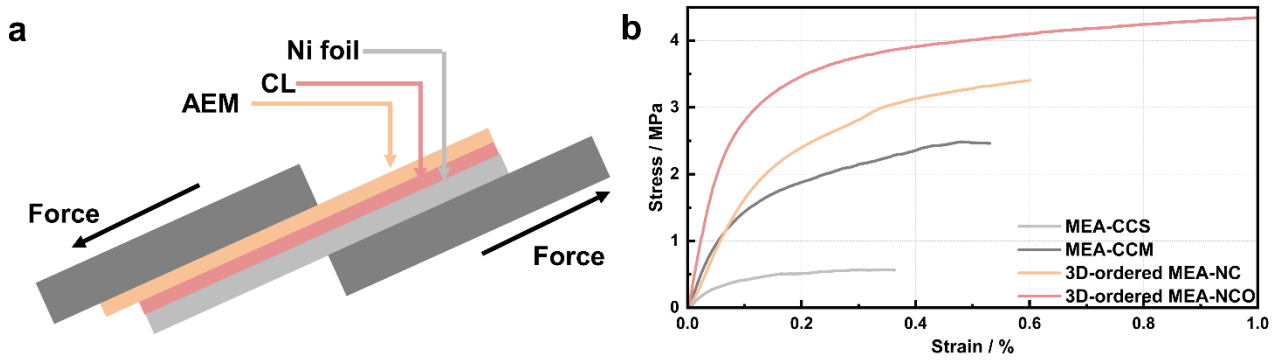

Fig. S37 | Interfacial bonding strength for 3D-ordered anode CLs in MEA. **a**, Structural illustration of evaluation method of interfacial bonding strength. **b**, Tensile stress–strain curves for shear testing of conventional MEA-CCS, MEA-CCM, 3D-ordered MEA-NC@FN and 3D-ordered MEA-NCO@FN.

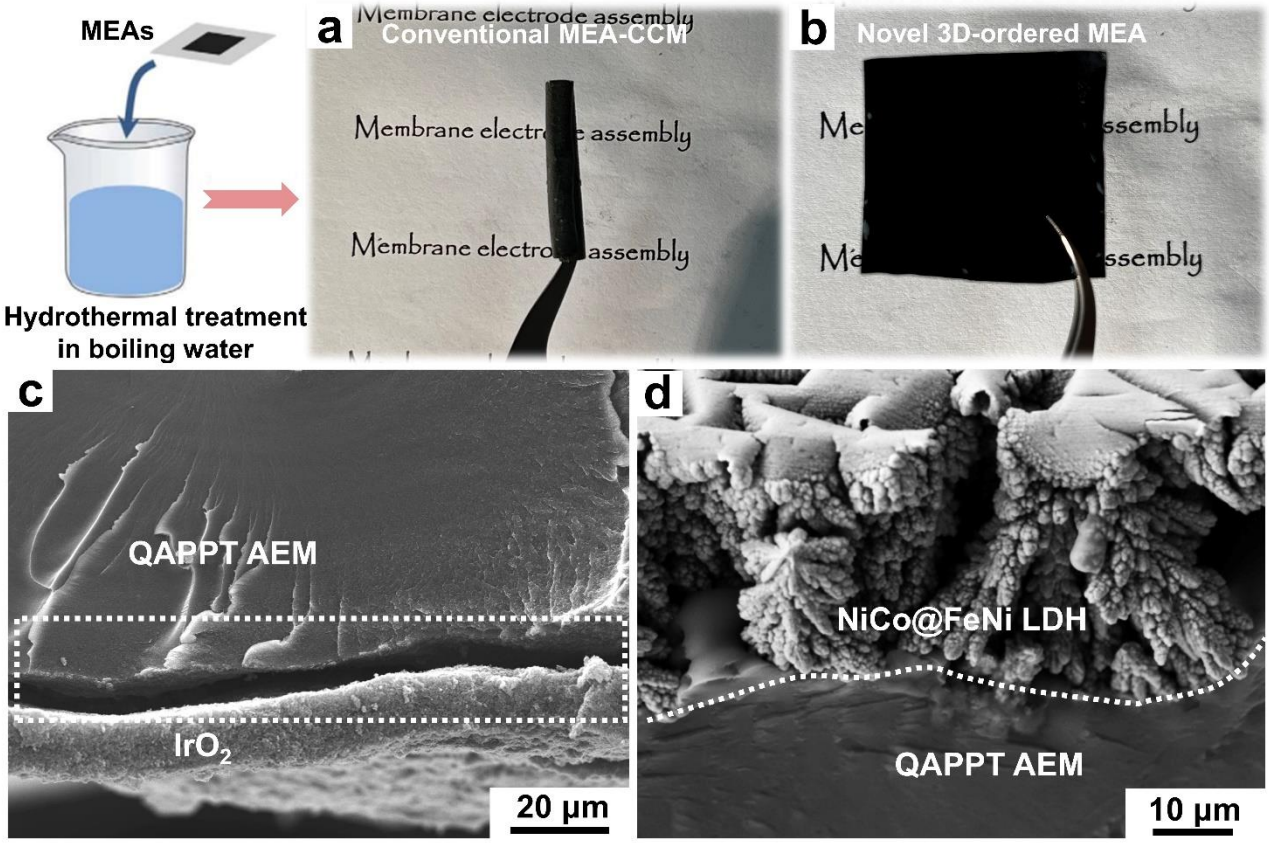

Fig. S38 | Hydrothermal adhesion test of MEAs in boiling water. Digital images of (a) conventional MEA-CCM and (b) novel 3D-ordered MEA after the hydrothermal adhesion tests. The cross-sectional SEM images of (c) conventional MEA-CCM and (d) novel 3D-ordered MEA after hydrothermal adhesion test.

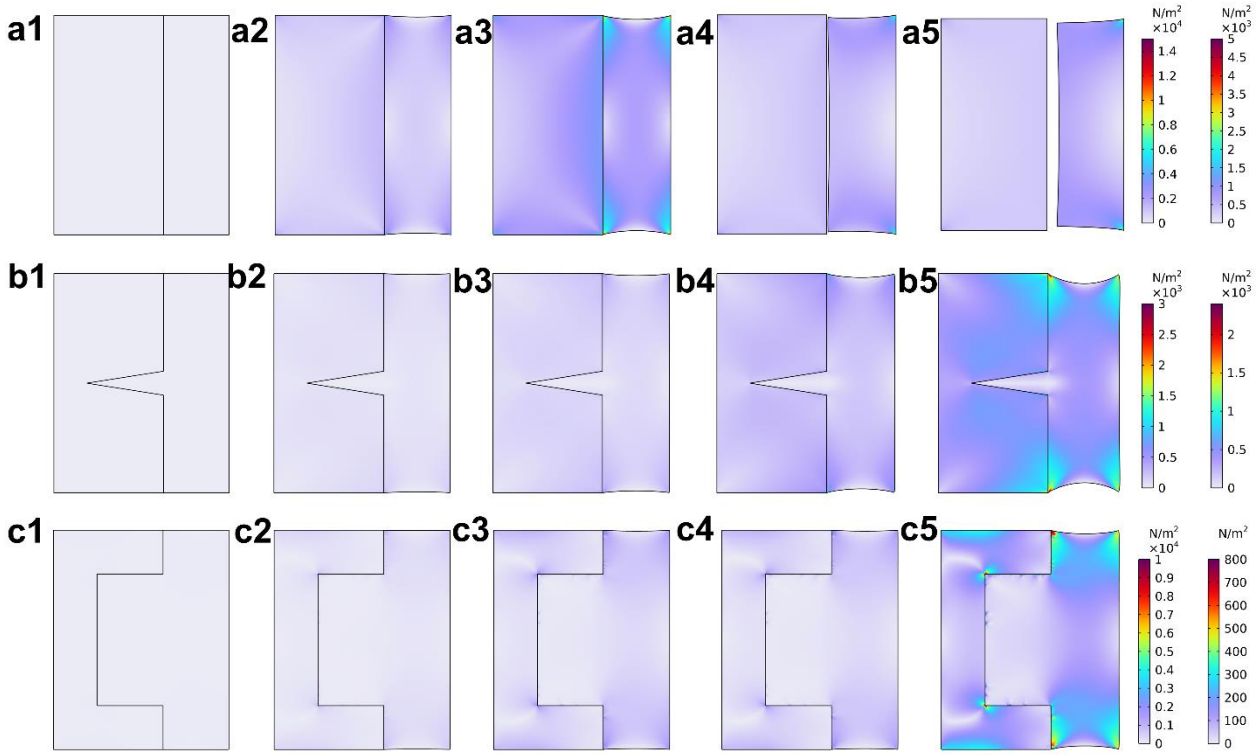

Fig. S39 | Interfacial bonding strength for 3D-ordered anode CLs in MEA. COMSOL Multiphysics simulations for AEM/anode CL interfaces of (a) conventional MEA-CCM, (b) 3D-ordered MEA-NC@FN and (c) 3D-ordered MEA-NCO@FN.

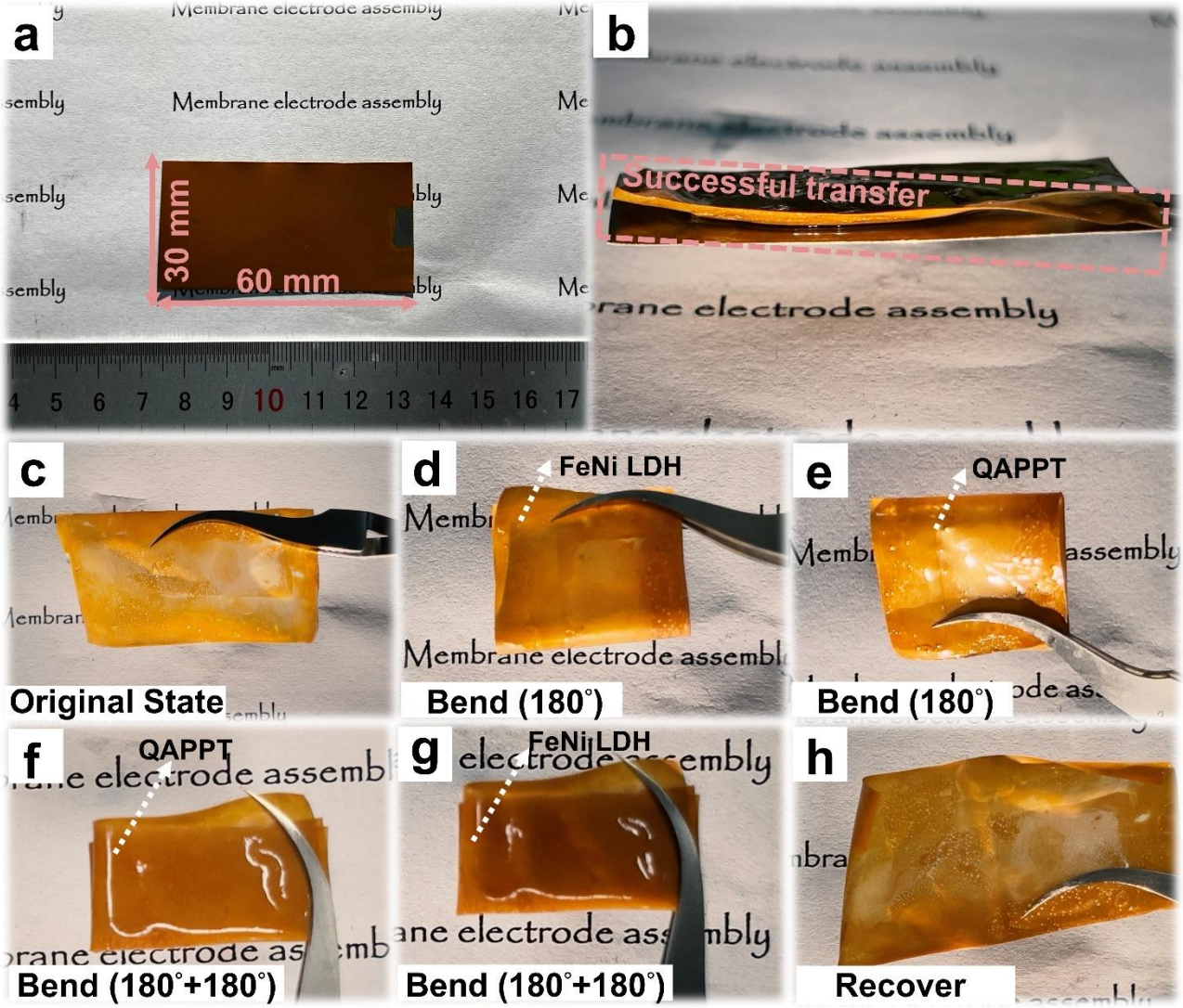

Fig. S40 | Scaled up and large-area 3D-ordered MEAs and mechanical bend test. Digital images of (a-b) 3D-ordered MEA (30 mm × 60 mm; 18 cm^2) using FeNi LDH as the anode. Digital images of (c-h) mechanical toughness test. The 3D-ordered MEA recovered their shape without cracks even after the bend tests.

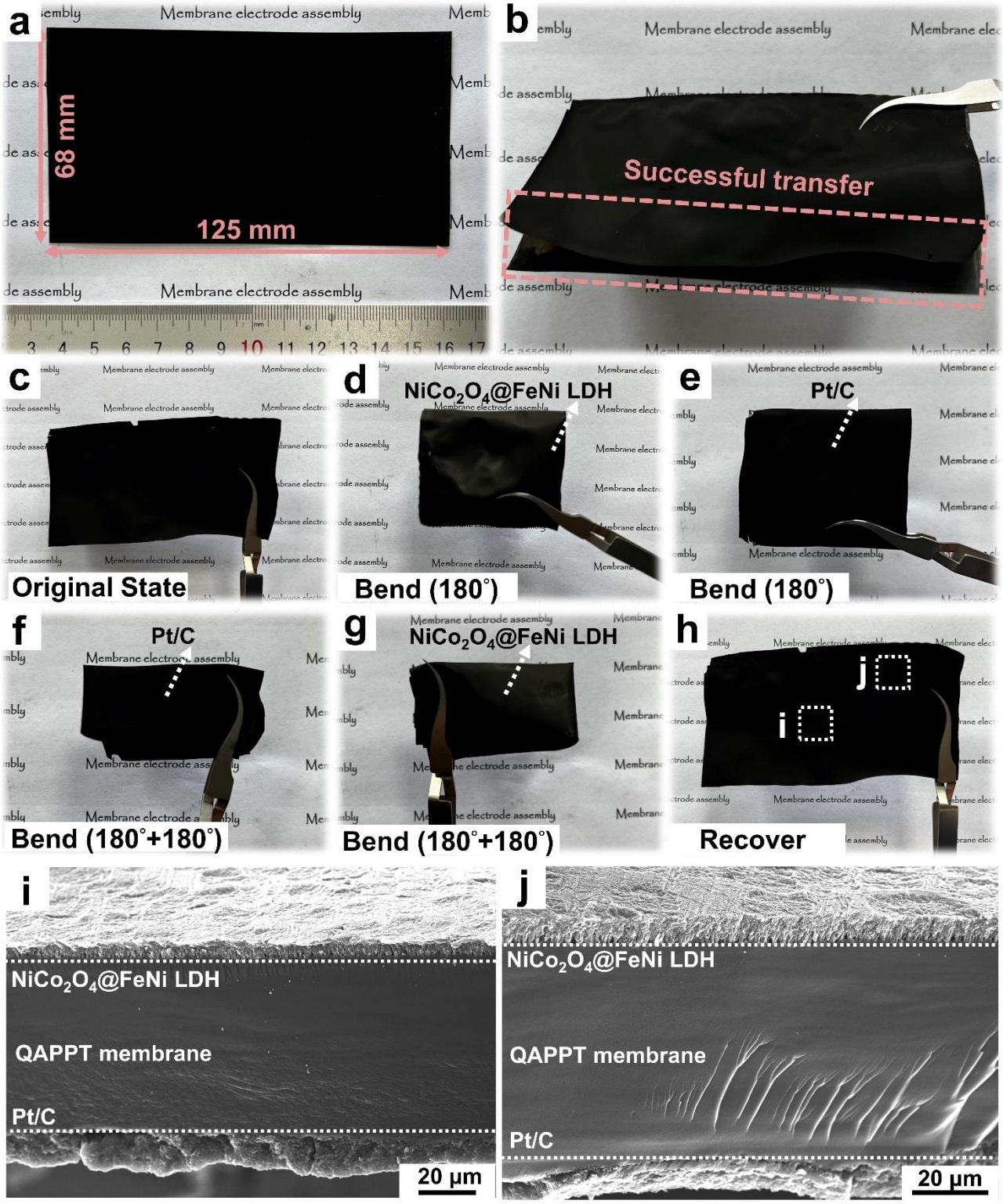

Fig. S41 | Scaled up and large-area 3D-ordered MEAs and mechanical bend test. Digital images of (a-b) 3D-ordered MEA (68 mm × 125 mm; 85 cm^2) using $NiCo_2O_4$@FeNi LDH as the anode. Digital images of (c-h) mechanical toughness test. The 3D-ordered MEA recovered their shape without cracks even after the bend tests. The cross-section morphologies of the representative areas (i) and (j) in the 3D-ordered MEA after the mechanical

bend test.

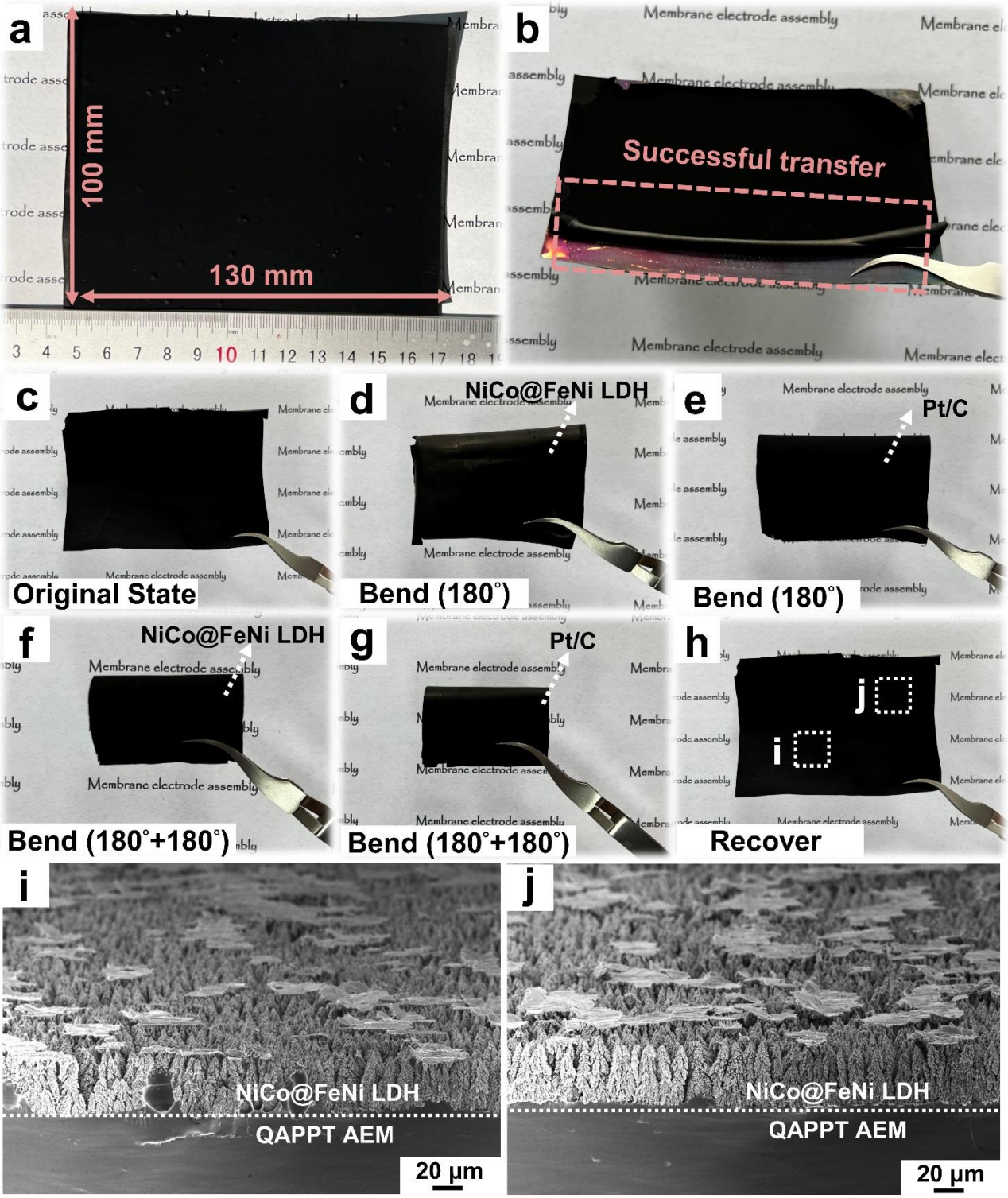

Fig. S42 | Scaled up and large-area 3D-ordered MEAs and mechanical bend test. Digital images of (a-b) 3D-ordered MEA (100 mm × 130 mm; 130 cm^2) using NiCo@FeNi LDH as the anode. Digital images of (c-h) mechanical toughness test. The 3D-ordered MEA recovered their shape without cracks even after the bend tests.

The cross-section morphologies of the representative areas (i) and (j) in the 3D-ordered MEA after the mechanical bend test.

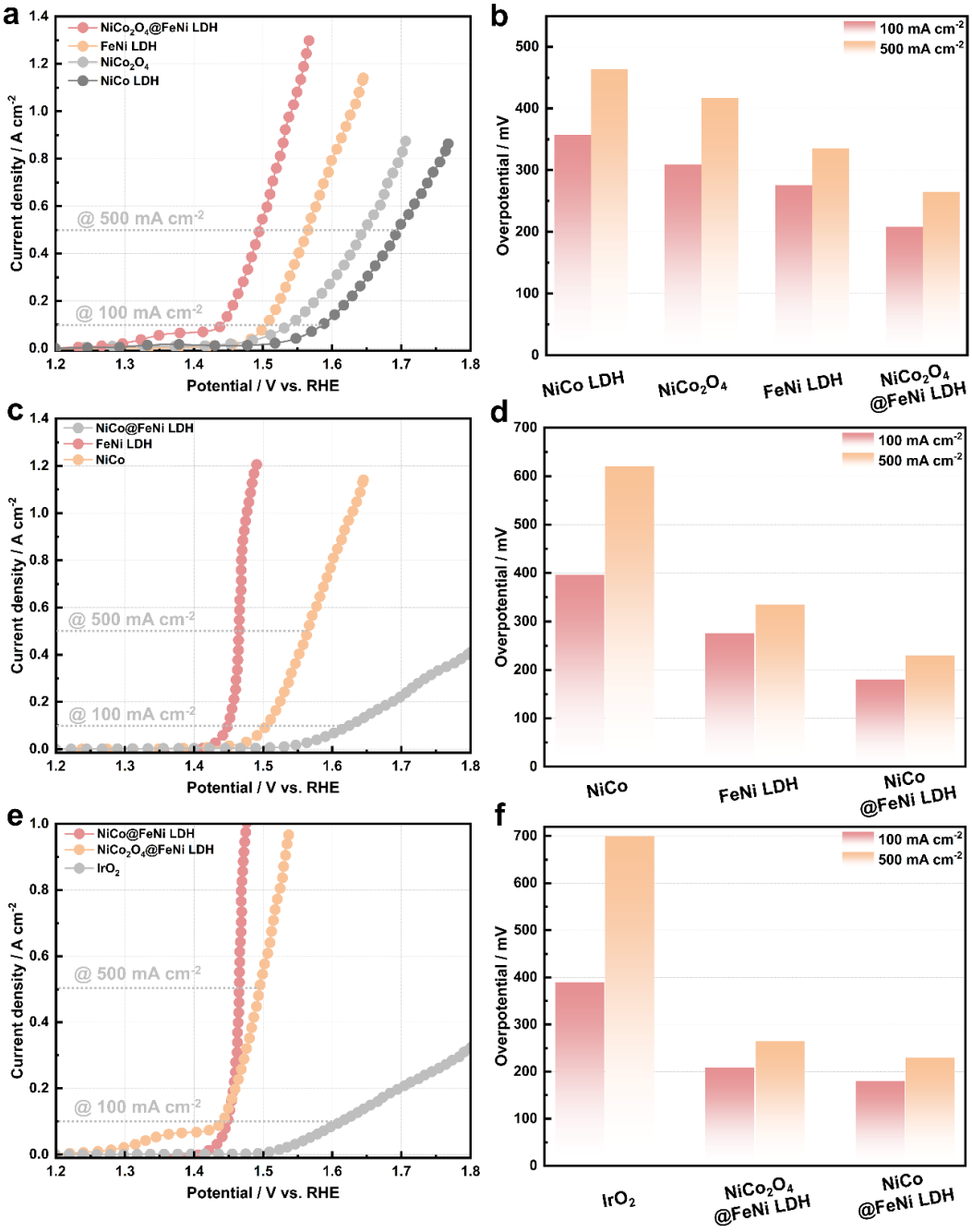

Fig. S43 | OER activity evaluation by a three-electrode system. Electrocatalytic properties of NiCo LDH, $NiCo_2O_4$, FeNi LDH, $NiCo_2O_4$@FeNi LDH, NiCo, NiCo@FeNi LDH and IrO_2: (a), (c) and (e) LSV plots obtained at 5 mV s^{-1} in 1 M KOH; (b), (d) and (f) Overpotential at different current densities (100 and 500 mA

cm^{-2}).

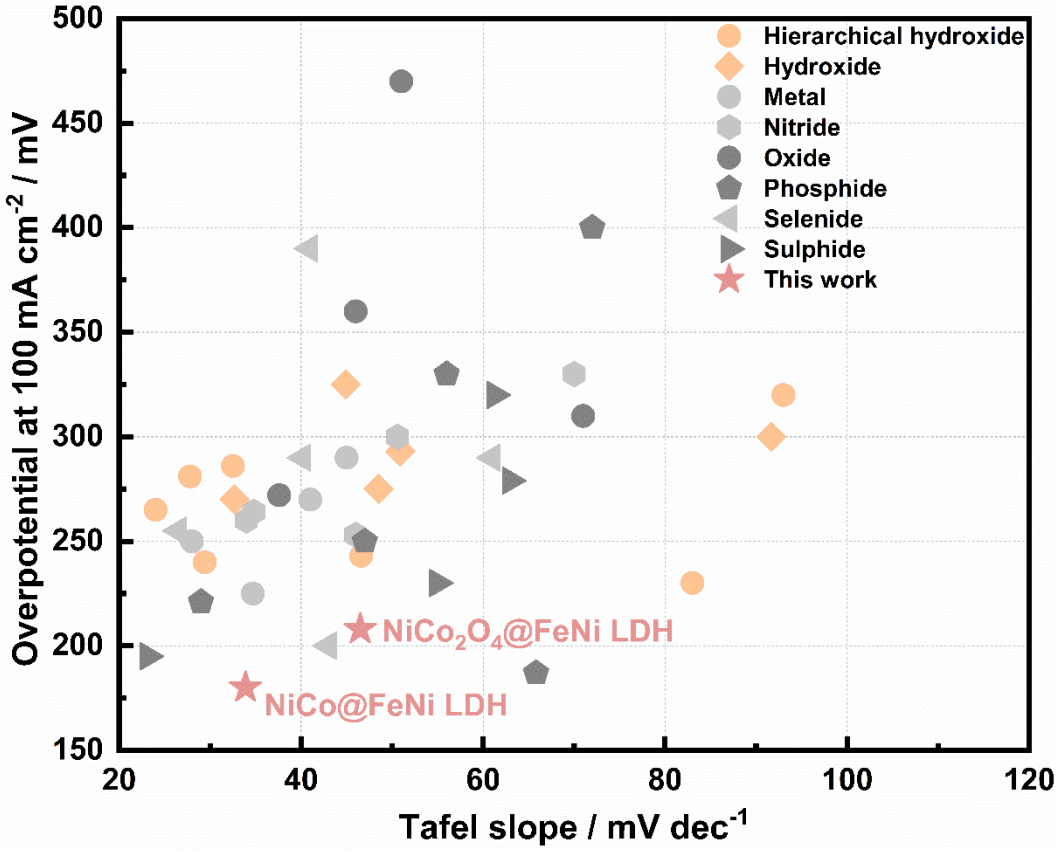

Fig. S44 | Comparison of the activities of different OER electrocatalysts. The details on the overpotential at 100 mA cm^{-2} and Tafel slope can be found in **Supplementary Table 2**.

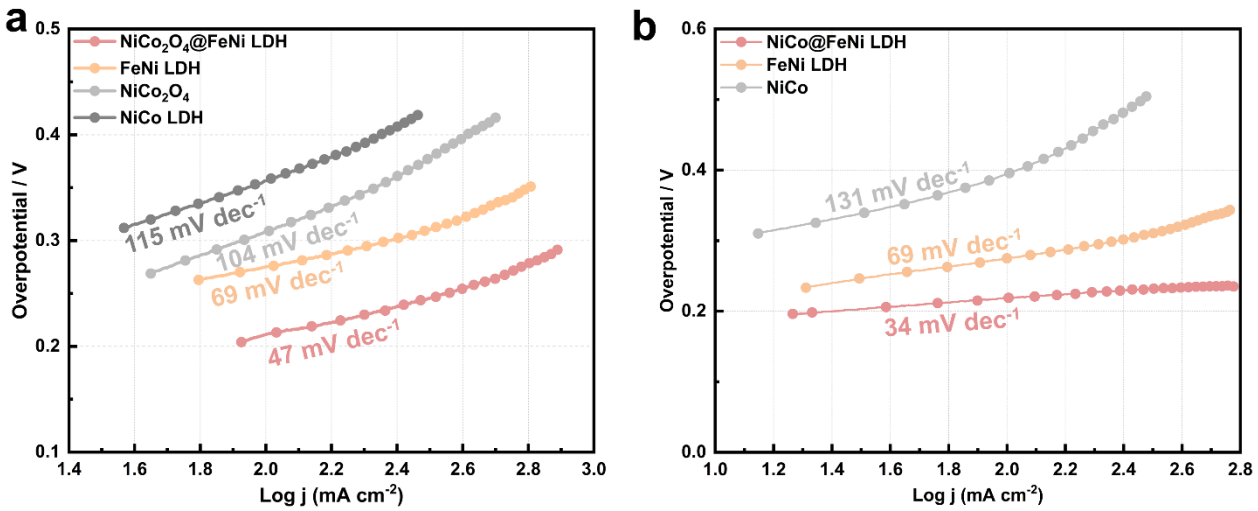

Fig. S45 | OER activity evaluation by a three-electrode system. (a-b) Tafel plots obtained for NiCo LDH, $NiCo_2O_4$, FeNi LDH, $NiCo_2O_4$@FeNi LDH, NiCo and NiCo@FeNi LDH in 1 M KOH.

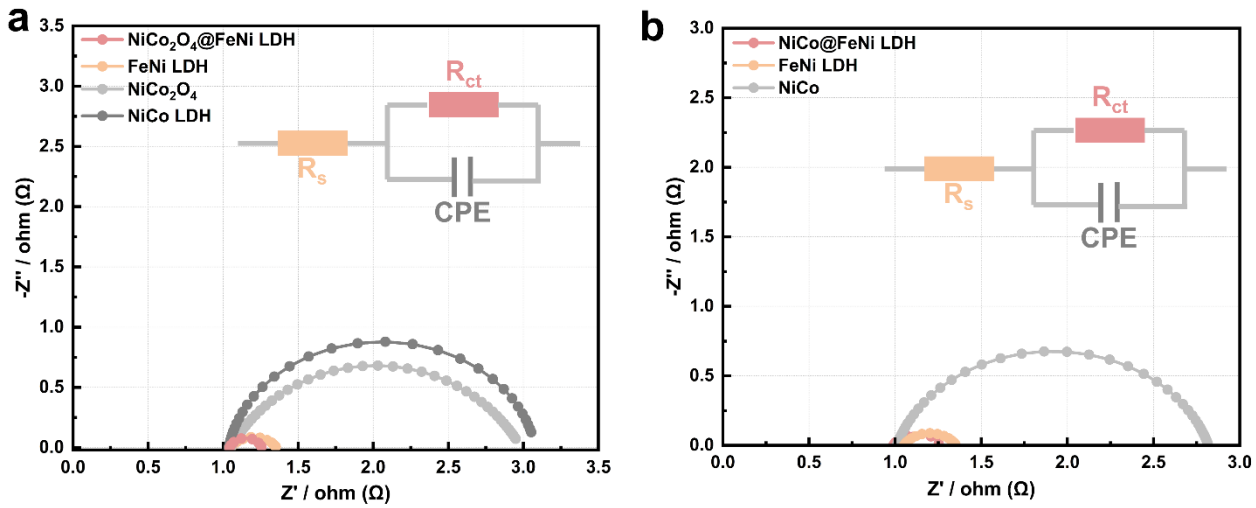

Fig. S46 | OER activity evaluation by a three-electrode system. (a-b) Nyquist plots of CoNi LDH, $NiCo_2O_4$, FeNi LDH, $NiCo_2O_4$@FeNi LDH, NiCo and NiCo@FeNi LDH obtained at the potential of 1.527 V vs RHE.

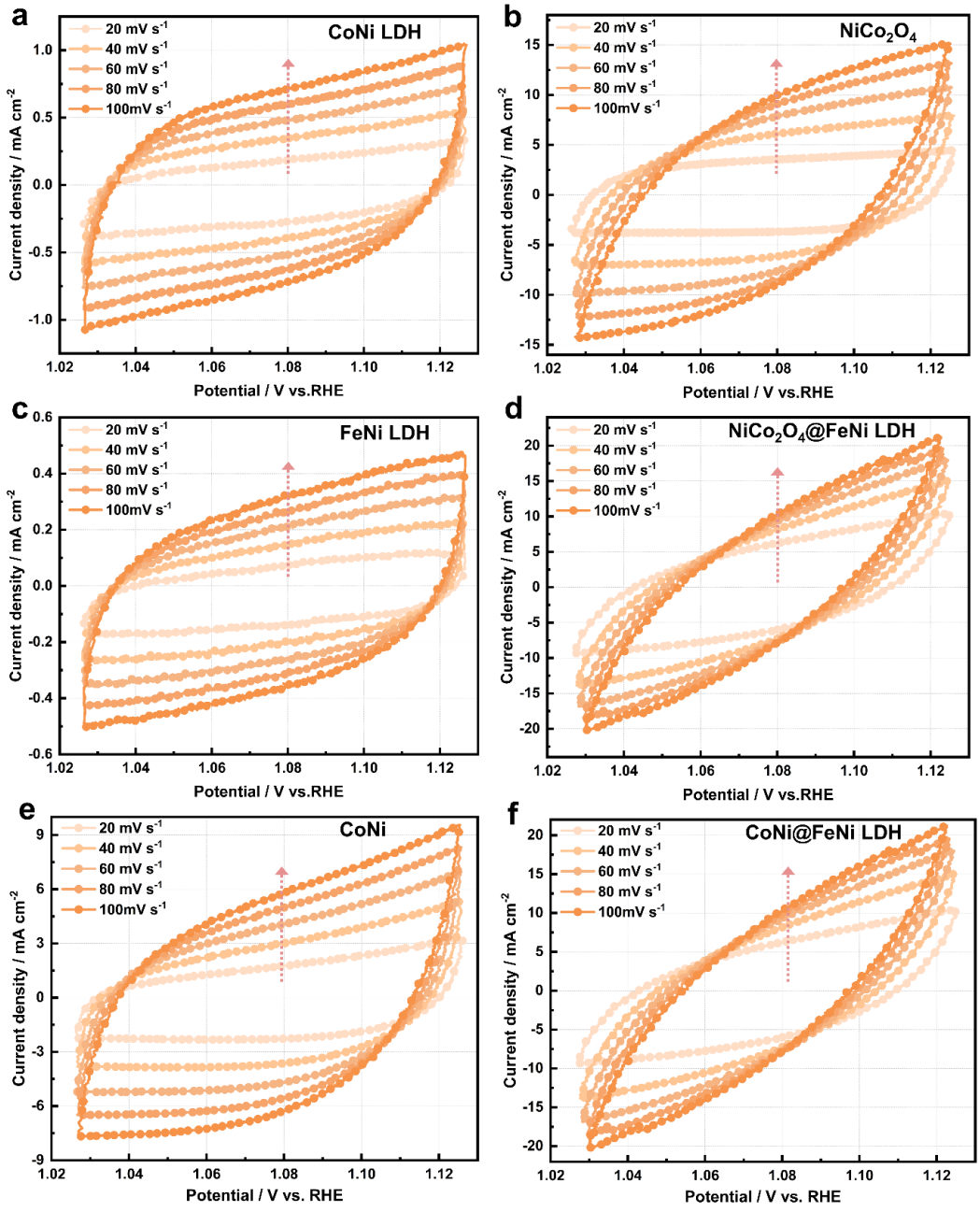

Fig. S47 | OER activity evaluation by a three-electrode system. CV curves at different scan rates within the non-faradaic potential regions with the scan interval of 20 mV s^{-1} for (a) CoNi LDH, (b) $NiCo_2O_4$, (c) FeNi LDH, (d) $NiCo_2O_4$@FeNi LDH, (e) CoNi and (f) CoNi@FeNi LDH.

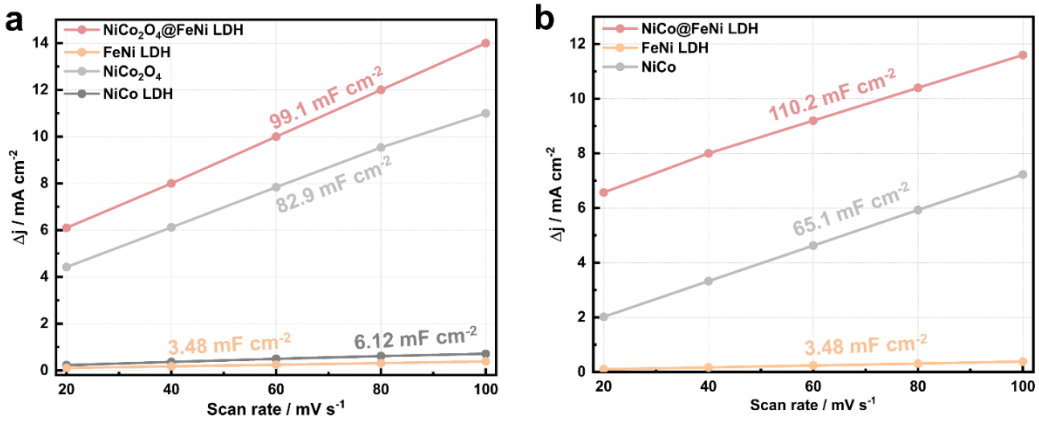

Fig. S48 | OER activity evaluation by a three-electrode system. (a-b) Capacitive currents as a function of scan rate for ECSA.

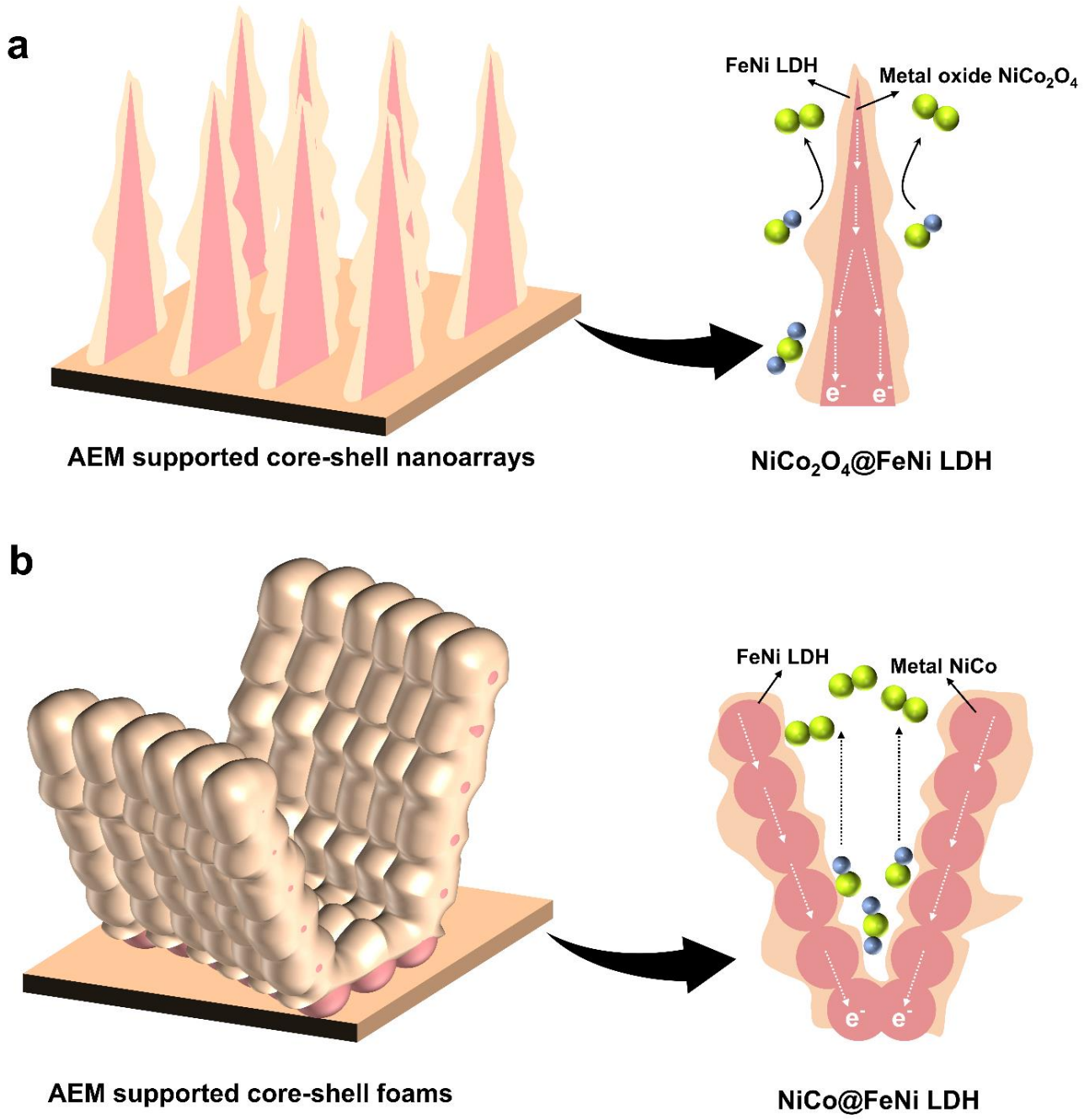

Fig. S49 | Illustration of the OER behavior for (a) $NiCo_2O_4$@FeNi LDH and (b) NiCo@FeNi LDH.

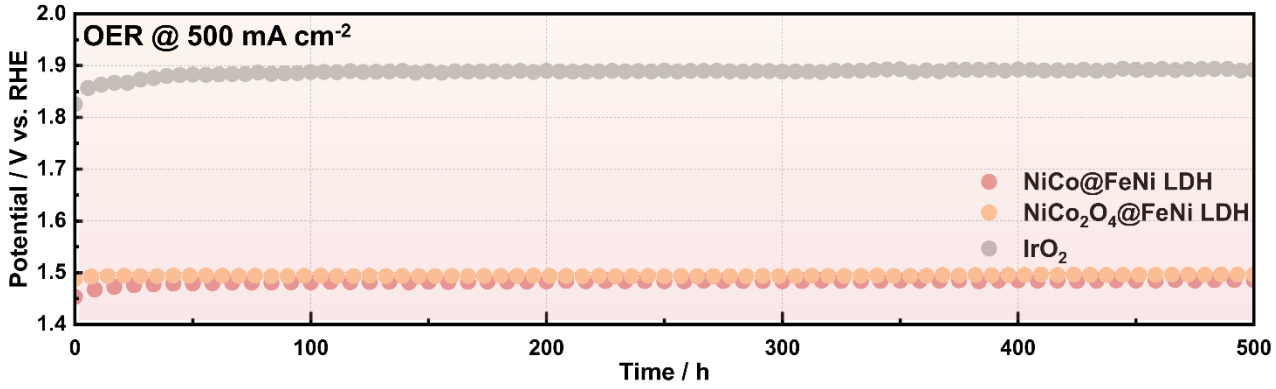

Fig. S50 | OER stability evaluation by a three-electrode system. Chronopotentiometry response of IrO_2, $NiCo_2O_4$@FeNi LDH and NiCo@FeNi LDH at 500 mA cm^{-2} in 1 M KOH.

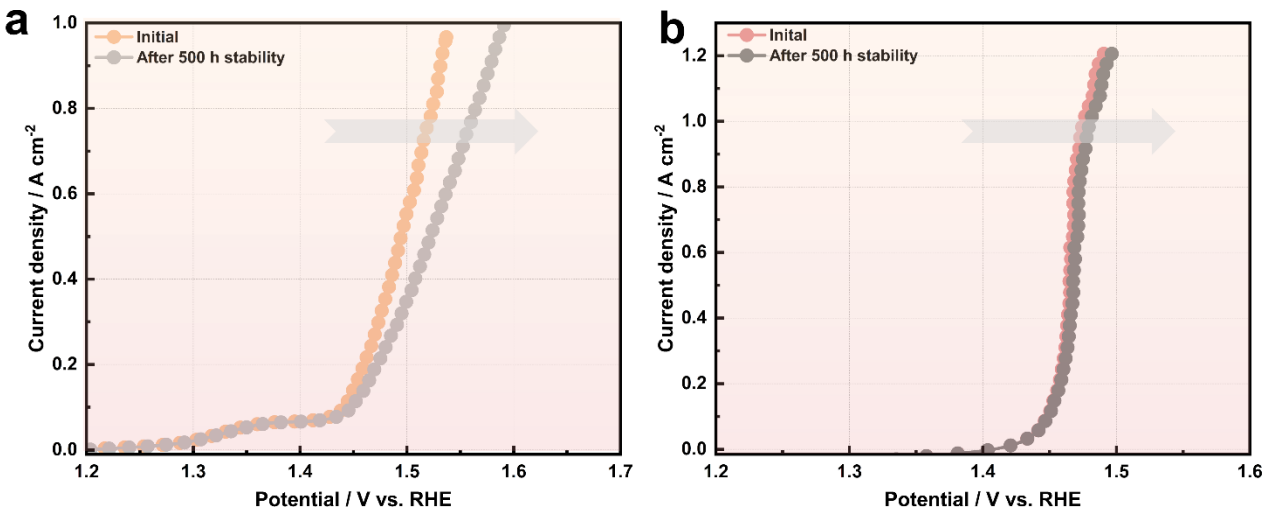

Fig. S51 | OER stability evaluation by a three-electrode system. The comparison of polarization curves of initial test and after 500 h stability for (a) $NiCo_2O_4$@FeNi LDH and (b) NiCo@FeNi LDH.

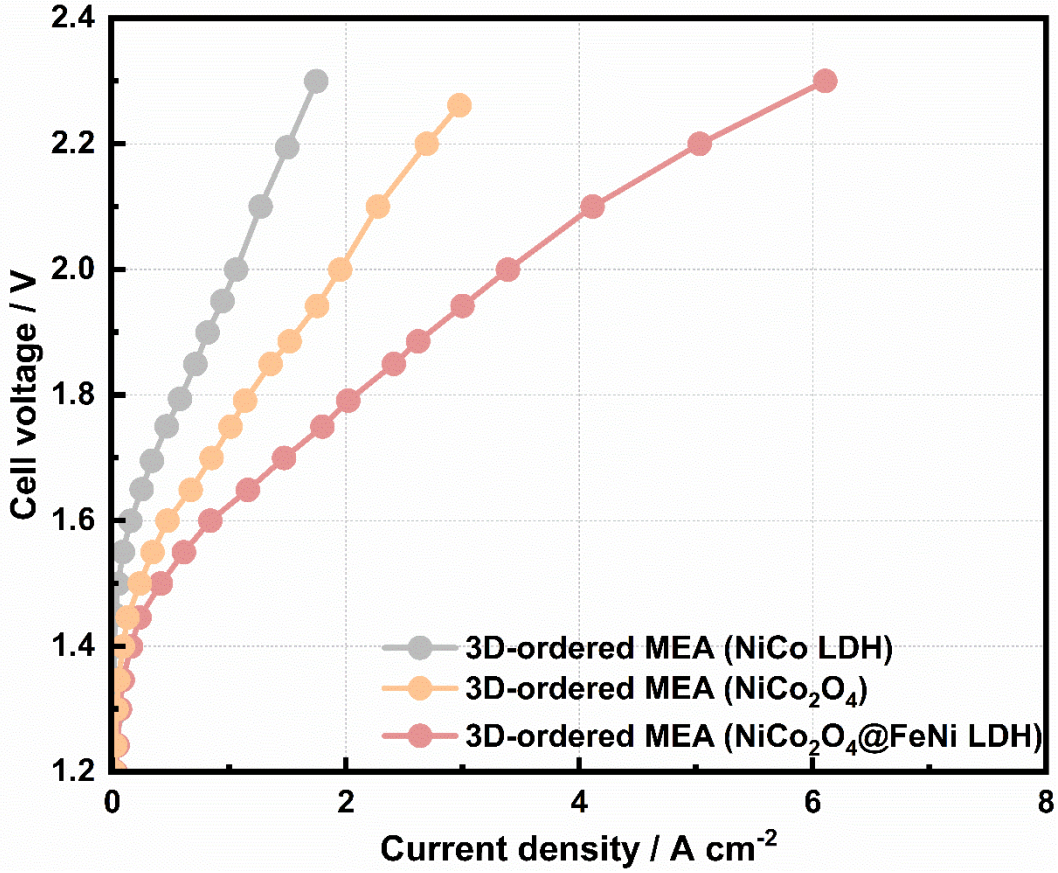

Fig. S52 | Performance evaluation of 3D-ordered MEAs using different anode CLs. Single-cell performance of 3D-ordered MEAs based on different anode CLs (NiCo LDH, $NiCo_2O_4$ and $NiCo_2O_4$@FeNi LDH) in 1 M KOH at 60 °C

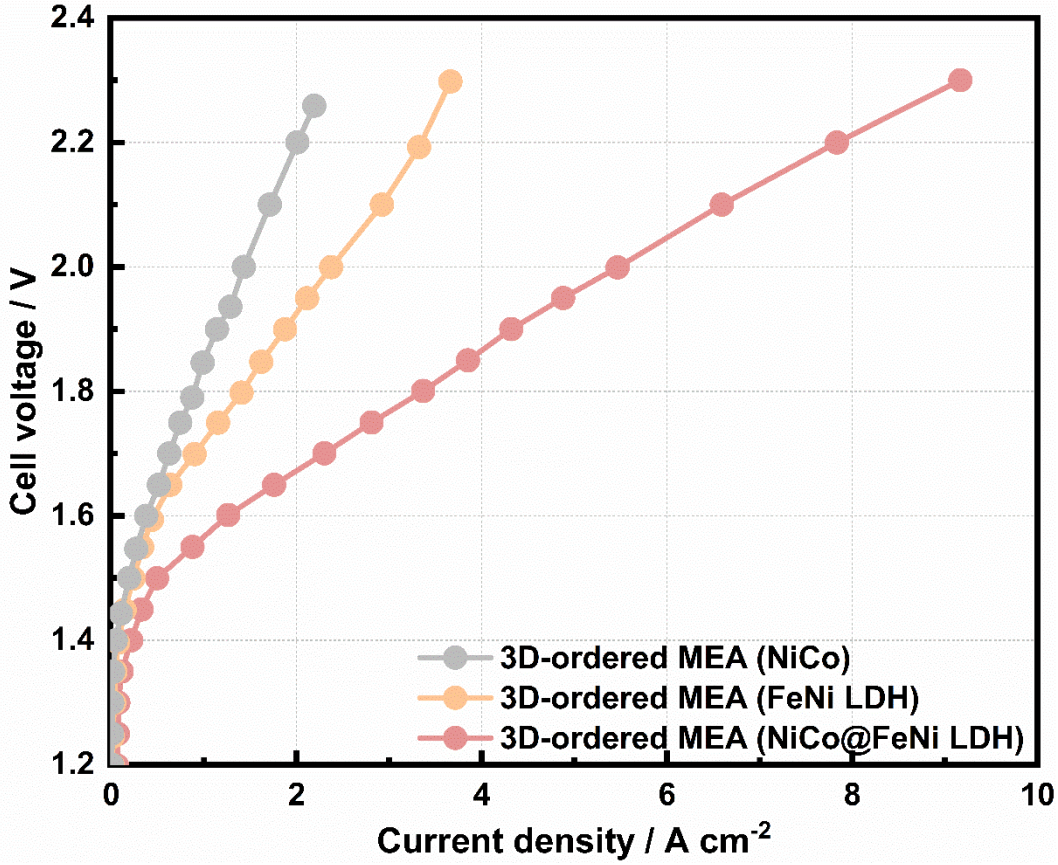

Fig. S53 | Performance evaluation of 3D-ordered MEAs using different anode CLs. Single-cell performance of 3D-ordered MEAs based on different anode CLs (NiCo, FeNi LDH, and NiCo@FeNi LDH) in 1 M KOH at 60 °C

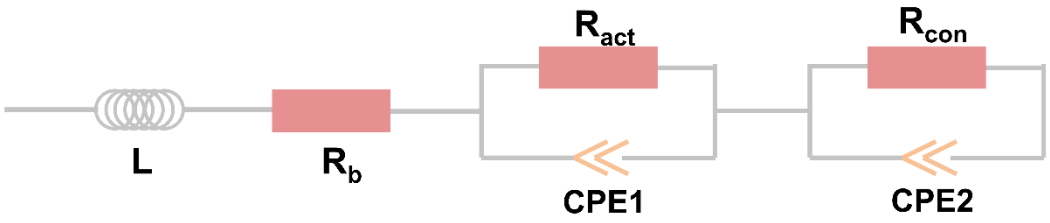

Fig. S54 | Equivalent circuit model for AEM water electrolysis cells. The equivalent circuit consists of an ohmic resistance (R_b) in series with two circuits, each comprising a resistance (R_{act}, activation resistance, and R_{con}, concentration resistance) and a CPE in parallel (CPE1 and CPE2, respectively). The inductor (L) in series with the R_b represents possible inductive parts of cables and other components.

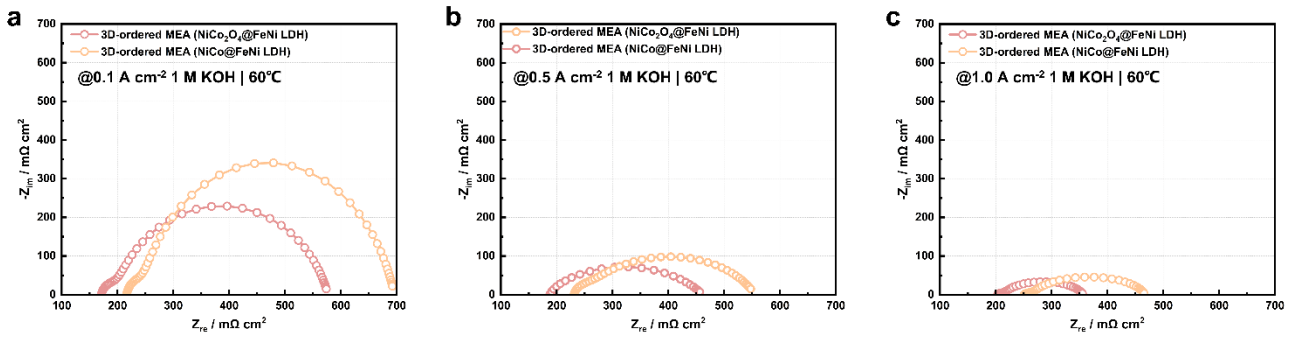

Fig. S55 | Nyquist plots from the EIS measurements for different 3D-ordered MEAs. Nyquist plot of 3D-ordered MEAs with $NiCo_2O_4$@FeNi LDH and NiCo@FeNi LDH at (a) 0.1 A cm^{-2}, (b) 0.5 A cm^{-2}, and (c) 1.0 A cm^{-2} in 1 M KOH at 60℃. The frequency range was 10 kHz to 0.1 Hz, and the amplitude was 50 mV.

a

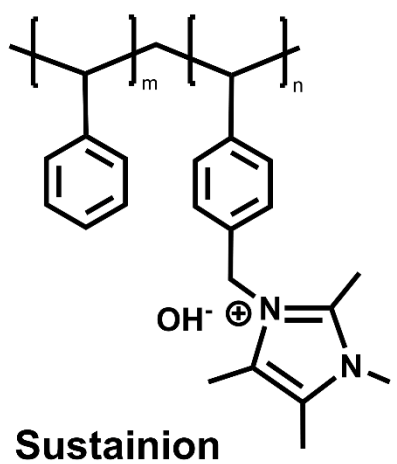

Sustainion

b

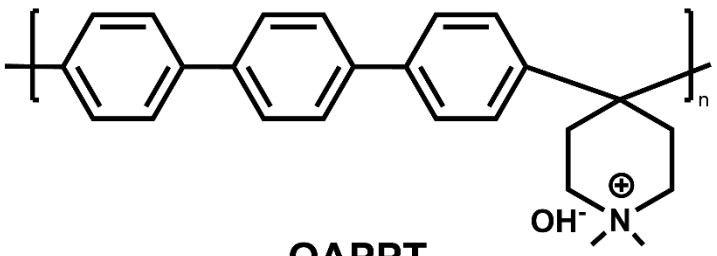

QAPPT

c

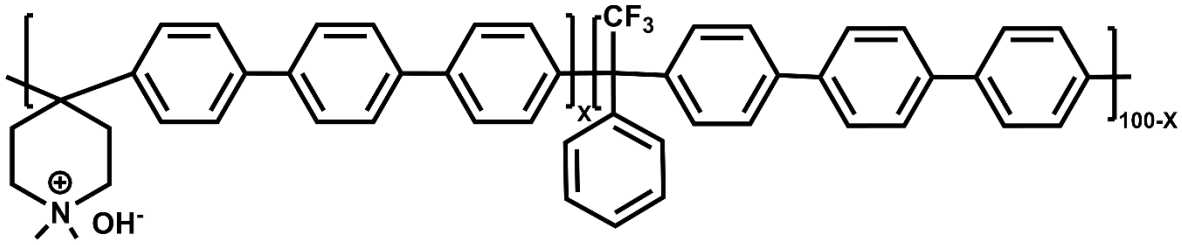

PiperION

d

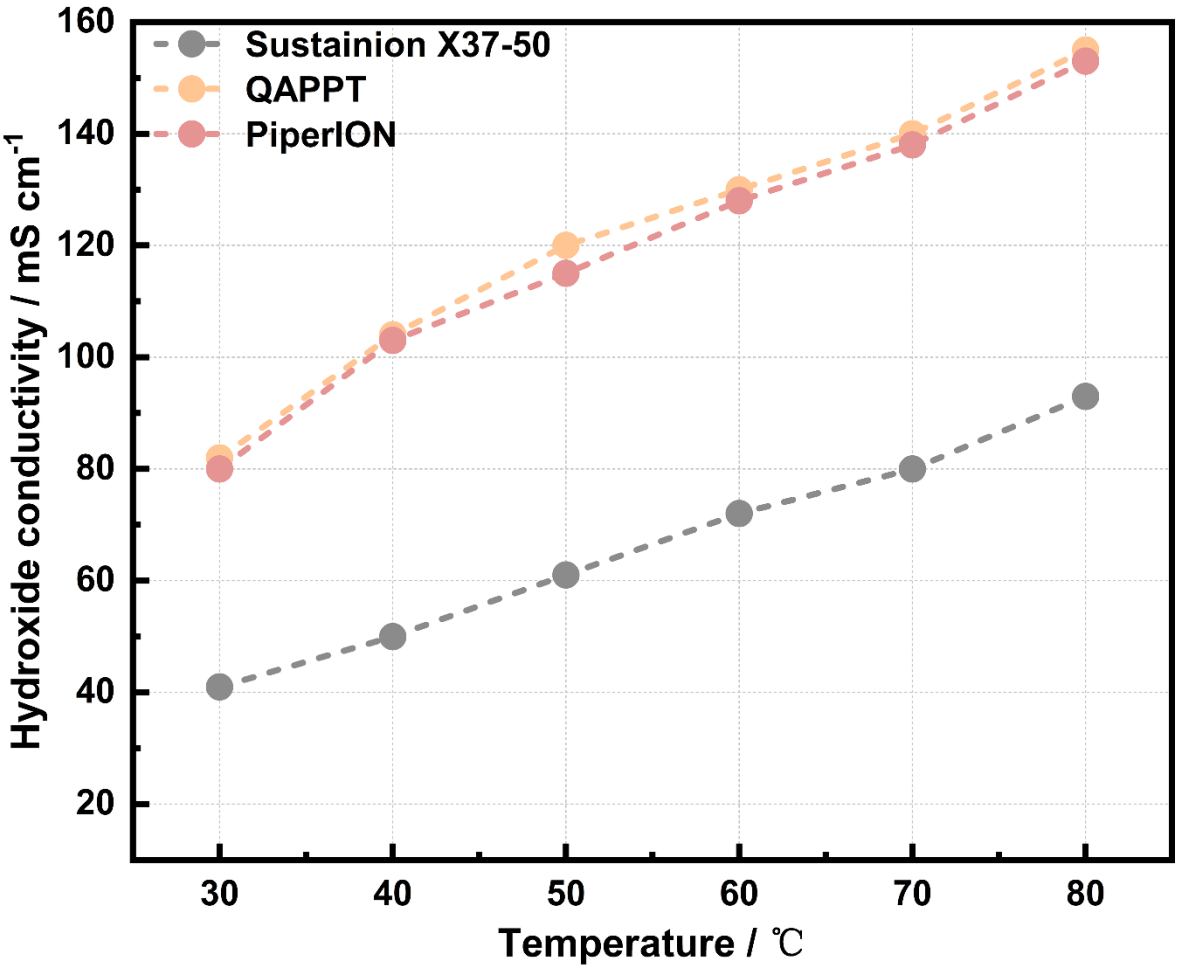

Fig. S56 | Hydroxide ion conductivity of AEMs. The chemical structures (a) Sustainion X37-50, (b) QAPPT, and (c) PiperION. (d) Hydroxide ion (OH^-) conductivities of different AEMs as a function of temperature.

Supplementary Note 4

Before hydroxide conductivity measurement of AEMs, the self-supported AEMs were prepared by catsing corresponding ionomer in a horizontal glass plate. The corresponding AEM was obtained by drying it at 70 °C for 24 h. The obtained AEM samples of 1 cm × 4 cm were cut out and immersed in Ar-purged CO_2-free NaOH solution (1.0 M) in a shaker at 80 ℃ for 24 h. After thorough ion-exchange into the OH^- form, the samples were washed at least three times with CO_2-free DI water to remove excess OH^-. The hydroxide conductivity of each sample was measured by impedance spectroscopy with the standard four-point prode technique using a PARSTAT PMC2000A and a Teflon four platinic electrode cell. The cell membrane assembly was submersed in a CO_2-free DI water bath on a temperature-controlled heat stage. Temperature from 30 ℃ to 80 ℃ with a step value of 10 ℃ was set and 30 min was kept for each temperature and then high frequency impedance was collected. The measurement was conducted in a galvanostatic mode with frequency from 100 kHz to 100 Hz. The hydroxide conductivity was obtained by using the following relationship:

$$\sigma = L/ (R \times T \times W)$$

where L represents the distance between the sensing electrodes, which is 1 cm for the used cell, and R represents the ohmic resistance, and T and W are the thickness and width of samples. All dimensional data were collected with samples under testing conditions.

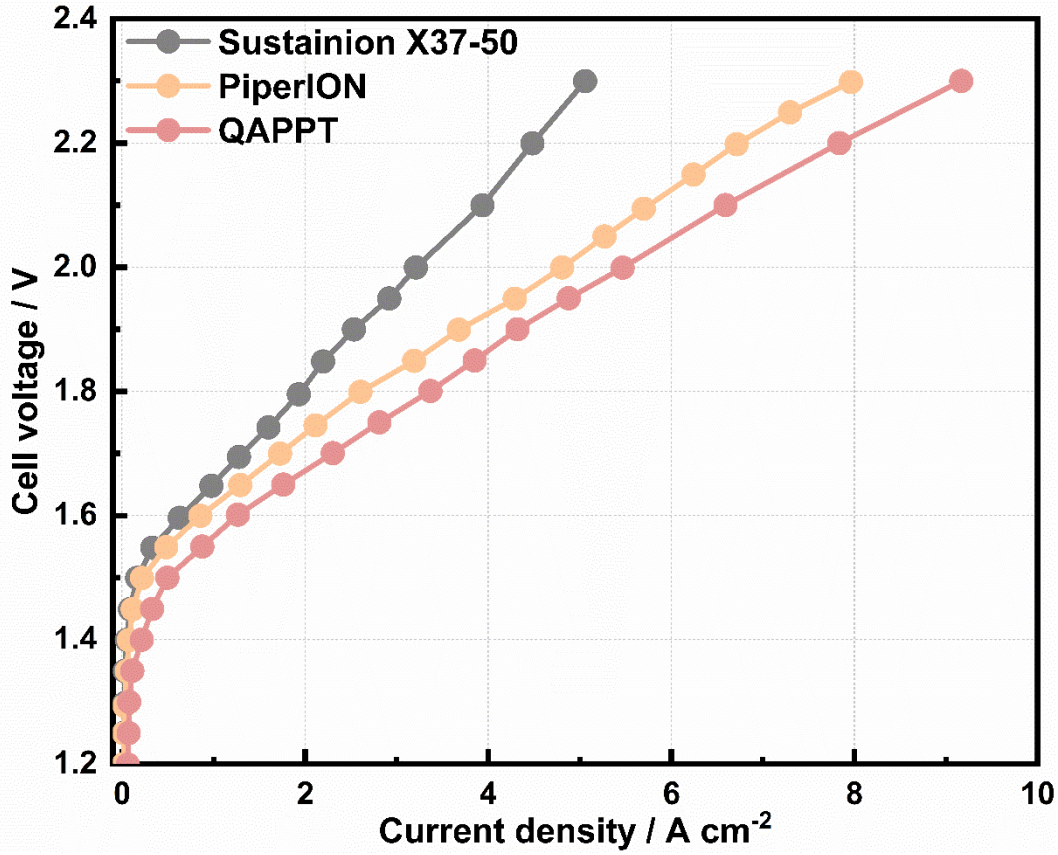

Fig. S57 | Electrolysis performance tests of novel 3D-ordered MEAs with different AEMs. Polarization curves of novel 3D-ordered MEAs using NiCo@FeNi LDH foams as ACL and different AEMs (including Sustainion X37-50, PiperION, and QAPPT). The electrolysis tests were performed in 1 M KOH at 60 ℃.

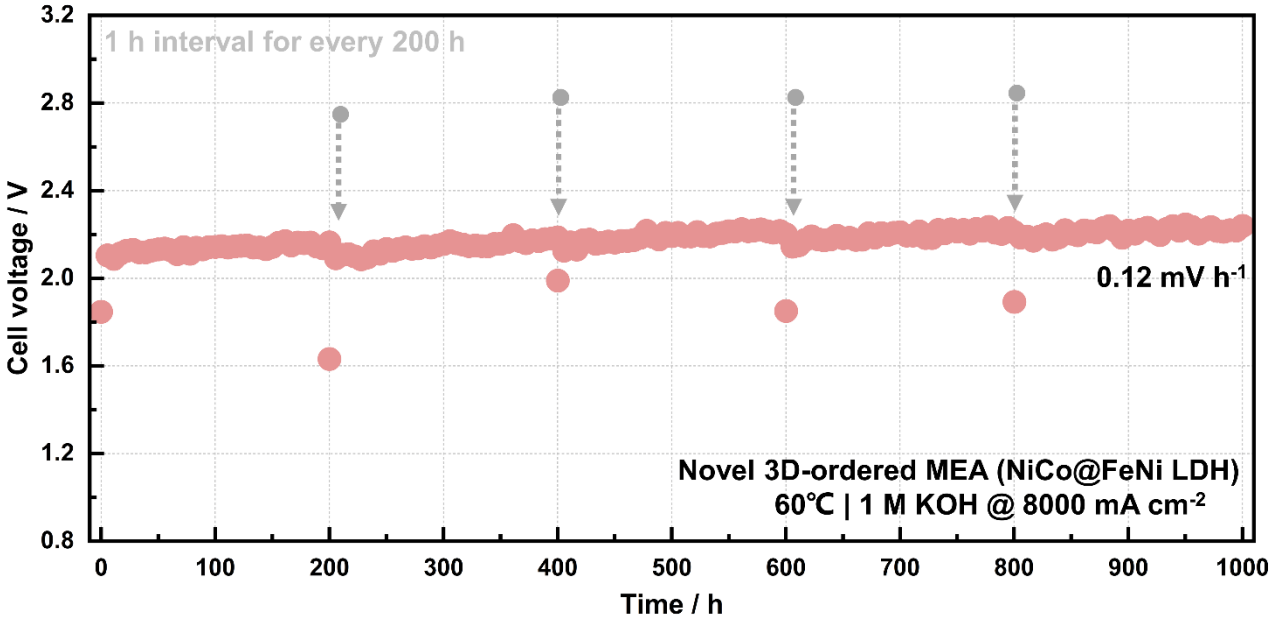

Fig. S58 | Electrolysis stability tests of novel 3D-ordered MEAs. Continuous durability tests of novel 3D-ordered MEAs using NiCo@FeNi LDH as ACLs at a current density of 8000 mA cm^{-2}. The stability tests were performed in 1 M KOH at 60 ℃. The electrolyzer runs for 1000 h with 1 h intervals for every 200 hour continuous operation.

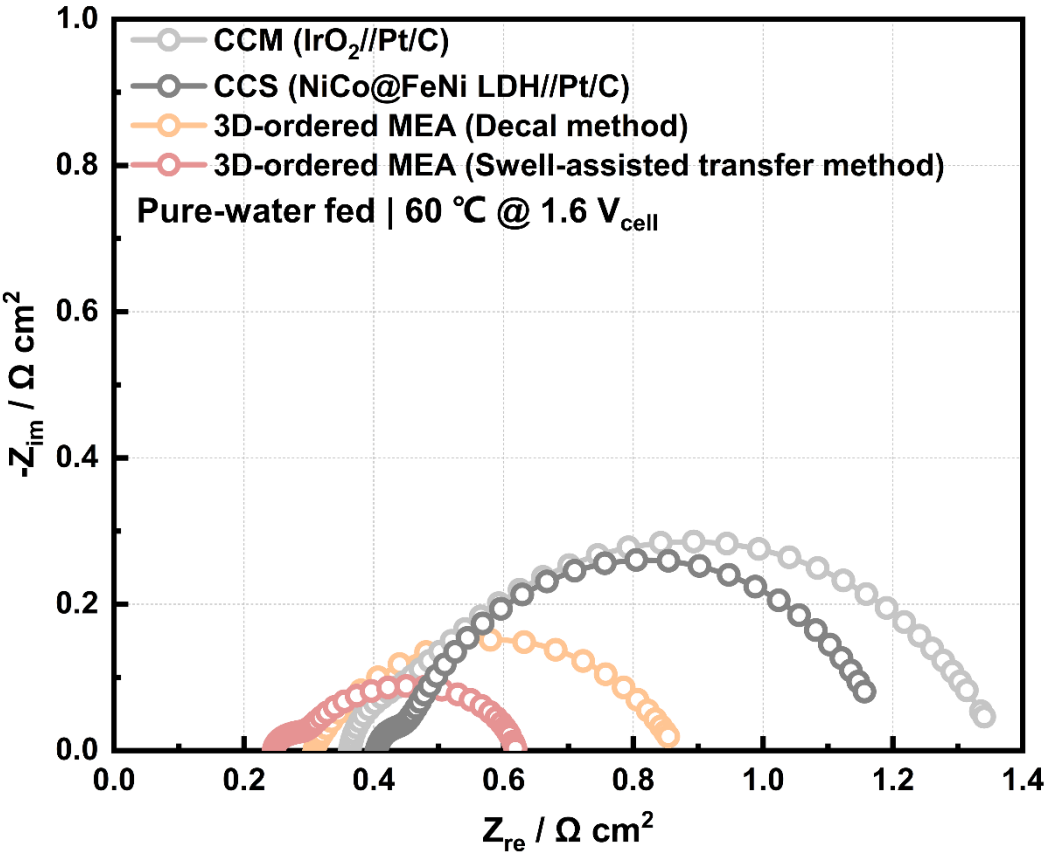

Fig. S59 | Nyquist plots from the EIS measurements for different MEAs prapared by different technique.

Nyquist plot of MEA-CCM (IrO_2//Pt/C), MEA-CCS (NiCo@FeNi LDH), 3D-ordered MEA (Decal method), and 3D-ordered MEA (Swell-assisted transfer method) at 1.6 V_{cell} in pure water at 60 °C.

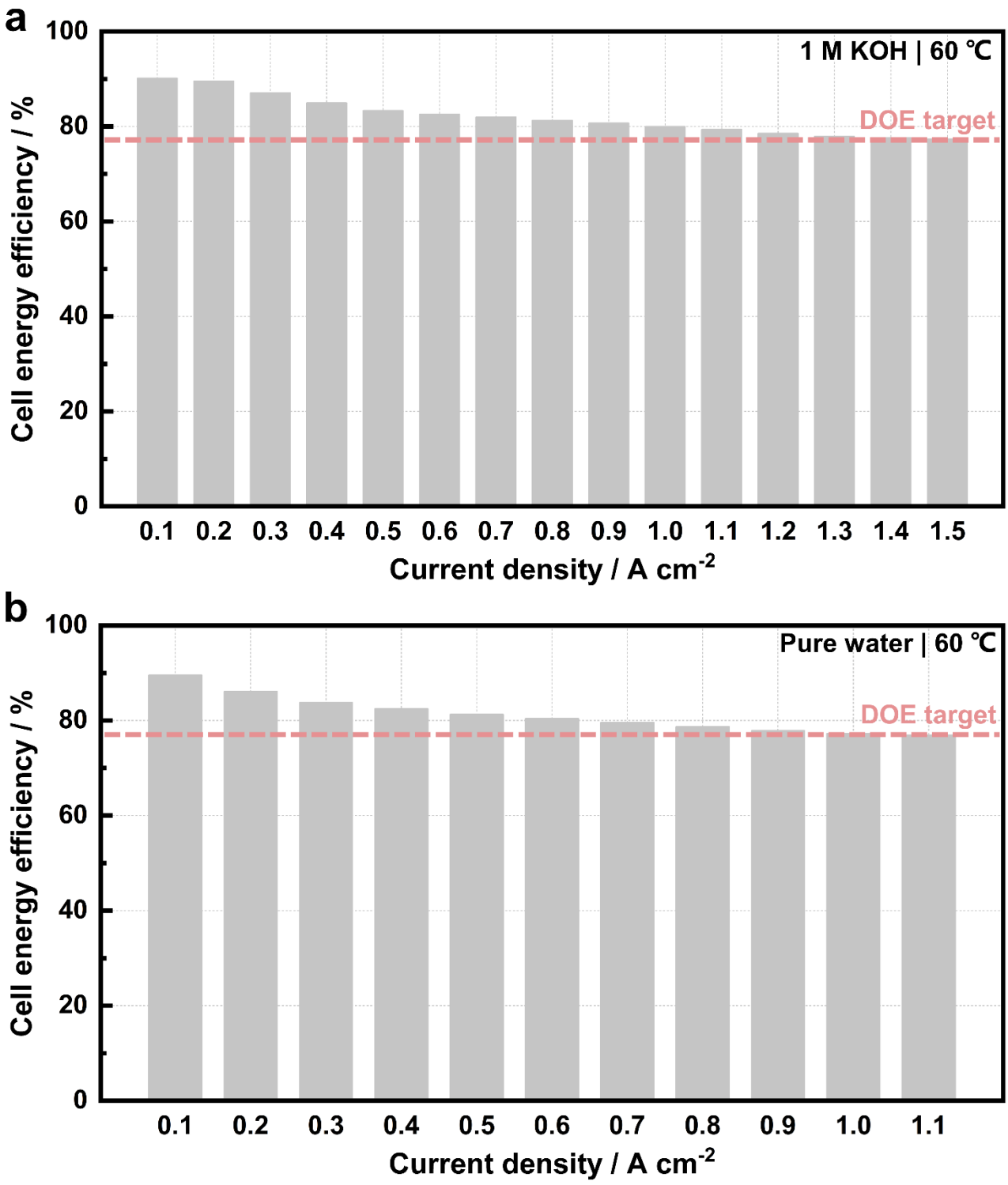

Fig. S60 | Cell energy efficiency at different current densities. Comparison of the Department of Energy (DOE) 2020 water electrolyzer efficiency target and the efficiency of AEMWE using 3D-ordered MEAs with NiCo@FeNi LDH in (a) 1 M KOH and (b) pure water, respectively.

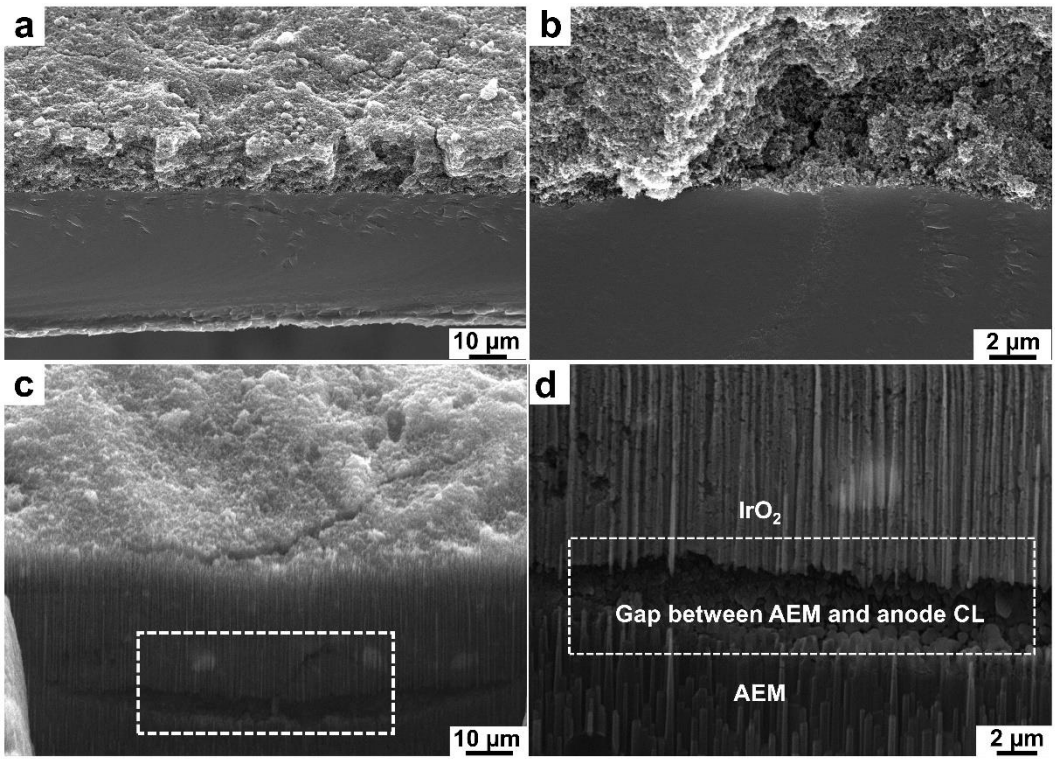

Fig. S61 | Morphology characterization of MEA-CCM after electrolysis. Cross-sectional FE-SEM images of (a-b) anode CL with IrO_2 on a AEM before durability test. Cross-sectional SEM images of (c-d) anode CL IrO_2 on a AEM during the FIB milling after durability test for 40 h.

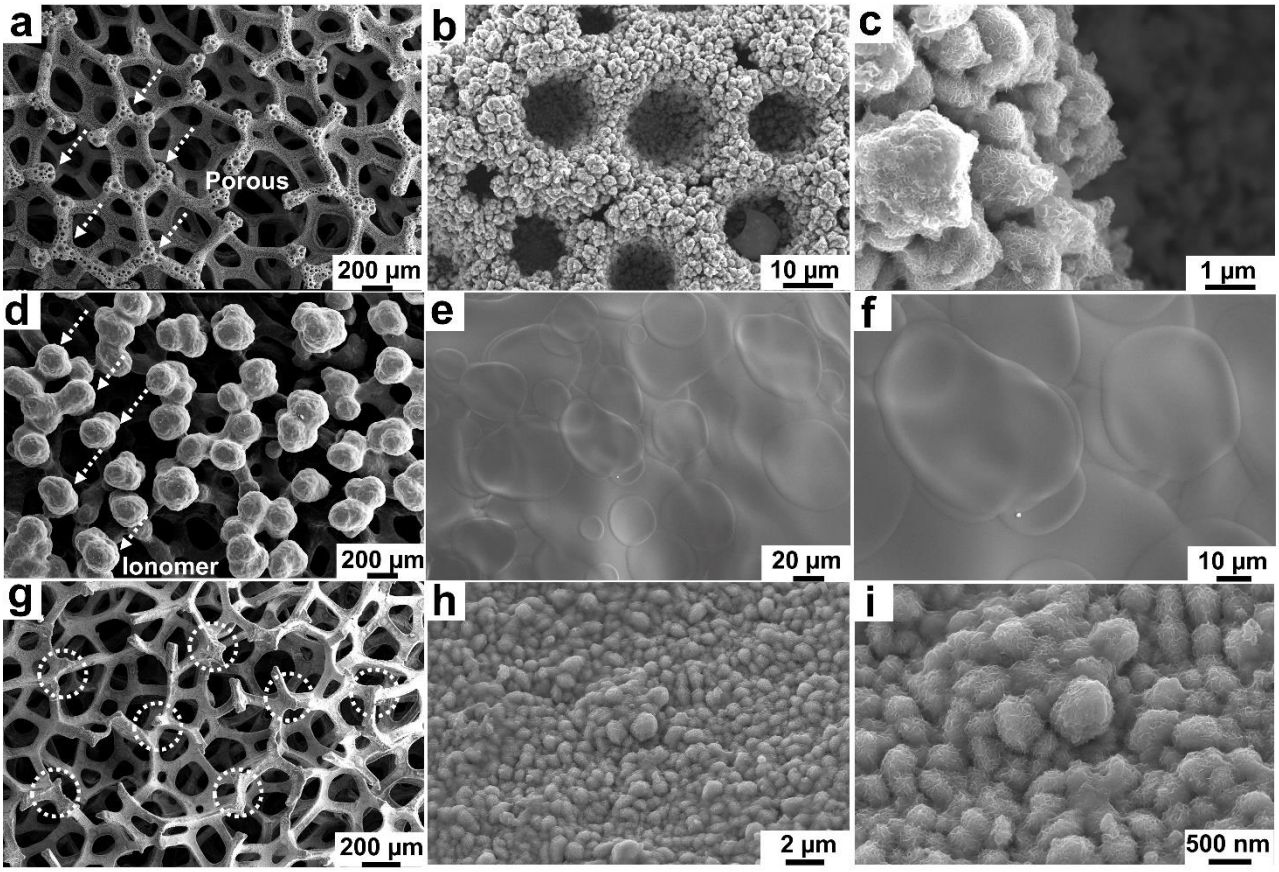

Fig. S62 | Morphology characterization of MEA-CCS before and after electrolysis. (a-c) The SEM iamges of ACL with NiCo@FeNi LDH foams on Ni foam before electrolysis. (d-f) The SEM images of ACL with ionomer-coated NiCo@FeNi LDH foams on Ni foam before electrolysis. (g-i) The SEM images of ACL with ionomer-coated NiCo@FeNi LDH foams on Ni foam after electrolysis.

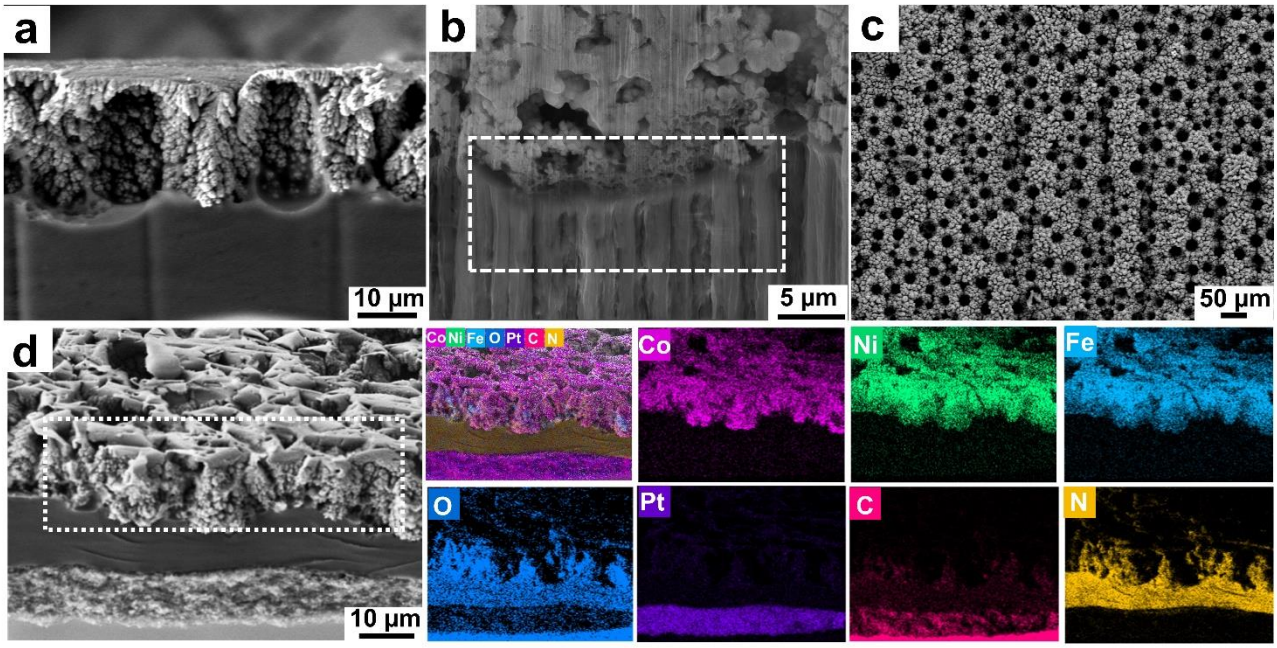

Fig. S63 | Morphology characterization of 3D-ordered MEA (NiCo@FeNi LDH) after electrolysis. (a-b) Cross-sectional and (c) surface FE-SEM images of 3D-ordered anode CL with NiCo@FeNi LDH on a AEM after durability test for 700 h in pure water. (d) The corresponding cross-sectional elemental mapping of anode CL with NiCo@FeNi LDH nanowire arrays on a AEM after durability test for 700 h in pure water.

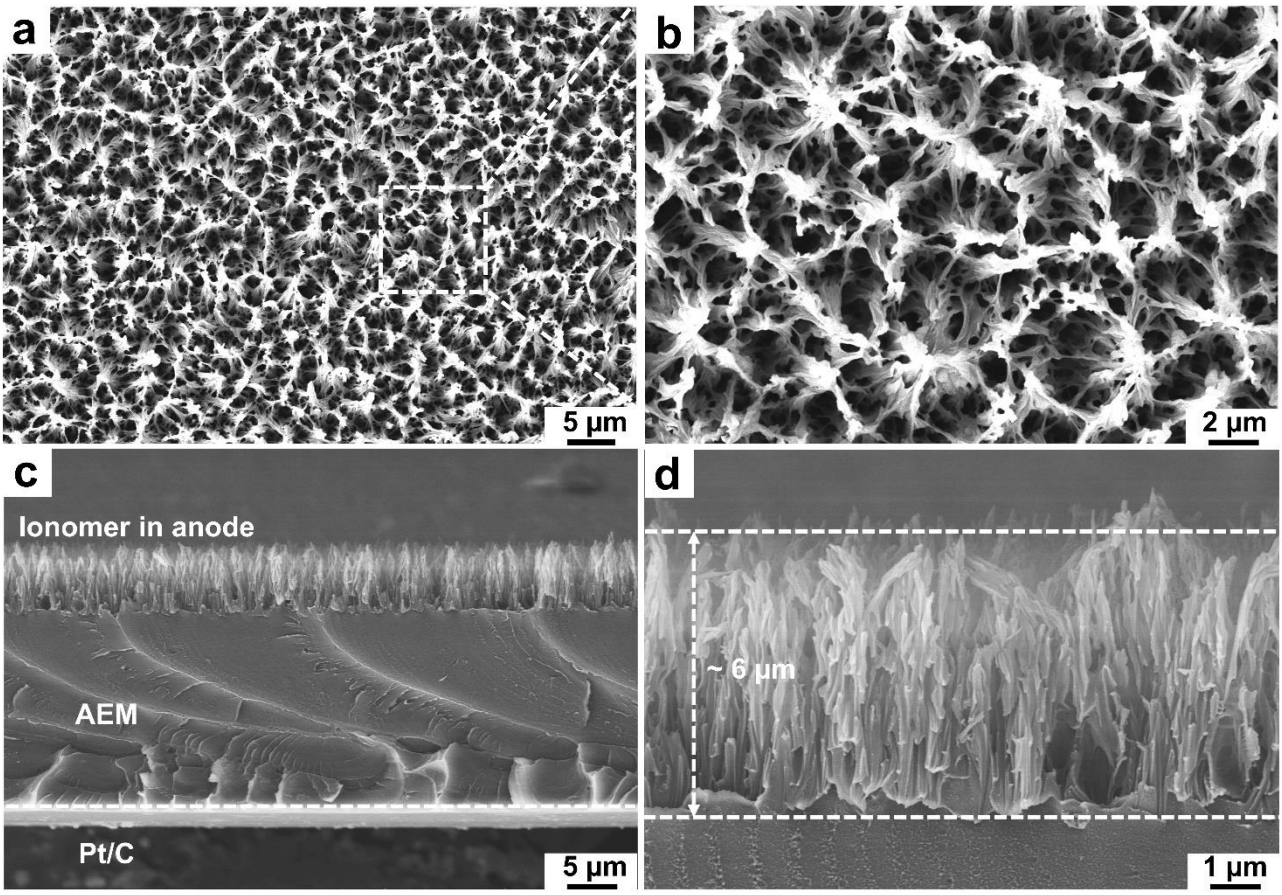

Fig. S64 | Morphology characterization of ionomer layer in 3D-ordered MEA (NiCo@FeNi LDH) after electrolysis. The (a-b) surface and (c-d) cross-section SEM images of of ionomer distribution in 3D-ordered ACL with NiCo@FeNi LDH on MEA after durability test for 700 h in pure water.

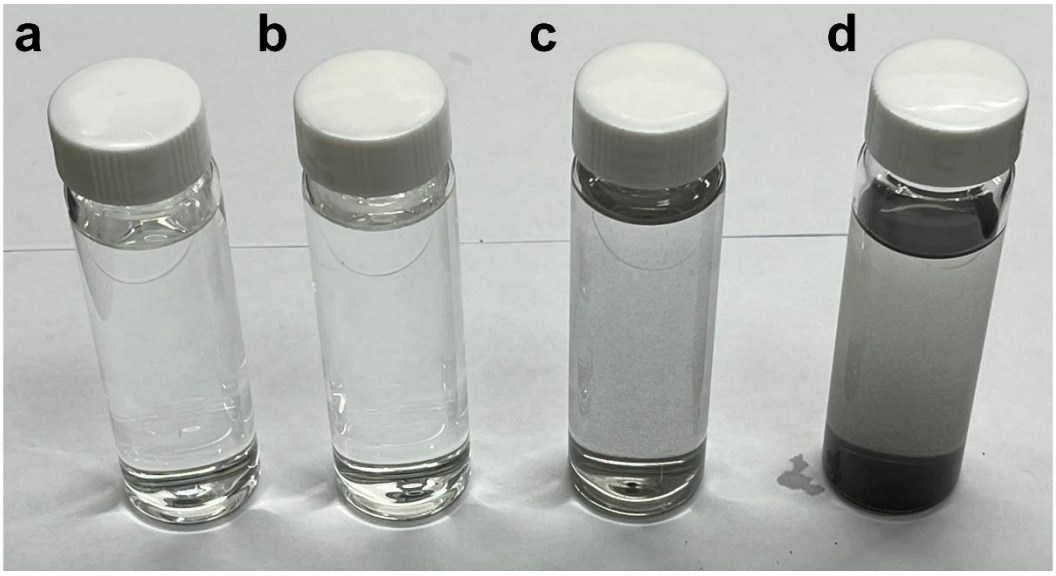

Fig. S65 | Electrolyte analysis after electrolysis. Digital images of (a) the pure reactant and the drain anode electrolytes of the AEM water electrolyzer using (b) 3D-ordered MEA (NiCo@FeNi LDH), (c) MEA-CCM (IrO_2), and (d) MEA-CCS (NiCo@FeNi LDH), respectively.

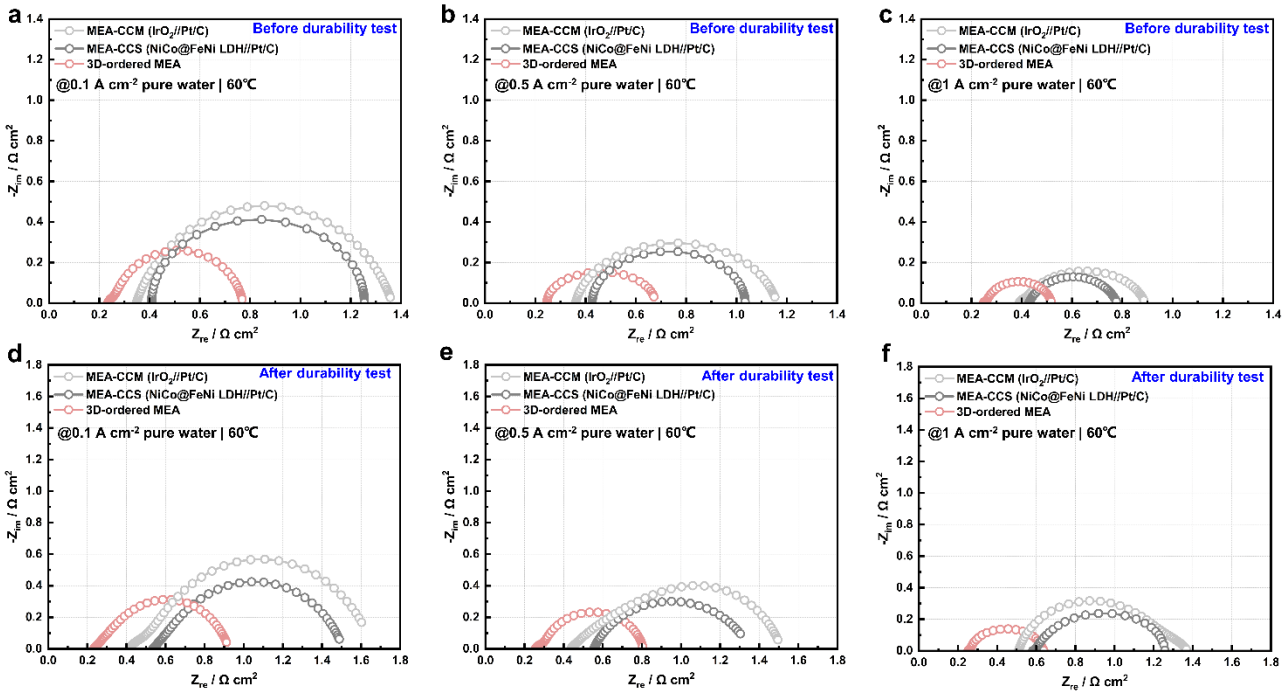

Fig. S66 | Nyquist plots from the EIS measurements before durability and after durability tests. Nyquist plot of MEA-CCM (IrO_2//Pt/C), MEA-CCS (NiCo@FeNi LDH//Pt/C) and 3D-ordered MEAs at (a) 0.1 A cm^{-2}, (b) 0.5 A cm^{-2}, and (c) 1.0 A cm^{-2} in 1 M KOH at 60°C before durability test. Nyquist plot of MEA-CCM (IrO_2//Pt/C), MEA-CCS (NiCo@FeNi LDH//Pt/C) and 3D-ordered MEAs at (d) 0.1 A cm^{-2}, (e) 0.5 A cm^{-2}, and (f) 1.0 A cm^{-2} in 1 M KOH at 60°C after durability test.

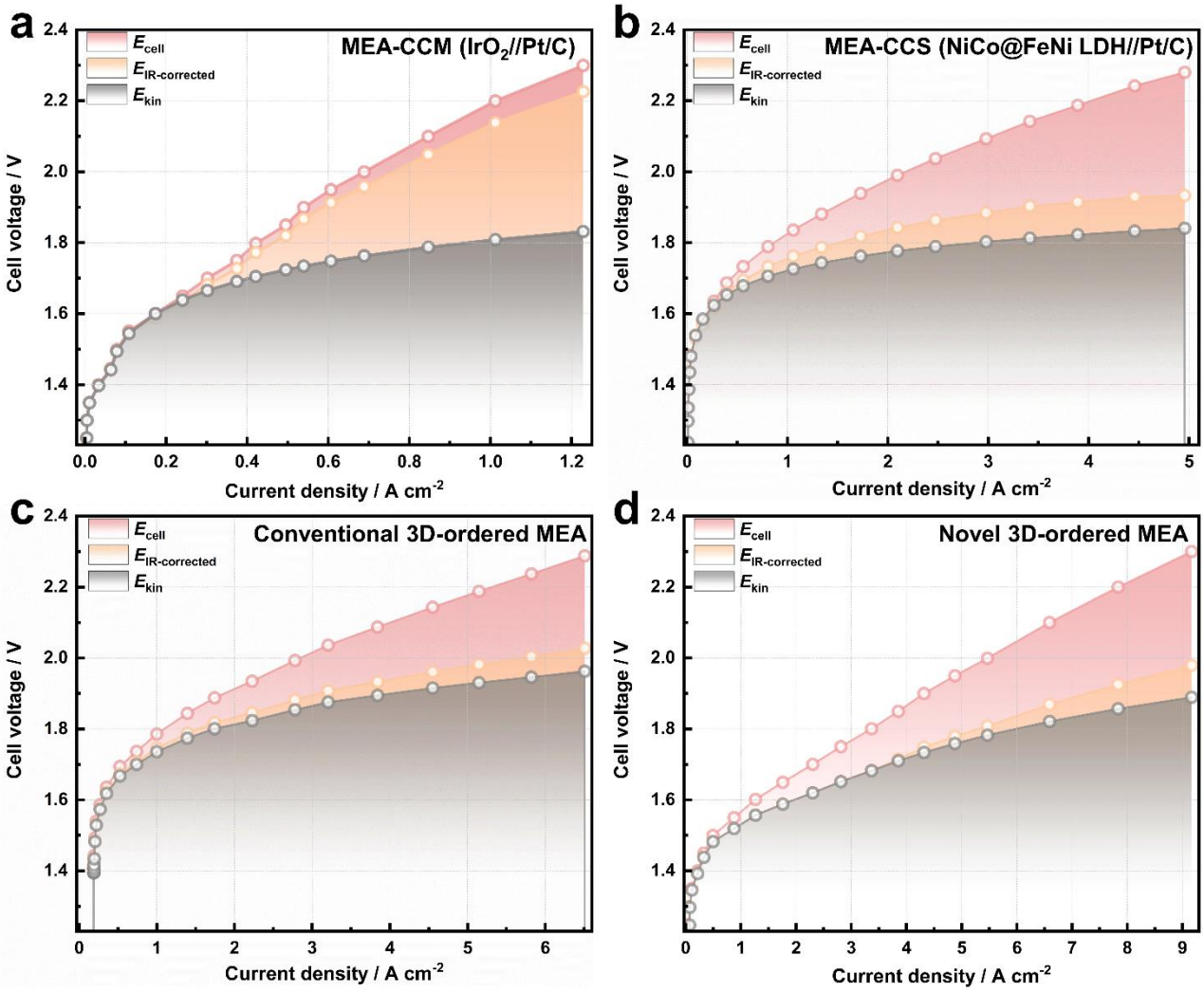

Fig. S67 | Overvoltage analysis of MEAs. The cell voltage, iR-corrected voltage, and kinetic voltage for the AEM water electrolysis in 1 M KOH at 60 ℃. (a) MEA-CCM (IrO_2//Pt/C), (b) MEA-CCS (NiCo@FeNi LDH//Pt/C), (c) conventional 3D-ordered MEA (NiCo@FeNi LDH//Pt/C), and (d) novel 3D-ordered MEA NiCo@FeNi LDH//Pt/C).

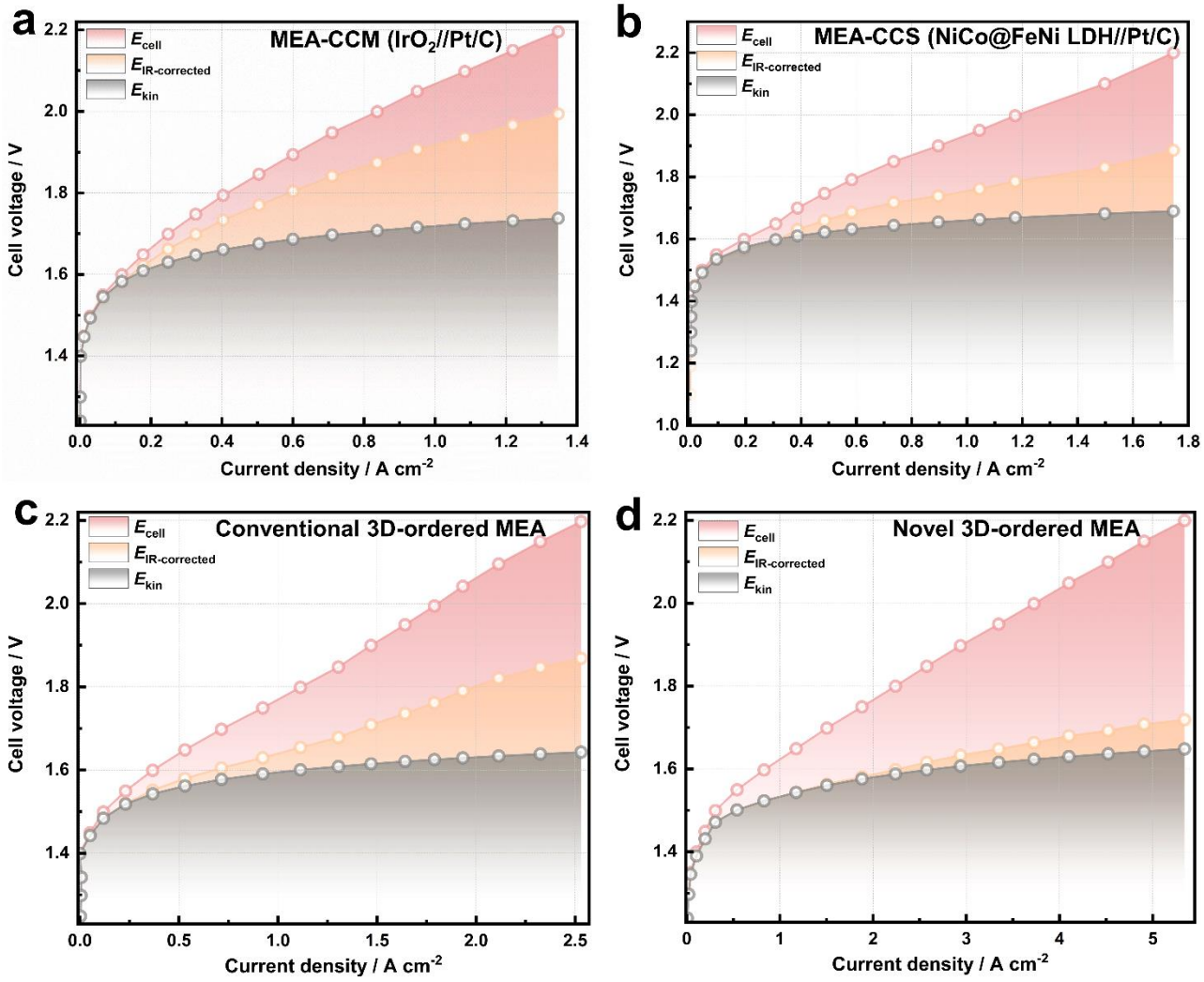

Fig. S68 | Overvoltage analysis of MEAs. The cell voltage, iR-corrected voltage, and kinetic voltage for the AEM water electrolysis in pure water at 60 °C. (a) MEA-CCM (IrO_2//Pt/C), (b) MEA-CCS (NiCo@FeNi LDH//Pt/C), (c) conventional 3D-ordered MEA (NiCo@FeNi LDH//Pt/C), and (d) novel 3D-ordered MEA NiCo@FeNi LDH//Pt/C).

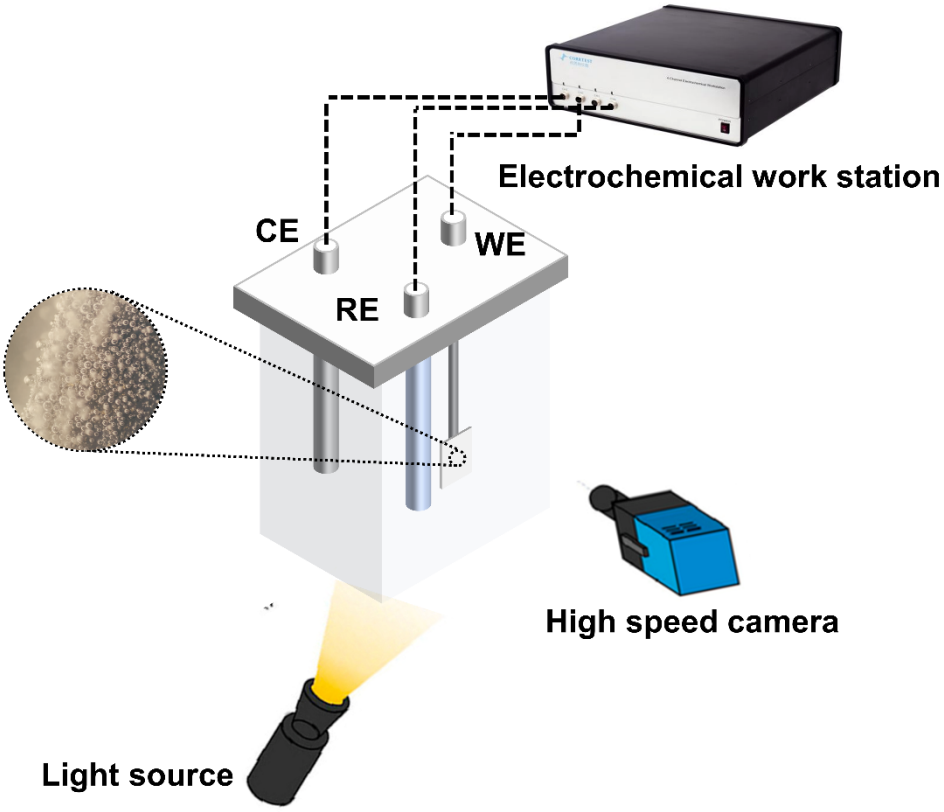

Fig. S69 | Schematic of the three electrode system for high-speed recording of the OER process.

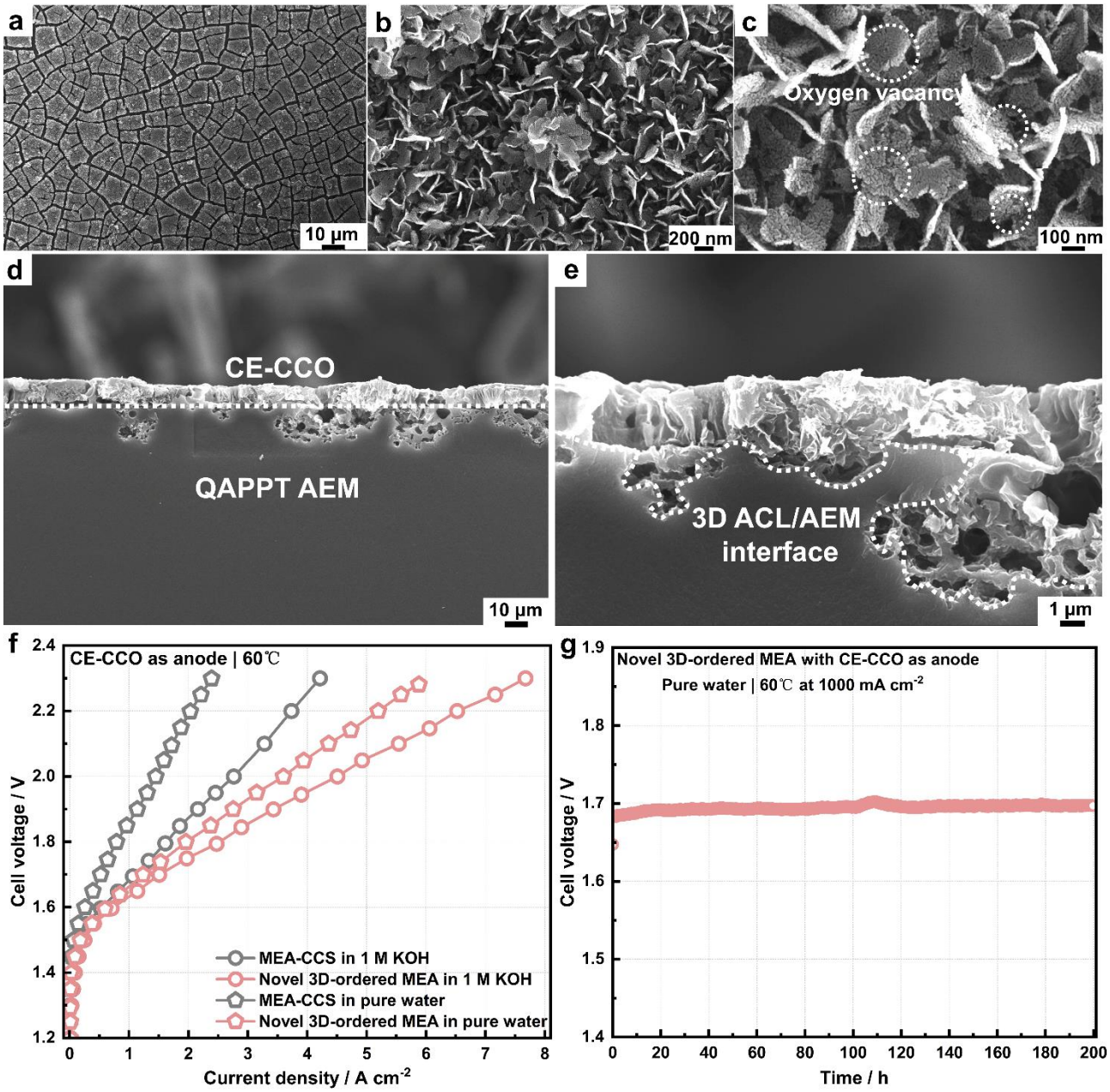

Fig. S70 | Generality of the swelling-assisted transfer strategy. (a-c) Surface SEM images of the CE-CCO ACL. (d-e) Cross-sectional SEM images of the CE-CCO ACL. (f) The polarization curves of MEA-CCS (CE-CCO//Pt/C) and novel 3D-ordered MEA using the CE-CCO ACL in 1 M KOH and pure water. (g) The stability test of water-fed AEM water electrolysis at 1000 mA cm^{-2} and 60 °C.

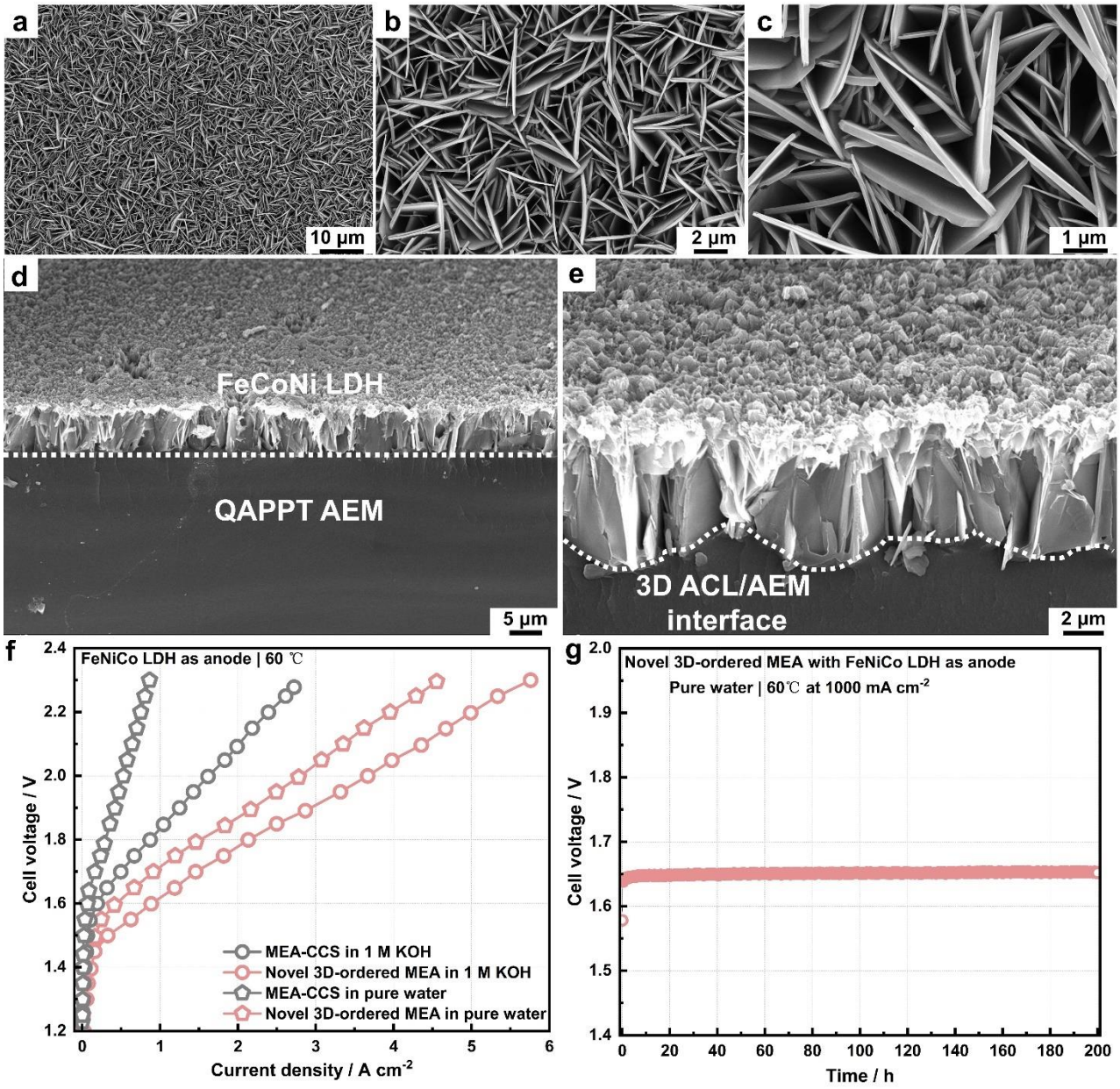

Fig. S71 | Generality of the swelling-assisted transfer strategy. (a-c) Surface SEM images of the FeCoNi LDH ACL. (d-e) Cross-sectional SEM images of the FeCoNi LDH ACL. (f) The polarization curves of MEA-CCS (FeCoNi LDH//Pt/C) and novel 3D-ordered MEA using the FeCoNi LDH ACL in 1 M KOH and pure water. (g) The stability test of water-fed AEM water electrolysis at 1000 mA cm^{-2} and 60 °C.

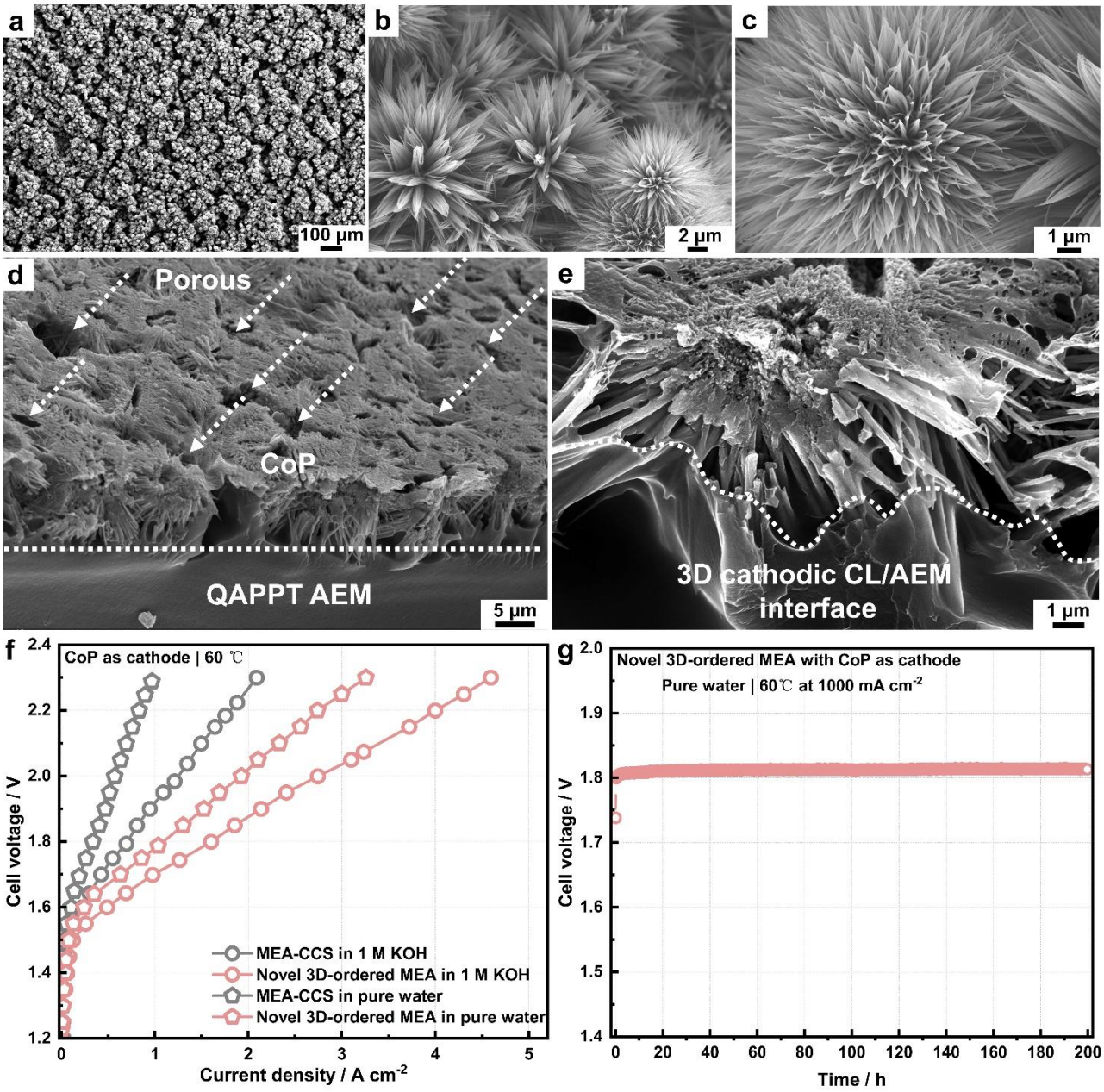

Fig. S72 | Generality of the swelling-assisted transfer strategy. (a-c) Surface SEM images of the CoP CCL. (d-e) Cross-sectional SEM images of the CoP CCL. (f) The polarization curves of MEA-CCS (IrO_2//CoP) and novel 3D-ordered MEA using the CoP CCL in 1 M KOH and pure water. (g) The stability test of water-fed AEM water electrolysis at 1000 mA cm^{-2} and 60 °C.

Table S1 | Overpotential (HER and OER) of electrocatalysts, hydroxide conductivity of AEMs and energy efficiency (at 500 mA cm^{-2}) of AEM water electrolysis (in 1 M KOH) comparison reported recently.

Anode	Cathode	Membrane	η_{OER} at j_{10} / mV	η_{HER} at j_{10} / mV	Conductivity / mS cm^{-1}	EE at 500 mA cm^{-2} /%	Ref.
$CuCoO_4$	Pt/C	X37-50 Grade T	270 mV	36 mV	130 at 80 °C	74.1	[5]
CuCoO	NiCoO-NiCo/C	X37-50 Grade T	285 mV	123 mV	130 at 80 °C	64.9	[6]
$Ni_2P@FePO_xH_y$	$MoNi_4/MoO_2$	X37-50 Grade T	220 mV	37 mV	130 at 80 °C	68.6	[7]
NiFeCo LDH	NiFeCoP	X37-50 Grade T	170 mV	37 mV	130 at 80 °C	69.8	[8]
FeNiPS	FeNiPS	FAA-3-50	180 mV	85 mV	60 at 80 °C	74.1	[9]
NiFe	Ni	FAA-3-50	310 mV	275 mV	60 at 80 °C	58.5	[10]
$Ni_{0.75}Fe_{2.25}O_4$	Pt/C	X37-50 Grade T	192 mV	36 mV	130 at 80 °C	75.0	[11]
CdS/ZIF-67	Pt/C	FAA-3-50	294 mV	36 mV	60 at 80 °C	69.8	[12]
Ir black	Pt/C	HMT-PMBI	328 mV	36 mV	131 at 80 °C	74.5	[13]
IrO_2	Pt/C	A201	310 mV	36 mV	70 at 80 °C	70.2	[14]
IrO_2	Pt/C	A201	310 mV	36 mV	70 at 80 °C	60.0	[15]
$NiCo_2O_4$	Pt/C	SEBS AEM	400 mV	36 mV	185 at 80 °C	61.9	[16]
IrO_2	Pt/C	Qmter-co-Mpi	310 mV	36 mV	66 at 80 °C	55.0	[17]
NiS_2/Ni_3S_4	Pt/C	FAA-3-50	305 mV	36 mV	60 at 80 °C	70.0	[18]
FeNi LDH	Pt/C	X37-50	250 mV	36 mV	130 at 80 °C	75.0	[19]
NiFe-LDH/KB	Pt/C	X37-50 Grade T	247 mV	36 mV	130 at 80 °C	78.9	[20]
NiFeOOH	Pt/C	FAA-3–50	210 mV	36 mV	60 at 80 °C	77.7	[21]
Fe_xNi_yOOH-F	Pt/C	PAP-TP	155 mV	36 mV	175 at 80 °C	76.4	[22]
$CoSb_2O_6$	Pt/C	FAA-3-50	170 mV	36 mV	60 at 80 °C	67.2	[23]
$(NiCo)_3Se_4$	Pt/C	X37-50	268 mV	36 mV	130 at 80 °C	73.2	[24]
Fe-NiMo	NiMo	X37-50 Grade T	192 mV	11 mV	130 at 80 °C	78.4	[25]
FeNi LDH	Pt/C	HWU-AEM	250 mV	36 mV	100 at 80 °C	69.2	[26]
$Cu_{0.5}Co_{2.5}O_4$	Pt/C	X37-50 Grade T	285 mV	36 mV	130 at 80 °C	72.7	[27]
NiFe	Pt/C	PFTP	310 mV	36 mV	163 at 80 °C	80.0	[28]

Table S2 | Comparison of the activities of different OER electrocatalysts.

Catalysts	Overpotential at j_{100} / mV	Tafel slope / mV dec^{-1}	Ref.
Ni_5P_4/NiP_2/NiFe LDH	243	47	29
$NiCo_2S_4$@CoFeMo LDH	230	83	30
Cu@NiFe LDH	281	28	31
V-Ni_3S_2@NiFe LDH	286	33	32
$NiFeO_xH_y$-PN	265	24	33
NiFe-LDH@$FeNi_2S_4$	240	29	34
Ni-Fe-OH@Ni_3S_2	320	93	35
NiFe LDH	275	49	36
NiLa-LDH	325	45	37
NiFe-LDH	293	51	38
$Fe(OH)_3/Ni(OH)_2$	300	92	39
NiFeV LDH	270	33	40
NiFeCr	250	28	41
NiFe	225	35	42
NiFe	270	41	43
NiFe	290	45	44
$CoMoN_x$	300	51	45
Fe_2Ni_2N	260	34	46
Co_3FeN_x	253	46	47
CoN	330	70	48
CoVFeN	264	35	49
$CoSb_2O_6$	360	46	23
$Zn_xCo_{3-x}O_4$	470	51	50
$Co_{0.37}Ni_{0.26}Fe_{0.37}O$	272	38	51
$CuCoO_4$	310	71	5
$Ni_{12}P_{5-x}Br_x/Ni_2P$	330	56	52
FeP/Ni_2P	250	47	53
Fe-CoP	187	66	54
Cu_3P/Ni_2P	400	72	55
Ni-Co-Fe-P	221	29	56
Fe-NiSe	200	43	57

NiFe-Se	390	41	[58]
Fe–Ni–Se	290	61	[59]
$Ni_{0.75}Fe_{0.25}Se_2$	255	27	[60]
$Cu_2Se/NiSe_2$	290	40	[61]
FeCoNiS	195	23	[62]
CoFe-Ni_4S_3	279	63	[63]
$NiCo_2S_4$	320	61	[64]
NiFeS	230	55	[65]
$NiCo_2O_4$@FeNi LDH	208	47	This work
NiCo@FeNi LDH	180	34	This work

Table S3 | Comparison of electrolysis performance between this work and alkaline liquid water electrolysis (ALWE) reported in literatures

Anode	Cathode	Separator	Current density / mA cm^{-2}	Voltage / V	Ref.
Ni foam	Ni foam	*mes*-PBI	50	1.84	[66]
FeNi LDH	$MoNi_4$	PSU-PVP	200	1.69	[67]
FeNi LDH	CoP	PTFE-LDH	250	1.70	[68]
Ni plate	Ni plate	Porous PFSA	150	2.21	[69]
FeNi LDH	Raney-Ni	Zirfon-cPVAZ	300	1.73	[70]
FeNi LDH	Raney-Ni	PSU-CeO_2	400	1.96	[71]
FeNi LDH	Raney-Ni	Zirfon	320	1.63	[72]
FeNi LDH	Raney-Ni	PSU-ZrO_2-CNC	220	1.58	[73]
FeNi LDH	Raney-Ni	PSU-ZAT	180	1.56	[74]
IrO_2	Pt/C	NPBI	380	1.55	[75]
Ni plate	Ni plate	Crosslinked PBI	240	2.08	[76]
Raney-Ni	Raney-Ni	PES-PVP	350	1.97	[77]
Ni foam	Ni foam	PBI-PVA	375	1.94	[78]

Table S4 | Comparison of electrolysis performance between this work and AEMWE reported in literatures

Anode	Cathode	Separator	Current density / mA cm^{-2}	Voltage / V	Ref.
$Cu_{0.5}Co_{2.5}O_4$	Pt/C	X37-50 Grade T	1080	1.80	[27]
FeNi LDH	NiMo	PVBC-MPy/PEK	800	2.11	[43]
$NiFe_2O_4$	NiFeCO	C-IL-100 AEM	500	1.98	[79]
NiFe	Pt/C	QPP-b-PSK-TMA	1100	1.60	[80]
CuCo-oxide	Pt/C	X37-50 Grade T	1600	1.84	[5]
$MoNi_4/MoO_2$	$Ni_2P@FePO_xH_y$	X37-50 Grade T	504	1.85	[7]
CuCoO	NiCoO-NiCo/C	X37− 50 Grade T	700	1.79	[6]
NiFeCo LDH	NiFeCoP	X37-50 Grade T	500	1.72	[8]
S-FeOOH	Pt mesh	FAA-3-50	1000	1.95	[81]
FeNi LDH	NiMo	PVBC-MPy-PSF	650	1.94	[82]
IrO_2	Pt/C	PISPVA	550	2.00	[83]
Ni foam	Ni foam	PAEK-APBI	1500	2.27	[84]
Ni foam	Ni foam	FAA-mPBI	500	2.25	[85]
IrO_2	Pt/C	PDTP	1000	1.85	[86]
IrO_2	Pt/C	SEBS-Pi	800	2.24	[87]
Ir black	Pt/C	HMT-PMBI	1000	1.70	[13]
$NiCo_2O_4$	Pt/C	SEBS AEM	700	2.00	[16]
$NiFe_2O_4$	PtNi/ECS	GT72-10 AEM	810	1.80	[88]
IrO_2	Pt/C	QMter-co-Mpi	510	2.20	[17]
FeNi-PS	FeNi-PS	FAA-3-50	1200	1.80	[9]
$Ni_{0.75}Fe_{2.25}O_4$	Pt/C	X37-50 Grade T	1050	1.75	[11]
NiS_2/Ni_3S_4	Pt/C	FAA-3-50	1200	1.90	[18]
FeNi LDH	Pt/C	X37-50 Grade T	900	1.68	[19]
FeNi LDH/KB	Pt/C	X37-50 Grade T	1000	1.59	[20]

Table S5 | Comparison of electrolysis performance between this work and PEM water electrolyzers reported in literatures

Anode	Cathode	PEM	Current density / mA cm^{-2}	Voltage / V	Ref.
IrO_2	FeS_2/C	N115	2000	2.30	[89]
IrO_2	Pt/C	N117	2000	1.90	[90]
Ir@WO_x	Pt/C	N115	2500	2.05	[91]
IrO_2	$Ni_{0.46}P_{0.54}$	N212	1470	2.00	[92]
IrO_2	Pt/C	N115	4000	2.20	[93]
IrO_2	Pt/C	sPPS	1490	1.80	[94]
$Ir_xRu_{1-x}O_2$	Pt/C	N115	1850	2.00	[95]
npIr_x-NS	Pt/C	N117	3000	1.98	[96]
IrO_2	Pt/C	N117	2700	1.91	[97]
IrO_x	Pt/C	N117	1800	1.90	[98]
IrO_2@TiO_2	Pt/C	N212	4000	1.88	[99]
$IrRuO_x$	MoS_2NSs	N115	2000	2.25	[100]
Ir/Au	Pt/C	N212	3250	1.87	[101]
IrO_2	Pt/C	N115	1750	1.70	[102]
IrO_2	Pt/C	N115	3100	2.12	[103]
IrO_2	Pt/C	N117	2500	2.11	[104]
IrO_2	Pt/C	SPAES	2100	1.77	[105]

References

1. H. Peng, Q. Li, M. Hu, L. Xiao, J. Lu and L. Zhuang, *Journal of Power Sources*, 2018, **390**, 165-167.
2. Y. S. Park, J. Yang, J. Lee, M. J. Jang, J. Jeong, W.-S. Choi, Y. Kim, Y. Yin, M. H. Seo, Z. Chen and S. M. Choi, *Applied Catalysis B: Environmental*, 2020, **278**.
3. L. Wan, Z. Xu, P. Wang, P.-F. Liu, Q. Xu and B. Wang, *Chemical Engineering Journal*, 2022, **431**, 133942.
4. J. Tian, Q. Liu, A. M. Asiri and X. Sun, *J Am Chem Soc*, 2014, **136**, 7587-7590.
5. D. Li, E. J. Park, W. Zhu, Q. Shi, Y. Zhou, H. Tian, Y. Lin, A. Serov, B. Zulevi, E. D. Baca, C. Fujimoto, H. T. Chung and Y. S. Kim, *Nature Energy*, 2020, **5**, 378-385.
6. Y. S. Park, J. Jeong, Y. Noh, M. J. Jang, J. Lee, K. H. Lee, D. C. Lim, M. H. Seo, W. B. Kim, J. Yang and S. M. Choi, *Applied Catalysis B: Environmental*, 2021, **292**.
7. A. Meena, P. Thangavel, D. S. Jeong, A. N. Singh, A. Jana, H. Im, D. A. Nguyen and K. S. Kim, *Applied Catalysis B: Environmental*, 2022, **306**.
8. J. Lee, H. Jung, Y. S. Park, N. Kwon, S. Woo, N. C. S. Selvam, G. S. Han, H. S. Jung, P. J. Yoo, S. M. Choi, J. W. Han and B. Lim, *Applied Catalysis B: Environmental*, 2021, **294**.
9. M. Yang, M. Zhao, J. Yuan, J. Luo, J. Zhang, Z. Lu, D. Chen, X. Fu, L. Wang and C. Liu, *Small*, 2022, **18**, e2106554.
10. E. López-Fernández, C. Gómez-Sacedón, J. Gil-Rostra, J. P. Espinós, A. R. González-Elipe, F. Yubero and A. de Lucas-Consuegra, *Chemical Engineering Journal*, 2022, **433**.
11. J. Lee, H. Jung, Y. S. Park, S. Woo, N. Kwon, Y. Xing, S. H. Oh, S. M. Choi, J. W. Han and B. Lim, *Chemical Engineering Journal*, 2021, **420**.
12. K. C. Devarayapalli, J. Lee, S. Kang, S. Moon, S. V. P. Vattikuti, J. Lee and K. Lee, *Journal of Power Sources*, 2022, **527**.
13. P. Fortin, T. Khoza, X. Cao, S. Y. Martinsen, A. Oyarce Barnett and S. Holdcroft, *Journal of Power Sources*, 2020, **451**.
14. M. K. Cho, H.-Y. Park, H. J. Lee, H.-J. Kim, A. Lim, D. Henkensmeier, S. J. Yoo, J. Y. Kim, S. Y. Lee, H. S. Park and J. H. Jang, *Journal of Power Sources*, 2018, **382**, 22-29.
15. M. K. Cho, H.-Y. Park, S. Choe, S. J. Yoo, J. Y. Kim, H.-J. Kim, D. Henkensmeier, S. Y. Lee, Y.-E. Sung, H. S. Park and J. H. Jang, *Journal of Power Sources*, 2017, **347**, 283-290.
16. G. Gupta, K. Scott and M. Mamlouk, *Journal of Power Sources*, 2018, **375**, 387-396.
17. X. Yan, X. Yang, X. Su, L. Gao, J. Zhao, L. Hu, M. Di, T. Li, X. Ruan and G. He, *Journal of Power Sources*, 2020, **480**.
18. L. Xia, W. Jiang, H. Hartmann, J. Mayer, W. Lehnert and M. Shviro, *ACS Appl Mater Interfaces*, 2022, **14**, 19397-19408.
19. S. S. Jeon, J. Lim, P. W. Kang, J. W. Lee, G. Kang and H. Lee, *ACS Appl Mater Interfaces*, 2021, **13**, 37179-37186.
20. H. Koshikawa, H. Murase, T. Hayashi, K. Nakajima, H. Mashiko, S. Shiraishi and Y. Tsuji, *ACS Catalysis*, 2020, **10**, 1886-1893.
21. J. E. Park, S. Park, M.-J. Kim, H. Shin, S. Y. Kang, Y.-H. Cho and Y.-E. Sung, *ACS Catalysis*, 2021, **12**, 135-145.
22. J. Xiao, A. M. Oliveira, L. Wang, Y. Zhao, T. Wang, J. Wang, B. P. Setzler and Y. Yan, *ACS Catalysis*, 2020, **11**, 264-270.
23. K. Ham, S. Hong, S. Kang, K. Cho and J. Lee, *ACS Energy Letters*, 2021, **6**, 364-370.
24. J. Abed, S. Ahmadi, L. Laverdure, A. Abdellah, C. P. O'Brien, K. Cole, P. Sobrinho, D. Sinton, D. Higgins, N. J. Mosey, S. J. Thorpe and E. H. Sargent, *Adv Mater*, 2021, **33**, e2103812.
25. P. Chen and X. Hu, *Advanced Energy Materials*, 2020, **10**.
26. Z. Xu, L. Wan, Y. Liao, P. Wang, K. Liu and B. Wang, *Journal of Materials Chemistry A*, 2021, **9**, 23485-23496.
27. M. J. Jang, J. Yang, J. Lee, Y. S. Park, J. Jeong, S. M. Park, J.-Y. Jeong, Y. Yin, M.-H. Seo, S. M. Choi and K. H. Lee, *Journal of Materials Chemistry A*, 2020, **8**, 4290-4299.
28. N. Chen, S. Y. Paek, J. Y. Lee, J. H. Park, S. Y. Lee and Y. M. Lee, *Energy & Environmental Science*, 2021, **14**, 6338-6348.
29. L. Yu, H. Zhou, J. Sun, I. K. Mishra, D. Luo, F. Yu, Y. Yu, S. Chen and Z. Ren, *Journal of Materials Chemistry A*, 2018, **6**, 13619-13623.
30. X. Shen, H. Li, Y. Zhang, T. Ma, Q. Li, Q. Jiao, Y. Zhao, H. Li and C. Feng, *Applied Catalysis B: Environmental*, 2022, **319**.
31. L. Yu, H. Zhou, J. Sun, F. Qin, F. Yu, J. Bao, Y. Yu, S. Chen and Z. Ren, *Energy & Environmental Science*, 2017, **10**, 1820-1827.
32. J. Zhou, L. Yu, Q. Zhu, C. Huang and Y. Yu, *Journal of Materials Chemistry A*, 2019, **7**, 18118-18125.
33. B. Zhong, P. Kuang, L. Wang and J. Yu, *Applied Catalysis B: Environmental*, 2021, **299**.
34. L. Tan, J. Yu, C. Wang, H. Wang, X. Liu, H. Gao, L. Xin, D. Liu, W. Hou and T. Zhan, *Advanced Functional Materials*, 2022, **32**.
35. X. Zou, Y. Liu, G. D. Li, Y. Wu, D. P. Liu, W. Li, H. W. Li, D. Wang, Y. Zhang and X. Zou, *Adv Mater*, 2017, **29**.
36. P. Wang, Y. Lin, Q. Xu, Z. Xu, L. Wan, Y. Xia and B. Wang, *ACS Applied Energy Materials*, 2021, **4**, 9022-9031.
37. S. Jiang, Y. Liu, W. Xie and M. Shao, *Journal of Energy Chemistry*, 2019, **33**, 125-129.
38. Z. Sun, Y. Wang, L. Lin, M. Yuan, H. Jiang, R. Long, S. Ge, C. Nan, H. Li, G. Sun and X. Yang, *Chem Commun (Camb)*, 2019, **55**, 1334-1337.
39. N. Yu, W. Cao, M. Huttula, Y. Kayser, P. Hoenicke, B. Beckhoff, F. Lai, R. Dong, H. Sun and B. Geng, *Applied Catalysis B: Environmental*, 2020, **261**.
40. J. Lee, H. Jung, Y. S. Park, S. Woo, J. Yang, M. J. Jang, J. Jeong, N. Kwon, B. Lim, J. W. Han and S. M. Choi, *Small*, 2021, **17**, e2100639.
41. L. Fan, P. Zhang, B. Zhang, Q. Daniel, B. J. J. Timmer, F. Zhang and L. Sun, *ACS Energy Letters*, 2018, **3**, 2865-2874.
42. C. Liang, P. Zou, A. Nairan, Y. Zhang, J. Liu, K. Liu, S. Hu, F. Kang, H. J. Fan and C. Yang, *Energy & Environmental Science*,

2020, **13**, 86-95.
43. X. Teng, J. Wang, L. Ji, Y. Liu, C. Zhang and Z. Chen, *ACS Sustainable Chemistry & Engineering*, 2019, **7**, 5412-5419.
44. C. L. Huang, X. F. Chuah, C. T. Hsieh and S. Y. Lu, *ACS Appl Mater Interfaces*, 2019, **11**, 24096-24106.
45. Y. Lu, Z. Li, Y. Xu, L. Tang, S. Xu, D. Li, J. Zhu and D. Jiang, *Chemical Engineering Journal*, 2021, **411**.
46. M. Jiang, Y. Li, Z. Lu, X. Sun and X. Duan, *Inorganic Chemistry Frontiers*, 2016, **3**, 630-634.
47. Y. Wang, D. Liu, Z. Liu, C. Xie, J. Huo and S. Wang, *Chem Commun (Camb)*, 2016, **52**, 12614-12617.
48. Y. Zhang, B. Ouyang, J. Xu, G. Jia, S. Chen, R. S. Rawat and H. J. Fan, *Angew Chem Int Ed Engl*, 2016, **55**, 8670-8674.
49. D. Liu, H. Ai, J. Li, M. Fang, M. Chen, D. Liu, X. Du, P. Zhou, F. Li, K. H. Lo, Y. Tang, S. Chen, L. Wang, G. Xing and H. Pan, *Advanced Energy Materials*, 2020, **10**.
50. X. Liu, Z. Chang, L. Luo, T. Xu, X. Lei, J. Liu and X. Sun, *Chemistry of Materials*, 2014, **26**, 1889-1895.
51. W. Chen, H. Wang, Y. Li, Y. Liu, J. Sun, S. Lee, J. S. Lee and Y. Cui, *ACS Cent Sci*, 2015, **1**, 244-251.
52. L. Wan, Z. Xu, Q. Xu, P. Wang and B. Wang, *Energy & Environmental Science*, 2022, **15**, 1882-1892.
53. X. Xu, X. Tian, Z. Zhong, L. Kang and J. Yao, *Journal of Power Sources*, 2019, **424**, 42-51.
54. Y. Li, F. Li, Y. Zhao, S.-N. Li, J.-H. Zeng, H.-C. Yao and Y. Chen, *Journal of Materials Chemistry A*, 2019, **7**, 20658-20666.
55. H. Liu, J. Gao, X. Xu, Q. Jia, L. Yang, S. Wang and D. Cao, *Chemical Engineering Journal*, 2022, **448**.
56. A. Li, L. Zhang, F. Wang, L. Zhang, L. Li, H. Chen and Z. Wei, *Applied Catalysis B: Environmental*, 2022, **310**.
57. Z. Zou, X. Wang, J. Huang, Z. Wu and F. Gao, *Journal of Materials Chemistry A*, 2019, **7**, 2233-2241.
58. Y. Guo, C. Zhang, J. Zhang, K. Dastafkan, K. Wang, C. Zhao and Z. Shi, *ACS Sustainable Chemistry & Engineering*, 2021, **9**, 2047-2056.
59. J. Du, A. Yu, Z. Zou and C. Xu, *Inorganic Chemistry Frontiers*, 2018, **5**, 814-818.
60. Y. Huang, L.-W. Jiang, X.-L. Liu, T. Tan, H. Liu and J.-J. Wang, *Applied Catalysis B: Environmental*, 2021, **299**.
61. R. Bose, K. Karuppasamy, P. Arunkumar, G. K. Veerasubramani, S. Gayathri, P. Santhoshkumar, D. Vikraman, J. H. Han, H.-S. Kim and A. Alfantazi, *ACS Sustainable Chemistry & Engineering*, 2021, **9**, 13114-13123.
62. Y. Huang, L.-W. Jiang, H. Liu and J.-J. Wang, *Chemical Engineering Journal*, 2022, **441**.
63. X. Mao, Y. Liu, Z. Chen, Y. Fan and P. Shen, *Chemical Engineering Journal*, 2022, **427**.
64. H. Su, S. Song, Y. Gao, N. Li, Y. Fu, L. Ge, W. Song, J. Liu and T. Ma, *Advanced Functional Materials*, 2021, **32**.
65. P. Ganesan, A. Sivanantham and S. Shanmugam, *Journal of Materials Chemistry A*, 2016, **4**, 16394-16402.
66. D. Aili, A. G. Wright, M. R. Kraglund, K. Jankova, S. Holdcroft and J. O. Jensen, *Journal of Materials Chemistry A*, 2017, **5**, 5055-5066.
67. D. Aili, M. R. Kraglund, J. Tavacoli, C. Chatzichristodoulou and J. O. Jensen, *Journal of Membrane Science*, 2020, **598**.
68. L. Wan, Z. Xu and B. Wang, *Chemical Engineering Journal*, 2021, **426**.
69. D. Aili, M. K. Hansen, J. W. Andreasen, J. Zhang, J. O. Jensen, N. J. Bjerrum and Q. Li, *Journal of Membrane Science*, 2015, **493**, 589-598.
70. S. Kim, J. H. Han, J. Yuk, S. Kim, Y. Song, S. So, K. T. Lee and T.-H. Kim, *Journal of Power Sources*, 2022, **524**.
71. J. W. Lee, C. Lee, J. H. Lee, S. K. Kim, H. S. Cho, M. Kim, W. C. Cho, J. H. Joo and C. H. Kim, *Polymers (Basel)*, 2020, **12**.
72. H. I. Lee, M. Mehdi, S. K. Kim, H. S. Cho, M. J. Kim, W. C. Cho, Y. W. Rhee and C. H. Kim, *Journal of Membrane Science*, 2020, **616**.
73. J. W. Lee, J. H. Lee, C. Lee, H.-S. Cho, M. Kim, S.-K. Kim, J. H. Joo, W.-C. Cho and C.-H. Kim, *Chemical Engineering Journal*, 2022, **428**.
74. M. F. Ali, H. I. Lee, C. I. Bernacker, T. Weissgarber, S. Lee, S. K. Kim and W. C. Cho, *Polymers (Basel)*, 2022, **14**.
75. B. Hu, Y. Huang, L. Liu, X. Hu, K. Geng, Q. Ju, M. Liu, J. Bi, S. Luo and N. Li, *Journal of Membrane Science*, 2022, **643**.
76. D. Aili, M. K. Hansen, R. F. Renzaho, Q. Li, E. Christensen, J. O. Jensen and N. J. Bjerrum, *Journal of Membrane Science*, 2013, **447**, 424-432.
77. S. Lu, L. Zhuang and J. Lu, *Journal of Membrane Science*, 2007, **300**, 205-210.
78. L. A. Diaz, R. E. Coppola, G. C. Abuin, R. Escudero-Cid, D. Herranz and P. Ocón, *Journal of Membrane Science*, 2017, **535**, 45-55.
79. X. Wang and R. G. H. Lammertink, *Journal of Materials Chemistry A*, 2022, **10**, 8401-8412.
80. Q. H. Meng, C. Hao, B. Yan, B. Yang, J. Liu, P. K. Shen and Z. Q. Tian, *Journal of Energy Chemistry*, 2022, **71**, 497-506.
81. X.-Y. Zhang, F.-T. Li, Y.-W. Dong, B. Dong, F.-N. Dai, C.-G. Liu and Y.-M. Chai, *Applied Catalysis B: Environmental*, 2022, DOI: 10.1016/j.apcatb.2022.121571.
82. H. Li, N. Yu, F. Gellrich, A. K. Reumert, M. R. Kraglund, J. Dong, D. Aili and J. Yang, *Journal of Membrane Science*, 2021, **633**.
83. H. J. Park, S. Y. Lee, T. K. Lee, H.-J. Kim and Y. M. Lee, *Journal of Membrane Science*, 2020, **611**.
84. D. D. Tham and D. Kim, *Journal of Membrane Science*, 2019, **581**, 139-149.
85. A. Konovalova, H. Kim, S. Kim, A. Lim, H. S. Park, M. R. Kraglund, D. Aili, J. H. Jang, H.-J. Kim and D. Henkensmeier, *Journal of Membrane Science*, 2018, **564**, 653-662.
86. X. Wang, X. Qiao, S. Liu, L. Liu and N. Li, *Journal of Membrane Science*, 2022, **653**.
87. X. Su, L. Gao, L. Hu, N. A. Qaisrani, X. Yan, W. Zhang, X. Jiang, X. Ruan and G. He, *Journal of Membrane Science*, 2019, **581**, 283-292.
88. M. Chen, M. Mandal, K. Groenhout, G. McCool, H. M. Tee, B. Zulevi and P. A. Kohl, *Journal of Power Sources*, 2022, **536**.
89. C. D. Giovanni, Á. Reyes-Carmona, A. Coursier, S. Nowak, J. M. Grenèche, H. Lecoq, L. Mouton, J. Rozière, D. Jones, J. Peron, M. Giraud and C. Tard, *ACS Catalysis*, 2016, **6**, 2626-2631.

90. Z. Kang, Y. Chen, H. Wang, S. M. Alia, B. S. Pivovar and G. Bender, *ACS Appl Mater Interfaces*, 2022, **14**, 2335-2342.
91. G. Jiang, H. Yu, Y. Li, D. Yao, J. Chi, S. Sun and Z. Shao, *ACS Appl Mater Interfaces*, 2021, **13**, 15073-15082.
92. J. Kim, J. Kim, H. Kim and S. H. Ahn, *ACS Appl Mater Interfaces*, 2019, **11**, 30774-30785.
93. S. Stiber, H. Balzer, A. Wierhake, F. J. Wirkert, J. Roth, U. Rost, M. Brodmann, J. K. Lee, A. Bazylak, W. Waiblinger, A. S. Gago and K. A. Friedrich, *Advanced Energy Materials*, 2021, **11**.
94. C. Klose, T. Saatkamp, A. Münchinger, L. Bohn, G. Titvinidze, M. Breitwieser, K. D. Kreuer and S. Vierrath, *Advanced Energy Materials*, 2020, **10**.
95. M. Faustini, M. Giraud, D. Jones, J. Rozière, M. Dupont, T. R. Porter, S. Nowak, M. Bahri, O. Ersen, C. Sanchez, C. Boissière, C. Tard and J. Peron, *Advanced Energy Materials*, 2019, **9**.
96. S. Chatterjee, X. Peng, S. Intikhab, G. Zeng, N. N. Kariuki, D. J. Myers, N. Danilovic and J. Snyder, *Advanced Energy Materials*, 2021, **11**.
97. X. Peng, P. Satjaritanun, Z. Taie, L. Wiles, A. Keane, C. Capuano, I. V. Zenyuk and N. Danilovic, *Adv Sci (Weinh)*, 2021, **8**, e2102950.
98. D. Kulkarni, A. Huynh, P. Satjaritanun, M. O'Brien, S. Shimpalee, D. Parkinson, P. Shevchenko, F. DeCarlo, N. Danilovic, K. E. Ayers, C. Capuano and I. V. Zenyuk, *Applied Catalysis B: Environmental*, 2022, **308**.
99. C. V. Pham, M. Bühler, J. Knöppel, M. Bierling, D. Seeberger, D. Escalera-López, K. J. J. Mayrhofer, S. Cherevko and S. Thiele, *Applied Catalysis B: Environmental*, 2020, **269**.
100. Z. Xie, S. Yu, X. Ma, K. Li, L. Ding, W. Wang, D. A. Cullen, H. M. Meyer, H. Yu, J. Tong, Z. Wu and F.-Y. Zhang, *Applied Catalysis B: Environmental*, 2022, **313**.
101. H. Kim, J. Kim, J. Kim, G. H. Han, W. Guo, S. Hong, H. S. Park, H. W. Jang, S. Y. Kim and S. H. Ahn, *Applied Catalysis B: Environmental*, 2021, **283**.
102. S. Choi, S.-H. Shin, D.-H. Lee, G. Doo, D. W. Lee, J. Hyun, J. Y. Lee and H.-T. Kim, *Journal of Materials Chemistry A*, 2022, **10**, 789-798.
103. M. Suermann, T. Gimpel, L. V. Bühre, W. Schade, B. Bensmann and R. Hanke-Rauschenbach, *Journal of Materials Chemistry A*, 2020, **8**, 4898-4910.
104. M. Bühler, F. Hegge, P. Holzapfel, M. Bierling, M. Suermann, S. Vierrath and S. Thiele, *Journal of Materials Chemistry A*, 2019, **7**, 26984-26995.
105. J. E. Park, J. Kim, J. Han, K. Kim, S. Park, S. Kim, H. S. Park, Y.-H. Cho, J.-C. Lee and Y.-E. Sung, *Journal of Membrane Science*, 2021, **620**.